Universitat Autònoma de Barcelona

Institut Català de Nanociència i Nanotecnologia

Doctoral Thesis

Atomistic simulations in hybrid C/BN structures

A thesis submitted for the degree of
Doctor of Philosophy
in the program

Doctorat en Física

Departament de Física
Facultat de Ciències

Author:

Rafael Martínez Gordillo

Supervisor:

Miguel Pruneda

Tutor:
Gemma García

July 2014

Contents

CHAPTER 1

Introduction

The transformation of materials to adapt them to our needs is one of the most ancient knowledges of human kind. Actually, the oldest ages were defined by the materials humans used to fabricate their tools (stone, bronze, iron). Starting with an empirical knowledge, which then led to scientific studies, material engineering has been important defining the life style through history. Nowadays, the development of materials includes metallic alloys, ceramics, plastics, semiconductors, biocompatible materials, textiles and composites, beside many others.

In order to get a desired specific behaviour for any material, it is first necessary to understand its properties. Given the great advances in the knowledge of the electronic structure of materials in the early 20th century, the interest in semiconductors became more important for applications in radars and as substitutes for the widely used vacuum tubes. As a result, in 1947 Bardeen, Brattain and Shockley accomplish one of the most important inventions of the last century, and perhaps of all time: the transistor. This solid state switching device meant a revolutionary change of route in the fabrication of electronic devices, enabling more compact and power efficient designs, while increasing their operation speed. Transistors are based on interfaces of different materials, either two semiconductors or a semiconductor and a metal, highlighting the importance of interfacial effects in materials. The intrinsic poor conductivity of semiconductors can be enhanced by the addition of charge donors or acceptors, while still being possible to fine tune the electric current through an external gate potential. This doping is made in high crystalline semiconductors by adding impurities of

other species with more (n-doped) or less (p-doped) electrons. Devices with non-uniform concentrations of impurities produce interesting effects, specially when semiconductors with different dopants are joined together, resulting in charge redistribution at the interface, like in p-n junctions of diodes, or n-p-n junctions of bipolar transistors.

The phenomena that take place at the interface of heterojunctions extend very little into the bulk of the constituents materials. Instead, the effect take place at the atomic scale, becoming important a deeper look to the fundamental composition of materials. The interest to observe and understand the phenomena at the microscopic level lead to more advanced measuring instruments. It is worth to remark the invention of the scanning tunnelling microscope (STM) in 1981, that made possible the observation of individual atoms, and eight years later their manipulation, which meant the beginning of nanotechnology. In the same decade of 1980s, the discovery of fullerenes by Kroto, Smalley and Curl [1] marked the importance of carbon materials in this newly created field. Nanotechnology intends to provide the tools to design and control the properties of new materials at the lowest levels of matter ever reached before, aiming to boost the development of novel technology.

Theoretical studies are very important to explain experimental observations and predict the properties of materials. Density functional theory (DFT), developed by Hohenberg, Kohn and Sham in the decade of 1960s,[2,3] is a theory based in quantum mechanics that describes the many-electron problem found in atomistic models, simplifying the mathematical expressions that describe the system making it feasible to calculate their properties at a moderate computational cost. Nowadays, DFT is one of the most popular methods for electronic structure calculations in physics, chemistry and materials science. It is an ideal tool to study interfaces, and widely used to obtain vibrational, optical and mechanical, among many others, properties of nanostructures. Even though DFT is a very powerful method, sometimes it is necessary to sacrifice accuracy in favour of computational efficiency. Here is where other methods come into play, like the tight binding (TB) approximations, which can give reasonable accurate results with low computational cost.

1.1 Graphene properties

Graphene is a one atom thick layer of carbon atoms disposed in an hexagonal array that resembles that of a honeycomb. Graphene, being an allotropic form of carbon, can be seen as the structure from which other allotropic forms of carbon can be build up. Fullerenes [4] are obtained by wrapping graphene, introducing curvature with pentagons and forming closed spherical zero-dimensional (0D) nanostructures. Nanotubes [5] are obtained by rolling graphene obtaining one-dimensional (1D) structures. Graphite is made up by stacking

graphene layers forming a three-dimensional (3D) structure. Although graphene is the basic building block to construct and understand many properties of these materials, it is the youngest member of the family of C allotropes obtained experimentally. In fact, before its isolation it was though that purely 2D materials were unstable. In 2004, Novoselov *et al.*[6] achieved the observation and characterisation of single layers of graphene, noticing the great potential that this material has for electronic devices. Since its discovery, a lot of effort has been made in understanding the properties if this outstanding material.

The honeycomb lattice of graphene, shown in Figure 1.1, can be considered as two triangular sublattices interpenetrated, resulting in a unit cell formed of two basis atoms. It is a common practice to designate these two atomic sites as A and B sublattices. The four valence electronic orbitals of C atoms in the lattice have sp^2 hybridization, meaning that three in-plane σ-bonds with covalent character are formed with the three nearest neighbours of each atom, and another more delocalized orbital, the β-orbital, is formed with its axis of symmetry being perpendicular to the lattice plane. The rigid σ-bonds contribute primarily to the great strength of graphene,[7] while the β-orbitals play the main role in the electronic properties.[8]

One of the most distinguishable characteristics of graphene is its band dispersion, which is shown in Figure 1.1 (right). Graphene is a semimetal, i.e. a zero gap semiconductor. The Fermi surface becomes a single point in reciprocal space, with a two-fold degeneracy. The degeneracy comes from the formation of two symmetric valleys at the **K** and **K** points. Close to the valleys, the dispersion relations can be well described by Dirac s relativistic equation, considering electrons to have zero rest mass.[9] This results in a linear energy dispersion of the form

$$E(\mathbf{k}) = \pm \; v_{\mathrm{F}} \, \mathbf{k} \tag{1.1}$$

where v_{F} is the Fermi velocity, and $\mathbf{k}$ is taken relative to **K** (or **K**). Equation 1.1 is valid as long as $\mathbf{k} \propto \mathbf{K}$, which implies that the dispersion is linear only for energies close to E_{F}.

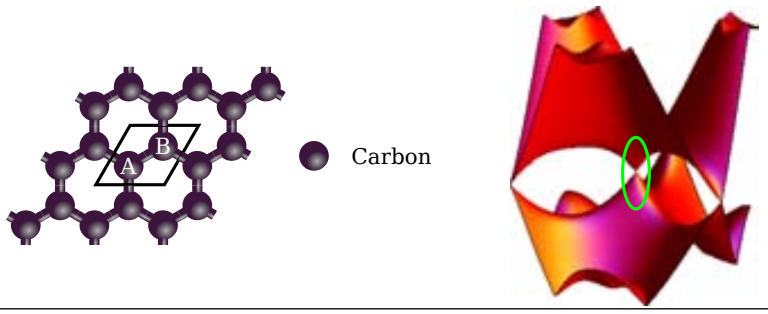

Figure 1.1: Atomic model (left) and band structure (right) of graphene. The Dirac cone in the band structure is encircled in green.

As seen in Figure 1.1 (green circle), the bands close to **K** and **K** are shaped as cones, thus, each valley is called a Dirac cone, and **K** and **K** are called Dirac points. A more detailed description of the properties of graphene can be found in the review by Castro Neto *et al.*[10]

Substrates for graphene

In the ideal case of perfect graphene, the ballistic conductivity sets the mobility to values in the order of 10^5 $cm^2V^{-1}s^{-1}$ at room temperature and even higher than 10^6 $cm^2V^{-1}s^{-1}$ at low temperatures, using the Boltzmann theory of transport.[11] In free-standing graphene samples the measured electrical mobilities are $\sim 2\times10^5$ $cm^2V^{-1}s^{-1}$ at low temperatures, and $\sim 1.2\times10^5$ $cm^2V^{-1}s^{-1}$ for higher temperatures,[12,13] which are very close to the expected ballistic behaviour. The problem with suspended graphene is that it imposes limitations on functionality, is difficult to fabricate and does not allow an easy way to measure the samples with scanning probe techniques. When using substrates, the transport properties are degraded for several factors like electron-phonon interactions, the corrugation of graphene sheets, defects and impurity scattering and grain boundaries.[14–20] Given that graphene is just one atom thick, the influence of the supporting substrate cannot be neglected and plays an important role modifying the intrinsic physical properties of graphene.

Many substrates have been used to grow or deposit graphene, like SiC,[21,22] metal surfaces,[23,24] mica[25] or SiO_2.[6] The latter, being one of the most common, imposes several limitations to the electronic transport in graphene.[14,26] In polarizable substrates, such as SiO_2 or SiC, electron charges in graphene couple to surface vibrational modes with polar character from the substrate increasing the scattering of electrons.[17,27] Due to this phonon scattering, the mobility using SiO_2 as substrate could reach values of at most 4×10^4 $cm^2V^{-1}s^{-1}$ at room temperature even for very clean samples,[26] which are difficult to obtain, and in practice, scattering defects further reduce the mobility to around 1×10^4 $cm^2V^{-1}s^{-1}$.[6,28–30] The SiO_2 surface is usually rough enough to introduce corrugation in graphene having an important impact in its electronic properties,[18,31] with variations in the height of the surface of ~ 2 Å.[32] The appearance of charge inhomogeneities over large areas in graphene samples, can be related to these topographic corrugations or to charge-donating impurities trapped between graphene and the substrate.[18,31,33,34] These inhomogeneities, known as electron-hole puddles, degrade the intrinsic transport properties of graphene and have motivated the search for alternative substrates, to actually reach the physical properties of the low carrier density region at the Dirac point.

Corrugations also produce charge inhomogeneities that lead to doping effects,[35,36] and create long-range scattering potentials.[16] The strain emerging from the layer deformation modifies the interactions between electronic states, hybridizing β and σ orbitals. This effect

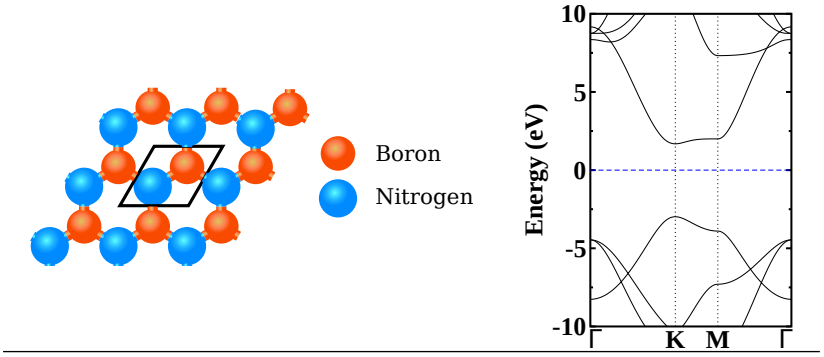

Figure 1.2: Atomic model (left) and band structure (right) of h-BN.

can be described in the simple TB model as a modulation in the hopping integrals, which effectively represents a vector potential acting over the graphene lattice.[35] Hence, the curvature in graphene generates a pseudo-magnetic field that gives rise to the appearance of local Landau levels at zero energy.[36,37]

Charged impurities can be partially screened by using dielectric materials with high dielectric constant κ as substrate. According to the self-consistent theory developed by Adam *et al.*,[38] the conductivity increases for increasing κ, suggesting the use of HfO_2 to increase the mobility by a factor of 5 with respect to that of SiO_2. The enhancement of the mobility with higher κ was proven using different solvents as top dielectric layer covering graphene.[39] However, using high-κ dielectrics does not seem to be the final solution,[40] as the surface phonon modes arising from high-κ dielectric counteract the enhancement of Coulomb scattering reduction,[41] making substrates like HfO_2 have less capabilities than SiO_2.[42] To minimize surface phonon scattering processes keeping the high-κ dielectric to screen charge impurities, a polymer buffer has been used between graphene and HfO_2.[43]

A more promising substrate for graphene has been found in h-BN due to its characteristics, which are described in the next section, and in section 1.3, the effects that h-BN has on graphene when used as substrate are mentioned.

1.2 *h*-BN properties

With the discovery of graphene and the advances in graphene synthesis and growth control, the research of other 2D systems has been fostered.[44] In particular, hexagonal boron nitride (h-BN) has emerged as a promising compound that can complement the properties of graphene. The atomic structure of h-BN, shown in Figure 1.2 (left), is the same as graphene, with boron atoms substituting the C atoms in one of the sublattices, and nitrogen atoms

substituting those of the other sublattice. Although h-BN is isostructural to graphene and both materials have the same number of electrons per unit cell, they present very different properties. Because A and B sites are occupied by different species a gap is opened. The band structure of h-BN is shown in Figure 1.2 (right). As can be seen, h-BN is an insulator with a large band gap of $\sim$6 eV,[45] making it a promising candidate for optical applications in the UV range.[45–47] The σ-bonds between B and N have a more ionic character than in graphene, and are strong enough to make h-BN have a great thermal and chemical stability.[48,49] In fact, thermal transport properties are comparable to those of graphene,[50] making it suitable for thermal dissipation applications. Being h-BN non-centrosymmetric, it presents interesting piezoelectric and flexoelectric effects.[51,52] The chemical compatibility between C, B and N and the superb characteristics of graphene and h-BN have attracted the attention of many scientific research groups that try to get the best of both and to obtain new properties not present in these materials separately.

1.3 Graphene/BN hybrid nanostructures

To exploit the properties of graphene, it is important to engineer its properties by tuning its electronic and mechanical behaviours at will. Tuning of the gap is one of the central topics for using graphene in electronic devices, and many attempts have been made by mechanical, chemical and structural modification.[53–55] Other approaches involve the formation of graphene/BN heterostructures to modulate the gap, from which two types of system can be distinguished:

- Coplanar hybrids.
- Stackings of graphene over h-BN.

Stackings

The characteristics of h-BN make it an appealing substrate for graphene electronics: a dielectric material with large band gap, strong in-plane bonds, planar structure, low density of charge traps and relatively inert surface without dangling bonds.[56] The roughness of graphene over h-BN is only 2-30 pm,[57,58] and the mobility in exfoliated graphene can reach values of 1 4×10^5 $\mathrm{cm^2V^{-1}s^{-1}}$ at low temperatures.[56] At room temperature, mobilities approaching the ballistic limit can also be obtained by encapsulating graphene on BN with mobilities larger than $1{\times}10^5$ $\mathrm{cm^2V^{-1}s^{-1}}$.[59] Even for the more disordered CVD grown graphene, the mobility using h-BN as substrate is $2\,9 \times 10^4$ $\mathrm{cm^2V^{-1}s^{-1}}$ at low temperatures.[60]

Moreover, very recently, the use of *h*-BN as a substrate for graphene has been boosted not only because it is a clean way to sustain graphene, but due to the appearance of new phenomena. While in-plane C/BN heterostructure yield 2D systems with 1D interface, deposition of graphene over a *h*-BN substrate yield a 2D system with a 2D interface, and while interfacial effects in the in-plane hybrids are mainly localized at the interface, the effects of stacking graphene over *h*-BN extent over all the system, highlighting the importance of substrates. An interesting substrate effect in graphene layers is the formation of moiré patterns observed with STM.[58,61] These moiré patterns give rise to the formation of superlattices, and new Dirac cones emerge at non-zero energies.[61] The modification of the electronic structure of graphene due to the *h*-BN substrate has allowed the study of a physical phenomenon not observed experimentally before: the Hofstadter butterfly, a fractal spectrum that appears when electrons move under the effect of an electric and magnetic fields.[62–64]

Coplanar hybrids

Boron and nitrogen are in the same row of the periodic table than carbon, and they have similar atomic radius. In C-based materials, this makes more feasible the substitution of C atoms by B (*p*-doped) or N (*n*-doped) without significantly distorting the crystalline lattice. Thus, B and N have been the natural choice for doping graphitic materials like fullerenes,[65,66] nanotubes (NT),[67–70] nanoribbons (NR)[71] and graphene.[72] Moreover, the structural similarity and chemical compatibility between graphite and *h*-BN prompted the idea of hybrid systems made of these two compounds,[73] with the first synthesised materials being bulk alloys with layered hexagonal structure, containing C, B and N in each layer.[74–76] Their exact atomic configuration was not clear but were considered to be hybrids with BC_2N composition.[75] For B C N NT, the same composition was proposed[77] and was soon confirmed experimentally.[67,78] In the samples obtained by Stephan *et al.*[67] and in many others that followed these,[79–84] evidence of phase segregation was found, with zones of only C atoms and others with only BN or BC_2N. The phase separation is explained considering the bond strength of C C and B N, being energetically more favourable than the C B and C N bonds,[85] such that segregated domains maximise the number of C C and B N bonds over C N and C B. Notice that the interfaces present in these domain-segregated systems correspond to junctions between a semimetal material (graphene) and an insulator (BN), which could lead to new phenomena and devices. This motivated an increase in the study of the electronic properties of NT with C/BN interfaces.[86–89]

Taking this same idea, single layer in-plane heterostructures of graphene and *h*-BN have been recently studied.[90–95] The experimental feasibility of these hybrids was sustained by the previous evidence of segregation in NT and in bulk alloys and supported by theoretical

models.[85,96,97] In fact, the first experimental attempts to obtain hybrid layers relied in techniques initially developed to dope carbon NT.[98] Great progress has been achieved in the last years to control the synthesis of lateral junctions,[99–105] although a precise and well understood method is still missing. This highlights the importance of studying coplanar hybrid systems in order to better understand the impact of interfacial effects in the electronic, magnetic and transport properties of these novel nanomaterials.

Experimentally, a common method to obtain hybrid graphene/BN samples is chemical vapour deposition (CVD), and can be done in a single stage using precursors for both materials simultaneously,[98,100,103] in two stages to grow flakes of one material and then continue the growth of the second material,[104] or sequentially in two steps with an etching in between the process.[99,105] Domains larger than 1 ϵ m can be obtained, and at the boundaries of these domains a transition zone is formed.[99,100] This transition region is made of an amorphous phase whose chemical composition is not clear and has widths of around 10 nm. In the method proposed by Lu *et al.*,[106] the synthesised samples have triangular BC_2N domains, and instead of the amorphous transition regions, the crystalline domains are surrounded by thin carbon NR of ∼5 Å. With this progress in improving the control of size, shape and boundaries of the domains, it is clear that precise engineering of hybrid structures will be available in the near future for device applications. Moreover, new possibilities arise if the inclusion of other 2D materials is considered.

1.4 Interfaces

Heterojunctions are formed when joining two dissimilar materials and can give rise to new physical phenomena at the interface. Junctions made of semiconductor-semiconductor and metal-semiconductor materials are very important in modern electronic and optoelectronic devices. There are many characteristics that come into play when defining the behaviour of heterostructures, like the crystallographic orientation of the interface, the lattice strain and polarity discontinuities, which are related to interfacial bound charges and electronic reconstruction. While some effects are desirable to design devices, others are not convenient, like the lattice mismatch between the two materials, which causes dislocations and strain at the interface, leading to undesired effects as carrier recombination at the junction.[107,108] The successful fabrication of heterostructures depends a lot on the capability of epitaxial techniques to grow lattice-matched materials with high crystallinity.

When two semiconductors are joined together and thermodynamic equilibrium is reached, the Fermi level (E_F) will match in both materials resulting in a realignment of the electronic bands close to the interface. The misalignment of the conduction and valence bands at both

sides of the interface forms a step barrier defining important characteristics of heterojunctions. The properties of the two constituents will remain the same in the bulk, and the important changes will occur in a very narrow region around the interface. The line-up of the bands is determined by the band offsets,[109 111] which represent the energy step at the interface, as shown in Figure 1.3. The valence band offset can be defined as[112]

$$\Delta E_{\mathrm{VBO}} = \left(E_0^{(2)} - E_v^{(2)}\right) - \left(E_0^{(1)} - E_v^{(1)}\right) + \Delta\tilde{V}, \tag{1.2}$$

where E_v and E_0 are the maximum of the valence band and the vacuum level (or the average electrostatic potential in the bulk), for each semiconductor. The term $\Delta\tilde{V}$, is the difference of the average electrostatic potential in each part of the heterojunction, and can be obtained with macroscopic average techniques.[113]

A similar situation is present in metal-semiconductor junctions.[111] In this case, instead of the top of the valence band, the Fermi energy of the metal has to be considered, and the term $E_0 - E_{\mathrm{F}}$ corresponds to the work function of the metal. Electronic states from the metallic component are induced into the semiconductor and the band alignment leads to the formation of a Schottky barrier. While this effect is important for electronic devices, it is not always convenient to have such barriers. To operate a semiconductor-based device, some current is necessary to apply power to the system. In this case, the current is provided through a metallic contact and the junction must present an ohmic behaviour (i.e. behave according to Ohm's law). For metal-semiconductor interfaces, an acceptable contact would present a small resistance compared to the total resistance of the semiconductor device. To achieve this, the work function of the metal must be low enough or the semiconductor highly doped, to allow the Fermi energy to lie in (or very close) to the conduction or valence band of the semiconductor, forming a negligible Schottky barrier.[114]

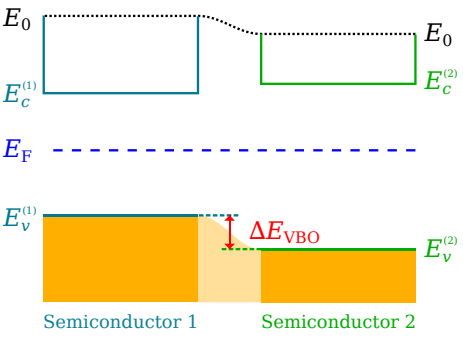

Figure 1.3: Diagram of a heterojunction, showing the valence band offset, ΔE_{VBO}. The Fermi level is marked with the dashed blue line.

Besides the traditional semiconductors largely studied since the first half of the last century, oxides are examples where growth techniques have evolved dramatically in the last two decades, allowing the fabrication of epitaxial heterojunctions of these materials with atomistic precision, from which $LaAlO_3/SrTiO_3$ interfaces have become a prototypical system. This kind of systems are insulating in the bulk and, surprisingly, the experimentally observed effects at the interface have shown new physics that suggest applications for new

devices. Among the interesting effects found in oxides it is worth mentioning the formation of metallic interfaces with high-mobilites,[115,116] superconducting behaviour at low temperatures[117] and magnetic ordering.[118]

To understand many of the phenomena that take place in the two-dimensional (2D) interface of crystalline materials, it is important to consider polarization effects. When a bulk system is cut, the ionic character of the atoms that constitute the crystal may cause a polarization discontinuity depending on the crystallographic orientation of the produced surface.[119,120] The same is true in two-dimensional (2D) systems like h-BN, where the polarity plays a very important role. In graphene/BN heterojunctions, the electronic behaviour of graphene nanoribbons is changed due to interfacial effects which can be modulated by the piezoelectric properties of h-BN.

1.5 Objectives

Hybrid systems with graphene and h-BN in the stacked and co-planar configurations are very actively developed areas of research and are considered to be very important for future development of graphene-based technology. This thesis is focused in the study of in-plane and stacked hybrids to get a better insight of the factors that could allow a better control of their properties. To accomplish this, it is necessary a clearer understanding of the effects that emerge as a consequence of joining these two compounds together. The principal objectives of this thesis are:

- Explain the causes of the appearance of new features in the heterostructures.
- Model the heterostructures in a simple manner to have a more *exposed* description of the systems.
- Analyse the behaviour of the hybrid systems under different conditions.

In chapter 3, graphene over h-BN is analysed within DFT. Different superlattices are considered to explore the changes changes in the atomic and electronic structure of graphene. The features analysed include the formation of new Dirac points, renormalization of the Fermi velocity and structural strains induced by the substrate. The case of graphene encapsulated within two BN monolayers is also analysed. The strength of the potential is estimated from the local energies finding a dependence with the size of the moiré. The parametrization of the moiré potential is then used in chapter 4 to calculate transport properties within the TB model. The effect of lattice disorder is also included in the model. The mean free path and resistivity are obtained for different intensities of the disorder. The effect of increasing the

disorder is studied focusing in the impact over the main and non-zero Dirac points. A brief discussion about the Hofstadter butterfly is also presented giving place to future research in order to understand the many interesting phenomena that occurs in this fractal spectrum.

In chapter 5, hybrid systems composed of graphene and *h*-BN are studied within DFT for different interfacial configurations. Then, a TB model is obtained parametrized from DFT data. Due to the important impact of interfacial effects in the electronic structure of in-plane hybrids, additional terms have to be included in the simple TB Hamiltonian to properly represent edge states of graphene and *h*-BN. Changes in the behaviour of the system due to variations in the values of the most relevant parameters are analysed. The model is intended to work with any proposed geometry and for very large structures. This opens the door to many future projects to study a variety of systems of experimental interest. The model can be easily used for transport calculation of mixed C/BN domains.

In chapter 6, the electromechanical response in hybrid systems with zigzag interface is studied. Tensile and compressive strains are applied perpendicular and parallel to the interface. The behaviour of this lateral junctions is dominated by the piezoelectric response of *h*-BN. The gaps in this systems can be modulated by mechanical deformations and semiconductor-half-metal and half-metal-semiconductor transitions are found. The piezoelectric effect is also studied in hybrid systems of graphene and BC_2N yielding an improved response over *h*-BN. Tubular geometries are also considered, finding an important magnetoelectricity effect.

CHAPTER 2

Methodology

In this chapter, the theoretical background used throughout the thesis is exposed. All the numerical simulations done here, are based on density functional theory (DFT) or tight binding (TB) methods, which are explained in sections 2.2 and 2.3, respectively. These two methods are widely used to model atomistic systems, and the different characteristics and advantages of each one make them appropriate for different situations. DFT, an *ab initio* method, is an accurate approach with a moderate computational cost, useful for small to medium size (∼100 1000 atoms) systems with a very high level of reliability for ground state properties. On the other hand, the TB approximation is cheaper and is more suitable for large, or very large (∼10^6 atoms) systems with a less accurate description of the system, but with the advantage that the model can be parametrized to fit the results of other more elaborated methods or to experiments.

2.1 Solution to the Schrodinger equation

The modelling of electrons can be done by solving the time-independent Schrodinger equation

$$\mathcal{H}\Psi = E\Psi \tag{2.1}$$

where $\mathcal{H}$ represents the Hamiltonian operator, Ψ is the many-body stationary wave function of the system and E its eigen-energies. For molecular systems, which usually involves several degrees of freedom (counting all the electrons and ions in the system), the eigenvalue problem 2.1 can become very complicated. Several approximations have proven to simplify the solution to the many-particle wave function.

The many body problem

In a system of interacting atoms consisting in N electrons, with mass m_e and charge $-e$, and M ions, with mass M_j and charge $Z_j e$, the wave function depends on the coordinates $\mathbf{r}_j$ and $\mathbf{R}_j$ of electrons and ions, respectively:

$$\Psi = \Psi(\mathbf{r}_1\ \mathbf{r}_2 \qquad \mathbf{r}_N; \mathbf{R}_1\ \mathbf{R}_2 \qquad \mathbf{R}_M) \tag{2.2}$$

For this system, the Hamiltonian operator is

$$\begin{aligned}\mathcal{H} =& \mathcal{T}_\mathrm{e} + \mathcal{T}_\mathrm{N} + \mathcal{V}_\mathrm{ee} + \mathcal{V}_\mathrm{Ne} + \mathcal{V}_\mathrm{NN} \\ =& -\frac{\hbar^2}{2m_e}\sum_{j=1}^{N}\nabla_j^2 - \frac{\hbar^2}{2}\sum_{m=1}^{M}\frac{\nabla_m^2}{M_m} + \frac{1}{2}\sum_{j=m}\frac{e^2}{\mathbf{r}_j - \mathbf{r}_m} \\ & - \sum_{j\,m}\frac{Z_m e^2}{\mathbf{r}_j - \mathbf{R}_m} + \frac{1}{2}\sum_{j=m}\frac{Z_j Z_m e^2}{\mathbf{R}_j - \mathbf{R}_m}\end{aligned} \tag{2.3}$$

where the first two terms are the kinetic energy of electrons and ions, and the last three terms, the electron-electron, nuclei-electron and nuclei-nuclei interactions. In such scenario, the wave function of each particle are coupled among them, and the system has to be solved simultaneously. In particular, the Coulomb interactions ($\mathcal{V}$) make the Schrodinger equation to be inseparable for more than one particle and solving the system involves the solution of a $3(N+M)$-dimensional eigen-problem (not considering the spin degree of freedom).

The Born-Oppenheimer approximation

A first approximation to deal with Equation 2.3 is Born-Oppenheimer approximation,[121] based on the fact that atomic nuclei are massive in comparison with electrons (around 10^3 10^5 times more massive). It can be then assumed that heavy nuclei move so slow that can be considered fixed. Within this approximation, the term $\mathcal{T}_\mathrm{N}$ is zero, and the problem is reduced to solving the many-body problem of electrons in the presence of the ionic potential,

by considering the electronic part of the Hamiltonian

$$\mathcal{H}_{\mathrm{e}} = -\frac{\hbar^2}{2m_e}\sum_{j=1}^{N}\nabla_j^2 + \frac{1}{2}\sum_{j=m}\frac{e^2}{\mathbf{r}_j - \mathbf{r}_m} - \sum_{j\,m}\frac{Z_m e^2}{\mathbf{r}_j - \mathbf{R}_m} \tag{2.4}$$

and solving for the electronic wave functions Ψ:

$$\mathcal{H}_{\mathrm{e}}\ \Psi(\mathbf{r}_1\ \mathbf{r}_2\ \ldots\ \mathbf{r}_N) = E\ \Psi(\mathbf{r}_1\ \mathbf{r}_2\ \ldots\ \mathbf{r}_N) \tag{2.5}$$

If one is interested in including the dynamics of nuclei, a common solution is to treat the ions as classical particles and solve the quantum mechanical wave function of electrons at each position of the nuclei.

The problem of solving the electronic part of a system is still difficult, and no analytic solution exist for more than one electron (hydrogenic atoms). Other approximations have been proposed to overcome this difficulty, having different impact in the accuracy of the predictions. Among the approximations to the many body problem, it is worth mentioning the Hartree-Fock Theory, quantum Monte Carlo methods, many-body perturbation methods and DFT. The latter has become one of the most successful and popular methods for electronic structure calculations, and the method in which an important part of this thesis is based.

2.2 Density Functional Theory

DFT is a method for electronic structure calculations and is based on the theorem proposed by Hohenberg and Kohn[2] which states that the total energy of a system, E_{tot}, is a unique functional of the electron density $n(\mathbf{r})$. Thus, the problem of N electrons with $3N$ variables, is changed to a problem with 3 spatial variables of $n(\mathbf{r})$. Kohn and Sham[3] proposed a way to construct and minimize the total energy functional $E_{\mathrm{tot}}[n(\mathbf{r})]$. In this section, the fundamentals of DFT are explained in more detail, and an overview of the exchange and correlations functionals, and the basis sets used in DFT calculations is given.

Hohenberg-Kohn Theorem

Consider a system of electrons subject to the influence of an external potential $V_{\mathrm{ext}}(\mathbf{r})$. The Hamiltonian is

$$\mathcal{H} = \mathcal{T}_{\mathrm{e}} + \mathcal{V}_{\mathrm{ee}} + \mathcal{V}_{\mathrm{ext}} \tag{2.6}$$

The ground state electronic density $n_0(\mathbf{r})$ is uniquely determined by the external potential, and the inverse is also true. To proof this, a *reductio ad absurdum* demonstration is done. Suppose that another potential, V_{ext} ($V_{\text{ext}} - V_{\text{ext}} = \text{const}$), gives rise to the same ground state density $n(\mathbf{r})$. Each potential will lead to different ground state wave functions, and . Since is not the ground state of $\mathcal{H}$, it follows that

$$E = \quad \mathcal{H} \quad < \quad \mathcal{H} \tag{2.7}$$

The last term can be rewritten as

$$\begin{aligned} \mathcal{H} \quad &= \quad \mathcal{H} \quad + \quad \mathcal{H} - \mathcal{H} \\ &= E \; + \quad \mathcal{V}_{\text{ext}} - \mathcal{V}_{\text{ext}} \\ &= E \; + \quad \big(V_{\text{ext}}(\mathbf{r}) - V_{\text{ext}}(\mathbf{r})\big)\, n_0(\mathbf{r}) d\mathbf{r} \end{aligned} \tag{2.8}$$

and substituting in Equation 2.7

$$E < E \; + \quad \big(V_{\text{ext}}(\mathbf{r}) - V_{\text{ext}}(\mathbf{r})\big)\, n_0(\mathbf{r}) d\mathbf{r} \tag{2.9}$$

The primed and unprimed labels can be swapped to give

$$E \; < E + \quad \big(V_{\text{ext}}(\mathbf{r}) - V_{\text{ext}}(\mathbf{r})\big)\, n_0(\mathbf{r}) d\mathbf{r} \tag{2.10}$$

Adding Equation 2.9 and Equation 2.10 results in the inconsistency $E + E \; < E + E$. Thus, V_{ext} is uniquely defined by $n_0(\mathbf{r})$. In turn, the system described by $\mathcal{H}$, which is fixed by the external potential, is a unique functional of $n_0(\mathbf{r})$ (within a constant), and with the knowledge of $n_0(\mathbf{r})$, all the properties of the system can be accessed.

Kohn-Sham equations

A procedure to treat DFT is based on an idea proposed by Khon and Sham,[3] where the many-body problem is replaced by a non-interacting system of electrons influenced by an effective potential, and the solution is given by the single-particle Schrodinger equation. The Hamiltonian in this case is given by

$$\mathcal{H}_{\text{KS}} = \mathcal{T}_{\text{s}} + \mathcal{V}_{\text{eff}} \tag{2.11}$$

where $\mathcal{T}_{\text{s}}$ is the kinetic energy operator for a system of non-interacting electrons, and $\mathcal{V}_{\text{eff}}$ represents the effective potential, both being functionals of the electronic charge density

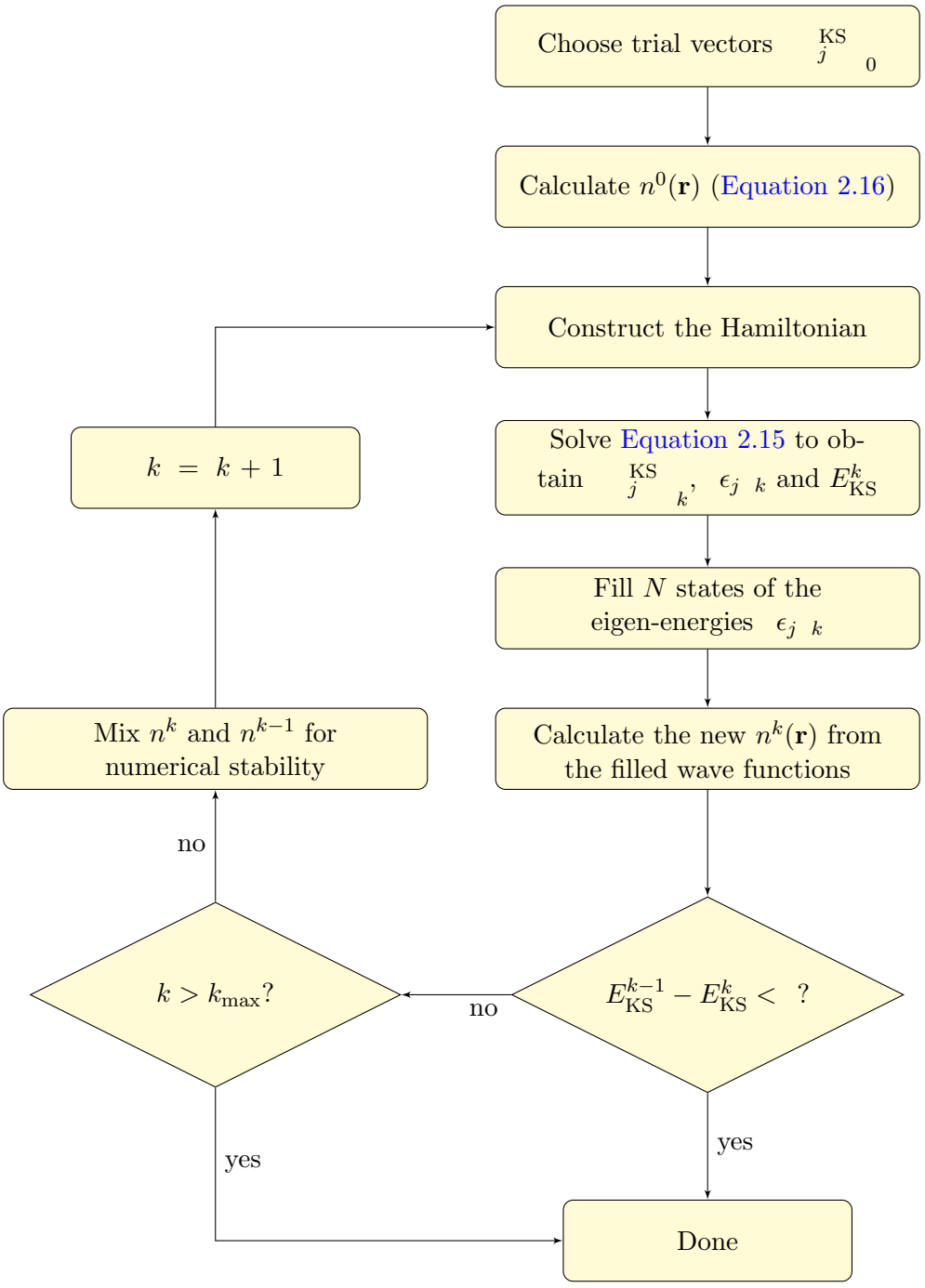

Figure 2.1: Flow chart of the DFT algorithm.

$n(\mathbf{r})$. The effective potential is defined as

$$V_{\text{eff}}\left[n(\mathbf{r})\right] = V_{\text{ext}}\left[n(\mathbf{r})\right] + V_{\text{H}}\left[n(\mathbf{r})\right] + V_{\text{xc}}\left[n(\mathbf{r})\right] \tag{2.12}$$

where V_{H} is the classical Hartree potential

$$V_{\text{H}}(\mathbf{r}) = -e \quad \frac{n(\mathbf{r})}{\mathbf{r}-\mathbf{r}} d\mathbf{r} \tag{2.13}$$

and

$$V_{\text{xc}}\left[n(\mathbf{r})\right] = \frac{\delta E_{\text{xc}}\left[n(\mathbf{r})\right]}{\delta n(\mathbf{r})} \tag{2.14}$$

with E_{xc} being the exchange-correlation energy functional, where all the interactions between electrons are included. The eigenproblem becomes

$$\left(-\frac{^2}{2m_e} \quad ^2 + V_{\text{eff}}(\mathbf{r})\right) \quad {}^{\text{KS}}_{j}(\mathbf{r}) = \epsilon_j^{\text{KS}} \quad {}^{\text{KS}}_{j}(\mathbf{r}) \tag{2.15}$$

where ${}^{\text{KS}}_{j}$ and ϵ_j^{KS} are not the actual wave function and energy of the electrons, but auxiliary quantities to calculate the electron density by

$$n(\mathbf{r}) = \sum_{j}^{N} \left| \quad {}^{\text{KS}}_{j}(\mathbf{r})\right|^2 \tag{2.16}$$

The total energy functional is

$$E_{\text{KS}}\left[n(\mathbf{r})\right] = T_{\text{s}}\left[n(\mathbf{r})\right] + E_{\text{H}}\left[n(\mathbf{r})\right] + E_{\text{xc}}\left[n(\mathbf{r})\right] + \quad V_{\text{ext}}(\mathbf{r})n(\mathbf{r})d\mathbf{r} \tag{2.17}$$

and the ground state of the system can be found by minimizing E_{KS} with respect to variations in the electron density, with the constraint that the number of electrons, N, remains constant.

An overview of the DFT algorithm is shown in Figure 2.1. The process involves a self-consistent cycle that goes on until a converged electronic density is obtained. The criterion to decide whether $n(\mathbf{r})$ is converged or not can vary, being a common one to compare the Kohn-Sham total energies E_{KS} of the present and previous cycles, and consider $n(\mathbf{r})$ to be converged if the difference is less than a certain (small) tolerance.

Basis sets

To solve Equation 2.15, the wave functions $\overset{\mathrm{KS}}{j}$ are usually expanded as a linear combination of basis functions

$$\overset{\mathrm{KS}}{j}(\mathbf{r}) = \sum_{\mu} c_{\mu j} \ \mu(\mathbf{r}) \tag{2.18}$$

where ϵ is the number of functions in the basis set, $c_{\mu i}$ are the expansion coefficients to be determined and μ forms the basis set. Within the SIESTA code,[122] the basis functions are taken as localized atom-centred orbitals. The basis orbitals are numerically generated as radial functions that depend on the position with respect to the atom which they belong, $\mu(\mathbf{r}) \equiv \mu(\mathbf{r}-\mathbf{R}_\mu)$ ($\mathbf{R}_\mu$ is the ionic position), and are zero beyond a certain cutoff radius.[123]

The basis functions are products of a pure radial function and a spherical harmonic

$$\overset{lm_l n}{\mu}(\mathbf{r}_\mu) = R_{ln}(r_\mu) Y_{lm_l}(r_\mu) \tag{2.19}$$

where $\mathbf{r}_\mu = \mathbf{r} - \mathbf{R}_\mu$, $r_\mu = \mathbf{r}_\mu$, and $r_\mu = \mathbf{r}_\mu \ r_\mu$. The numbers l and m_l have the usual notation for the angular momentum quantum numbers, while n, in this context, is an index to distinguish between orbitals with the same angular dependence. To each ionic core, several basis function can be assigned, which determines the size of the basis for each atom. To have an acceptable basis for certain chemical element, it must consider at least all the shells that are occupied by electrons in its atomic ground state. Multiple-ζ basis can be used by considering several orbitals with the same l and m quantum numbers, but with a different radial dependence. To further enhance the basis set, polarization orbitals have to be included, by increasing l to a higher angular momentum.

In calculations for crystalline systems, the reciprocal space is sampled by a k-mesh, and the Kohn-Sham equation has to be solved for each point in the mesh, adding an extra quantum number: the crystal momentum $\mathbf{k}$. In these periodic systems, the Bloch representation of the wave functions is used:

$$\overset{\mathrm{KS}}{j\mathbf{k}}(\mathbf{r}) = \sum_{\mathbf{T}\mu} c_{\mu j}(\mathbf{k}) e^{i\mathbf{k}\cdot(\mathbf{r}_\mu+\mathbf{T})} \ \mu(\mathbf{r} - \mathbf{R}_\mu - \mathbf{T}) \tag{2.20}$$

where the atomic orbitals are periodically repeated to every other cell, with translations given by lattice vector $\mathbf{T}$.

2.3 Tight Binding

The tight binding method is an approach to solve the Schrodinger equation based on linear combination of atomic orbitals.[124] The Hamiltonian matrix element between orbital μ and orbital ν is

$$H_{\mu\,\nu}(\mathbf{k}) = \sum_{\mathbf{T}} e^{i\mathbf{k}\cdot(\mathbf{R}_\nu+\mathbf{T}-\mathbf{R}_\mu)} \int d\mathbf{r}\lambda^*_\mu(\mathbf{r}-\mathbf{R}_\mu)\mathcal{H}\lambda_\nu(\mathbf{r}-\mathbf{R}_\nu-\mathbf{T}) \tag{2.21}$$

and the overlap matrix is

$$S_{\mu\,\nu}(\mathbf{k}) = \sum_{\mathbf{T}} e^{i\mathbf{k}\cdot(\mathbf{R}_\nu+\mathbf{T}-\mathbf{R}_\mu)} \int d\mathbf{r}\lambda^*_\mu(\mathbf{r}-\mathbf{R}_\mu)\lambda_\nu(\mathbf{r}-\mathbf{R}_\nu-\mathbf{T}) \tag{2.22}$$

Considering an expansion of the eigenfunctions similar to that in Equation 2.20, the coefficients are found by solving the equation

$$\sum_{\nu} \left[H_{\mu\,\nu}(\mathbf{k}) - \epsilon_j(\mathbf{k})S_{\mu\,\nu}(\mathbf{k})\right] c_{\nu j}(\mathbf{k}) = 0 \tag{2.23}$$

If the basis functions are orthonormal, the equation can be written as

$$\sum_{\nu} H_{\mu\,\nu}(\mathbf{k})c_{\nu j}(\mathbf{k}) = \epsilon_j(\mathbf{k}) \sum_{\nu} c_{\nu j}(\mathbf{k}) \tag{2.24}$$

The representation of the Hamiltonian in terms of localized orbitals, has the advantage that the matrix elements become negligible for orbitals far away from each other. The terms in the integral in Equation 2.21 can be divided into one-, two- and three-centre integrals. While these integrals can be solved numerically, a simplified approach, the semi-empirical tight binding, considers a parametrized form of the matrix terms in the Hamiltonian:

$$H_{\mu\,\nu}(\mathbf{k}) = {}_\mu\delta_{\mu\nu} + \gamma_{\mu\nu} \sum_{\mathbf{T}} e^{-i\mathbf{k}\cdot(\mathbf{R}_\nu+\mathbf{T}-\mathbf{R}_\mu)} \tag{2.25}$$

where $\delta_{\mu\nu}$ is the Kronecker delta,

$${}_\mu = \int d\mathbf{r}\ {}^*_\mu(\mathbf{r})\mathcal{H}\ {}_\mu(\mathbf{r}) \tag{2.26}$$

and

$$\gamma_{\mu\nu} = \int d\mathbf{r}\ {}^*_\mu(\mathbf{r}-\mathbf{R}_\mu)\mathcal{H}\ {}_\nu(\mathbf{r}-\mathbf{R}_\nu-\mathbf{T}) \tag{2.27}$$

The parameter ${}_\mu$, is related to the potential energy of the orbital ${}_\mu$, and depends only on the type of orbital, while $\gamma_{\mu\nu}$ is related to the kinetic energy of electrons hopping from orbital ${}_\mu$ to orbital ${}_\nu$, and are considered to depend only on the distance between both

orbitals.

2.4 Transport in the Kubo formalism

When a system in equilibrium is perturbed by, for instance, an optical, electric or thermal fluctuation, it will response to such external effect and evolve over time. The response can be measured to obtain the correlation between the input perturbation and the output evolution of the system. The effect of the perturbation will dissipate as the time passes, inducing fluctuations in the system around its equilibrium state. If the fluctuations are considered to be small, first order perturbation theory can be used to obtain the modifications of any observable with respect to the unperturbed ground state. This change represent the linear response of the system to the external perturbation. The Kubo approach is a technique used to calculate the linear response in materials, which is suitable for the study of quantum transport phenomena in disordered graphene-based materials. To calculate the conductivity, the Kubo approach considers a small perturbation due to an electric field. Under this perturbation, electrons will propagate along the system as a wave packet.

Considering the frequency-dependent longitudinal conductivity (along the x axis), the Kubo formula is[125]

$$\sigma(\ \ ) = \frac{2\beta\ \ e^2}{\Omega}\ {}^{+}_{-}\quad dE\frac{f(E) - f(E + \ \ \ )}{\ }\mathrm{Tr}\ \ V_x\delta(E - \mathcal{H})V_x\delta(E + \qquad - \mathcal{H}) \tag{2.28}$$

where Ω is the volume of the system, $f(E)$ is the Fermi-Dirac distribution function, V_x is the velocity operator, and a factor of two has been used for the spin degeneracy. In the static electric limit, 0,

$$\sigma_{\mathrm{DC}} = -e^2\ {}^{+}_{-}\quad dE\frac{f(E)}{E}\alpha(E)\lim_{t}\ \frac{\ }{t}\Delta X^2(E\ \ t) \tag{2.29}$$

where $\alpha(E)$ is the density of states

$$\alpha(E) = \frac{\mathrm{Tr}\ \ \delta(E - \mathcal{H})}{\Omega} \tag{2.30}$$

and $\Delta X^2(E\ \ t)$ the mean square spreading of the wave packet

$$\Delta X^2(E\ \ t) = \quad X(t) - X(0)\ {}^{2}_{\quad E} \tag{2.31}$$

whit X the position operator. The zero-temperature limit, $T \to 0$, implies that $-\frac{f(E)}{E} \to \delta(E - E_{\mathrm{F}})$, so that

$$\sigma_{\mathrm{DC}}(E_{\mathrm{F}}) = e^2 \alpha(E_{\mathrm{F}}) \lim_t \frac{1}{t} \Delta X^2(E_{\mathrm{F}}, t) \tag{2.32}$$

This last expression means that $\frac{1}{t}\Delta X^2(E_F, t)$ should converge in the limit $t \to \infty$ to define a meaningful conductivity. Thus, the propagation of the wavepacket needs to establish a saturation regime before the conductivity can be safely calculated.

An efficient real space implementation of the Kubo formula is the one developed by Roche and Mayou.[126] In this approximation, Equation 2.32 is rewritten as

$$\sigma_{\mathrm{DC}} = e^2 \alpha(E_{\mathrm{F}}) \lim_t \left[\frac{1}{t} \left\langle \Delta X^2(t) \right\rangle_E \right] \tag{2.33}$$

and $\left\langle \Delta X^2(t) \right\rangle_E$ is defined as

$$\left\langle \Delta X^2(t) \right\rangle_E = \frac{\mathrm{Tr}\left[\delta(E - \mathcal{H}) \left(X(t) - X(0) \right)^2 \right]}{\mathrm{Tr}\ \delta(E - \mathcal{H})} \tag{2.34}$$

Using the time-reversal symmetry and the fact that trace is permutation invariant, the numerator in the above expression is expressed as

$$\begin{aligned} &\mathrm{Tr}\left[\delta(E - \mathcal{H}) \left(X(t) - X(0) \right)^2 \right] = \\ &\quad = \mathrm{Tr}\ \left(e^{i\hat{\mathcal{H}}t}\ X - X e^{-i\hat{\mathcal{H}}t}\ \right) \delta(E - \mathcal{H}) \left(X e^{-i\hat{\mathcal{H}}t}\ - e^{-i\hat{\mathcal{H}}t}\ X \right) \\ &\quad = \mathrm{Tr}\left[\ X\ U(t)\ \ \delta(E - \mathcal{H})\ \ X\ U(t)\ \right] \end{aligned} \tag{2.35}$$

where $U = e^{-i\hat{\mathcal{H}}t}$ is the time evolution operator. The trace in Equation 2.34 is approximated by the expectation values on random-phase states, which are expanded in terms of all the N orbitals of the basis set

$$_{\mathrm{RP}} = \frac{1}{\sqrt{N}} \sum_j e^{2i\pi\alpha_j}\ _j \tag{2.36}$$

and the spread is finally rewritten as

$$\left\langle \Delta X^2(t) \right\rangle_E = \frac{\left(_{\mathrm{RP}} \left|\ X\ U(t)\ \ \delta(E - \mathcal{H})\ \ X\ U(t)\ \right|\ _{\mathrm{RP}} \right)}{_{\mathrm{RP}} \left| \delta(E - \mathcal{H}) \right|\ _{\mathrm{RP}}} \tag{2.37}$$

The quadratic spread is directly related to the diffusion coefficient through

$$D(E\ t) = \frac{\left\langle \Delta X^2(t) \right\rangle_E}{t} \tag{2.38}$$

whose time dependence fully determines the transport mechanism. A more detailed derivation of the previous formulas and a deeper discussion of the transport regimes is presented in the book by Foa *et al.*[125]

CHAPTER 3

Graphene on h-BN substrate

3.1 Introduction

The Klein paradox is a relativistic process present in graphene in which electrons have a high probability of tunnelling through strong barrier potentials.[127] The consequences of this is that even at the charge neutrality point, where the graphene density of states (DOS) vanishes, there is a minimum of conductivity of $\sigma_{\min} = 4e^2 \ \beta h$,[128] where e is the electron charge and h the Planck s constant. In order to control the transport of carriers in electronic devices based on graphene, a gap must be induced to have the possibility to switch on and off the current. Early theoretical calculations using DFT with the LDA functional, predicted that a gap of about 53 meV will be opened for graphene on h-BN.[129,130] These calculations were done by considering a commensurate structure, where graphene and BN monolayers were forced to have the same lattice constant. The effect induced in graphene by underneath B and N atoms is different for each species, with a lower electrostatic potential in the vicinity of N atoms. Thus, a potential difference is set between the A and B sublattices in graphene breaking the symmetry of the two inequivalent sites and opening a gap. Variations in the stacking configuration of both layers will change the adhesion energy and the magnitude of the gap.

However, no gap was found in early scanning tunnelling microscopy (STM) measurements.[58,61] Instead, the formation of an incommensurate phase coming from the interference pattern of both layers, known as moiré pattern, was observed. These samples present different local

stacking configurations across the structure, inducing different changes in the local potential. If the average of the potential is zero, then no gap is expected. More recent experiments evidenced a controversy about the appearance of a gap in graphene over *h*-BN, since in most of the experiments the preservation of the zero-gap Dirac cone is evident,[58,61,63,64,131,132] while few papers report a clear gap in transport measurements.[62,133] The gap opening in the incommensurate state has been explained in terms of lattice relaxations and strains coming from interactions with the substrate[133–135] and also as a many-body effect.[136]

One of the most remarkable peculiarities of graphene over *h*-BN, is the appearance of new features in the DOS at energies that depend on the size of the moiré.[61] These features correspond to the formation of new Dirac points due to the superlattice potential induced by the *h*-BN substrate.[137,138]

Studies of graphene over *h*-BN within DFT are usually done with small cells (4 atoms per unit cell), and then extrapolations are done to treat larger systems containing up to several thousands of atoms.[136,139,140] Calculations with very high energy resolution have to be done in order to observe the dips that appear in the DOS induced by the *h*-BN substrate. This requires very large *k*-samplings in the Brillouin zone (BZ) to achieve the required resolution, imposing a limitation in the range of moiré systems that can be studied with DFT.

In this chapter, the effects of BN monolayers as a substrate for graphene are studied by means of DFT. Systems with as much as ∼1,000 atoms are considered. DOS with a large number of *k*-points are calculated and changes with respect to pristine graphene are discussed. The electronic band structures and atomic deformations are analysed. Then, estimations to the strength of the potentials and changes in v_F are discussed for graphene monolayers on BN. Finallyn, systems with graphene encapsulated between two *h*-BN sheets are studied.

3.2 Moiré patterns in graphene

The formation of moiré patterns is not exclusive of *h*-BN substrates, and has been observed over many other substrates.[23,24,141–143] In Figure 3.1 a moiré pattern is shown. This pattern is formed as a consequence of the lattice mismatch between graphene, with lattice constant a_0, and the substrate, with lattice constant $a_0(1+\delta)$, and the twist angle between both lattices (λ). The length of the lattice vector of the supercell is denoted as γ and, for triangular superlattices, can be calculated from δ and λ as[61]

$$\gamma = \frac{(1+\delta)a_0}{\sqrt{2(1+\delta)(1-\cos\lambda)+\delta^2}} \tag{3.1}$$

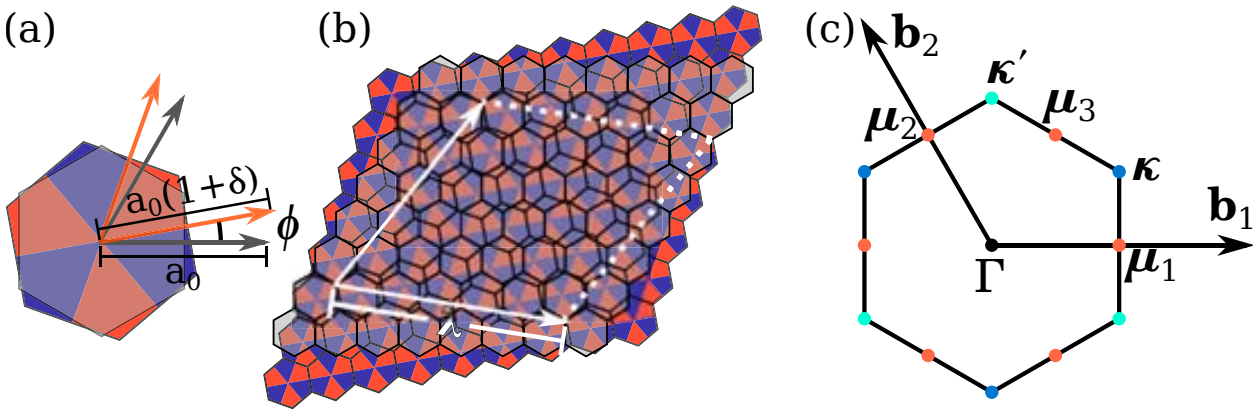

Figure 3.1: (a) Diagram of the unit cells of graphene and h-BN showing the different lattice parameters and the rotational angle ϕ between the layers. (b) Moiré supercell with lattice vectors of length λ. (c) Supercell BZ showing the high symmetry points.

The effect that the substrate has over graphene is that of an external periodic potential that changes the periodicity of the system, from the original honeycomb lattice with two atoms, to a superlattice with many more atoms (up to ∼6,000 C atoms for graphene over BN with $\phi = 0°$). In real samples, the lattice mismatch between graphene on h-BN generally leads to an incommensurate phase. Nevertheless, to study these systems with common DFT codes that use periodic boundary conditions, finite size supercells have to be constructed from an integer number of graphene and h-BN unit cells, enforcing a commensurated structure. Being $\mathbf{a}_1$ and $\mathbf{a}_2$ the lattice vectors of graphene:

$$\mathbf{a}_1 = a_0(1,0) \qquad \text{and} \qquad \mathbf{a}_2 = a_0\left(\tfrac{1}{2}, \tfrac{\sqrt{3}}{2}\right), \tag{3.2}$$

a triangular supercell is defined by the vectors[144]

$$\mathbf{R}_{\mathrm{M1}} = n_1\mathbf{a}_1 + n_2\mathbf{a}_2 \qquad \text{and} \qquad \mathbf{R}_{\mathrm{M2}} = -n_2\mathbf{a}_1 + (n_1+n_2)\mathbf{a}_2, \tag{3.3}$$

where n_1 and n_2 are integers. The wavelength of the moiré pattern can be defined as

$$\lambda = a_0\sqrt{n_1^2 + n_2^2 + n_1 n_2}. \tag{3.4}$$

To construct the moiré patterns for graphene on h-BN, suitable choices of the parameters n_1 and n_2 in Equation 3.3 have to be considered, so that the lattice parameter of h-BN ($a_{\mathrm{BN}} = a_0(1+\delta)$) is kept close to the experimental value of 2.50 Å,[145] while the lattice parameter of graphene is fixed to the experimental value of 2.46 Å. From these considerations, it is clear that only certain angles will be allowed for a certain tolerance of a_{BN}.

It is possible to consider a moiré pattern formed by vectors

$$\mathbf{R}_{\mathrm{M1}} = m_1\mathbf{a}_1 + m_2\mathbf{a}_2 \qquad \text{and} \qquad \mathbf{R}_{\mathrm{M2}} = -m_2\mathbf{a}_1 + (m_1 + m_2)\mathbf{a}_2 \tag{3.5}$$

with m_1 and m_2 being non-integer numbers $m_1 = n_1\ n_{\mathrm{M}}$, $m_2 = n_2\ n_{\mathrm{M}}$, where n_{M}^2 is an integer number. In this case, the supercell is constructed by making a larger supercell with vectors $\mathbf{R}_{\mathrm{SC1}} = n_{\mathrm{M}}\mathbf{R}_{\mathrm{M1}}$ and $\mathbf{R}_{\mathrm{SC2}} = n_{\mathrm{M}}\mathbf{R}_{\mathrm{M2}}$ containing n_{M}^2 moirés. Even when these supercells are larger than the moiré itself, the wavelength γ is still defined by the rotational angle λ and the lattice mismatch δ as in Equation 3.1, satisfying the relation $\gamma = \mathbf{R}_{\mathrm{SC1}}\ n_{\mathrm{M}} = \mathbf{R}_{\mathrm{SC2}}\ n_{\mathrm{M}}$, and the properties of the moiré depend only on γ and not on the size of the supercell. This construction of the moirés is useful to find coincidence lattices to any desired degree of accuracy of λ and a_{BN}, by considering large enough lattice vectors.

High symmetry points for the reciprocal superlattice are defined in analogy to those in graphene. Similar to the inequivalent points $\mathbf{K}$ and $\mathbf{K}$ in graphene, which are located at the corners of the BZ, the points $\boldsymbol{\kappa}$ and $\boldsymbol{\kappa}$ are located at the corners of the superlattice BZ (SBZ), and the three inequivalent $\boldsymbol{\mu}$ points are located at the edges of the SBZ, as shown in Figure 3.1(c). When $2n_1 + n_2$ is a multiple of three, $\mathbf{K}$ and $\mathbf{K}$ are mapped to $\boldsymbol{\Gamma}$. Otherwise, they will be mapped onto $\boldsymbol{\kappa}$ and $\boldsymbol{\kappa}$.

Superlattice potentials in graphene have been extensively studied.[137,138,146–157] In general, the external periodic potential can be expressed as the sum of a symmetric and an antisymmetric parts, which, considering the linear dispersion of graphene near the $\mathbf{K}$ vector, can be included in the low energy Hamiltonian as

$$H = \ v_{\mathrm{F}}\mathbf{k}\cdot\boldsymbol{\sigma} + V(\mathbf{r})\mathbb{I} + \Delta(\mathbf{r})\sigma_z \tag{3.6}$$

where v_{F} is the Fermi velocity,

$$\mathbb{I} = \begin{matrix} 1 & 0 \\ 0 & 1 \end{matrix}$$

is the 2×2 unit matrix, and $\boldsymbol{\sigma} = (\sigma_x\ \ \sigma_y)$ and σ_z are the 2×2 Pauli matrices acting on the A/B sublattice space:

$$\sigma_x = \begin{matrix} 0 & 1 \\ 1 & 0 \end{matrix} \qquad \sigma_y = \begin{matrix} 0 & -i \\ i & 0 \end{matrix} \qquad \text{and} \qquad \sigma_z = \begin{matrix} 1 & 0 \\ 0 & -1 \end{matrix}$$

The term $V(\mathbf{r})$ stands for the symmetric part of the potential, and $\Delta(\mathbf{r})$ is the antisymmetric mass term that breaks the sublattice symmetry. The potentials can be expanded as

$$V(\mathbf{r}) = \sum_{\mathbf{G}} V_{\mathbf{G}} e^{i\mathbf{G}\cdot\mathbf{r}} \qquad \text{and} \qquad \Delta(\mathbf{r}) = \sum_{\mathbf{G}} \Delta_{\mathbf{G}} e^{i\mathbf{G}\cdot\mathbf{r}}$$

where $V_{\mathbf{G}}$ and $\Delta_{\mathbf{G}}$ are the Fourier components of the potential whose magnitudes depend on the modulus of the supercell reciprocal lattice vectors $\mathbf{G}$ alone. External potentials are capable of changing the shape of the Dirac cone renormalizing the Fermi velocity anisotropically. When considering a one dimensional potential, v_{F} becomes lower in the direction perpendicular to the periodicity of the potential.[137,138] For potentials with triangular periodicity, as those present in graphene over BN, the Fermi velocity renormalizes isotropically, and using a perturbative approximation, it can be probed to be[137,152,156]

$$v_{\mathrm{F}}(G_0) \approx v_{\mathrm{F}}^0 \left[1 - \frac{6}{(\ v_{\mathrm{F}}^0 G_0)^2}\left(V_{G_0}^2 + \Delta_{G_0}^2\right)\right] \tag{3.7}$$

where v_{F}^0 is the Fermi velocity of pristine graphene and only the lowest wavelength reciprocal vectors with magnitude $\mathbf{G}\ = 4\beta\quad \overline{3}\gamma \equiv G_0$ have been considered.

For systems where the geometry makes $\mathbf{K}$ to be mapped into Γ, the supercell zone folding gives rise to the appearance of two-fold degenerated states above and below E_{F}, which, assuming a linear dispersion, correspond to energies at the $\boldsymbol{\mu}$ point[61,138,152]

$$E_{\boldsymbol{\mu}} = \pm\ v_{\mathrm{F}} G_0\ \ 2 = \pm 2\beta\ \ v_{\mathrm{F}}\quad \overline{3}\gamma \tag{3.8}$$

Considering the substrate potential as a perturbation, the description of the band dispersion for the above mentioned two-fold degenerated states, can be approximated by an anisotropic two-dimensional Dirac equation at finite energy close to $\boldsymbol{\mu}$ as[152]

$$E_{\boldsymbol{\mu}}(\boldsymbol{\delta}\mathbf{k}) \approx \frac{v_{\mathrm{F}} G_0}{2} \pm \quad \sqrt{4\ {}^2 v_{\mathrm{F}}^2 \delta k_x^2 + \Delta_{G_0}^2 + \frac{16 V_{G_0}^2 \delta k_y^2}{G_0^2}} \tag{3.9}$$

where $\boldsymbol{\delta}\mathbf{k} = \mathbf{k} - \boldsymbol{\mu}$. Note that when $\Delta_{G_0} = 0$ the degeneracy is broken and a gap is opened. Similarly, at $\boldsymbol{\kappa}$ three degenerate levels appear at energies

$$E_{\boldsymbol{\kappa}} = \pm\ v_{\mathrm{F}} G_0\quad \overline{3} = \pm 4\beta\ \ v_{\mathrm{F}}\ \ 3\gamma \tag{3.10}$$

which are split into a singlet and a doublet if $V_{G_0} = 0$, and the doublet is further split if Δ_{G_0} is non-zero.[152] While Equations 3.8 to 3.10 are valid for systems where $2n_1 + n_2 = 3p$, p an integer, similar relations can be found for other geometries.[152]

In graphene over h-BN moirés, the effect of these new Dirac points is reflected as dips at energies that correspond to those of $E_{\boldsymbol{\mu}}$. This has been observed experimentally in the $dI\ \ dV$ curves obtained with scanning tunneling spectroscopy (STS) .[61] As seen in Equation 3.8, the position in energy of these dips comes closer to E_{F} as γ increases. What makes the systems with h-BN specially interesting is that, due to the small lattice mismatch between graphene and h-BN ($\delta = 2\%$), the resulting moirés can have large values of γ ($\sim$14 nm for $\lambda = 0°$)

giving values of $E_{\boldsymbol{\mu}}$ very close to E_{F} ($\sim$0.2 eV for the largest possible moiré of 0°). Even more, the large periodicities of these moiré patterns enables the observation of the fractal spectrum that emerges in presence of a magnetic field: the Hofstadter butterfly,[158] which is a consequence of electrons moving through a periodic potential and a magnetic field. The observation of this spectrum, requires magnetic fields of the order of one magnetic flux quantum ($\Phi_0 = h\ e = 4\,13 \times 10^{15}$ Wb). For ordinary crystals, which are relatively small, that would require the use of very high magnetic fields. However, for the moiré superlattices, because of their large size, the Hofstadter spectrum can be observed with laboratory accessible magnetic fields of 10 30 T.[62–64]

To study the moiré superlattices theoretically

3.3 Systems and geometry specifications

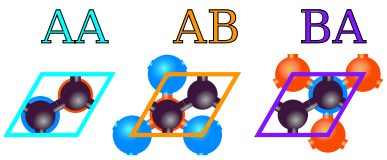

Figure 3.2: Different stack configurations of graphene over h-BN. Black, orange and blue circles represent C, B and N atoms, respectively.

For single cell commensurable graphene over h-BN, the three different stacking configurations considered are shown in Figure 3.2. The AA stacking corresponds to C atoms over B and N atoms; in AB stacking B atoms are below C atoms, and N atoms in the centre of the hexagons of graphene; the BA stacking corresponds to N atoms below C, and B in the centre of C hexagons. These same stackings are present locally in certain regions of the moiré patterns, and local properties of each zone should resemble that of its corresponding single cell system.

DFT calculations are performed for different systems to study the properties of the moiré patterns, which are listed in Table 3.1. There are six systems of graphene on h-BN monolayer, from which five have $n_{\mathrm{M}} = 1$ (22°, 11°, 7°, 5° and 3°), and one has $n_{\mathrm{M}} = 2$ (19°), which corresponds to four replicas of the moiré pattern within the supercell. The atomic structures of the moirés with $n_{\mathrm{M}} = 1$ are shown in Figure 3.3. Encapsulated graphenes are also considered (i.e. graphene between two h-BN monolayers). Taking the system with $\lambda = 22°$ an additional layer of h-BN is added and is denoted with the label 22° 22°. A similar system is constructed with the top layer rotated by $-60°$ (22° $-38°$). Additionally, two systems are constructed with different twist angles for both layers of BN (20° 26° and 6° $-16°$).

DFT calculations are done using norm-conserving Troullier-Martins pseudopotentials.[159] For a good description of the interactions between layers, van der Waals exchange-correlation functional is used with the implementation done by Román-Pérez and Soler[160] in the

SIESTA code.[122] The wavefunctions for the valence electrons are described using a linear combination of pseudo-atomic numerical orbitals with a double-ζ polarized basis (DZP).[123]

For the convergence of the density matrix, a Monkhorst-Pack k-sampling[161] equivalent to a 56×56 sampling in a graphene unit cell is used. To clearly observe the dips in the DOS, a more dense k-mesh is used equivalent to a sampling of 1100×1100 k-points in a unit cell of graphene, and the width of the Gaussian smearing, which defines the energy resolution, set to 6 meV, unless otherwise specified. The specific k-samplings in each system are listed in Table 3.2. Periodic boundary conditions are used, and to avoid interactions between the moirés in the z direction, a vacuum space of >30 Å is imposed.

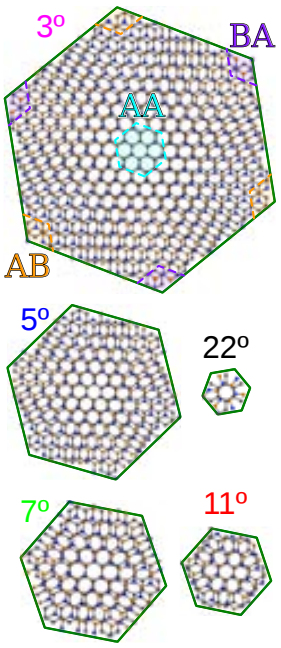

Figure 3.3: Atomic structures of graphene over h-BN with different twist angles. The different stacking zones from Figure 3.2 are sketched for the structure with $\phi = 3°$.

The structures with $\phi \geq 5°$ are relaxed until the forces are smaller than 0.01 eV/Å, while the size of the cell is kept fixed. An ionic relaxation of the 3° system would mean a very expensive calculation. For this reason, the interlayer distance is kept fixed to 3.29 Å in the 3° system, which corresponds to the average separation of the other relaxed systems. For the specific interlayer distance of each system after relaxation see Table 3.3.

3.4 Graphene over *h*-BN monolayer

Single cell systems

From the lattice matched systems shown in Figure 3.2, the most stable one is the AB stacking. The AA and BA stackings are both 20 meV less favourable energetically than the AB stacking. The interlayer distance between graphene and h-BN is 3.33 Å, 3.23 Å and 3.32 Å for the AA, AB and BA stackings, respectively. The average of these interlayer distances is 3.29 Å, which is the same average interlayer distance found in the moiré systems after relaxation. The sublattice symmetry breaking induced by h-BN opens a gap at the

Table 3.1: Specifications of the moiré superlattices studied. The parameters shown are the angle between layers (λ), the moiré wavelength (γ), the lattice mismatch (δ), the BN lattice parameter (a_{BN}), the number of moirés in the supercell (n_{M}^2), the parameters n_1 and n_2 for each layer (G for the graphene layer, BN for the BN layer), the number of atoms per layer and the total number of atoms in the system.

λ (°)	γ (Å)	δ	a_{BN} (Å)	n_{M}^2	Layer	n_1	n_2	Atoms	Total # atoms
22	6.51	0.000	2.46	1	G	1	2	14	28
					BN	2	1	14	
11	13.17	0.018	2.50	1	G	4	2	56	110
					BN	3	3	54	
7	19.53	0.016	2.50	1	G	6	3	126	248
					BN	5	4	122	
5	26.61	0.022	2.51	1	G	9	3	234	458
					BN	8	4	224	
3	41.09	0.020	2.51	1	G	15	3	558	1094
					BN	14	4	536	
19	7.68	0.027	2.53	4	G	5	2	78	152
					BN	3	4	74	
20	7.44	0.008	2.47	7	G	8	0	128	376
26	5.46	0.024	2.52	13	BN1	6	3	126	
					BN2	5	4	122	
6	23.72	0.011	2.49	1	G	7	4	186	550
−16	8.97	0.011	2.49	7	BN1	6	5	182	
					BN2	9	1	182	

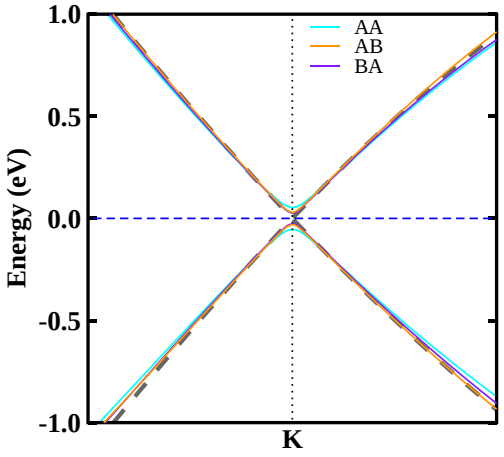

Figure 3.4: Band structure near the **K** point for the systems in Figure 3.2. The dark grey dahsed line corresponds to pristine graphene.

Dirac cone, as can be seen in the band structures of Figure 3.4. The gap depends on the stacking configuration and on the interlayer distance.[129] The resulting gaps are 107 meV, 59 meV and 50 meV for the AA, AB and BA stackings. These gaps are larger than previously reported for the equilibrium interlayer distance due to the smaller separation in our calculations compared to Ref. [129]. Even though, they agree with the corresponding gaps reported by Giovannetti *et al.*[129] for the distances obtained in the present work.

As explained in section 1.1, the band energy of graphene in the linear regime is $E = \pm\hbar v_{\mathrm{F}}|k|$, with the plus (minus) sign corresponding to the conduction (valence) band. The slope of the bands in Figure 3.4 are changed due to changes in the Fermi velocity, being larger in the AB stacking and smaller in the AA stacking. The changes in v_{F} are due to the interlayer interaction, becoming lower for stronger interactions.

Table 3.2: Sampling of k-points for the different systems used in the self-consistent cycle, and in the DOS calculation. The different values n, represent a $n \times n$ sampling in the BZ.

Angle (°)	SCF	DOS
22	21	416
20|26	7	138
19	9	176
11	12	208
7	9	147
6|−16	6	114
5	6	102
3	3	67

Moire pattern systems

The DOS of the different systems of graphene on top of h-BN monolayer show dips at different energies, as seen in Figure 3.5(a). Besides the dips, new van Hoove singularities can be observed around the dips. As expected, the dips in the DOS come closer to E_{F} as the angle between the layers decreases. The wavelength dependence of the energy of the dips can be

seen in Figure 3.5(b), being inversely proportional to the length of the moiré. The values of the energy of the dips follow the relation 3.8 for $E_{\boldsymbol{\mu}}$ in good agreement with experimental data.[61] A notorious discrepancy with the expected value of $E_{\boldsymbol{\mu}}$ is observed for $\lambda = 22°$, in which case, the dip is far from the linear part of the energy dispersion, and the expression for $E_{\boldsymbol{\mu}}$ is not valid any more. The position of the dips for electrons and holes is mostly symmetric with respect to E_{F}, with small variations in energy of at most 19 meV for $\lambda = 22°$. For a better agreement with the energy values of the dip in the DOS, the Fermi velocity is taken as $v_{\mathrm{F}}^0 = 0\ 86 \times 10^6$ m/s. This value is obtained by calculating the band structure of pristine graphene with SIESTA and fitting the bands near E_{F} to a linear relation, and is in good agreement with the single-particle Fermi velocity of graphene.[162]. Due to many-body effects, v_{F} is renormalized to $\sim 1 \times 10^6$ m/s,[9,163] which better fits the experimental data in Ref. [61].

The correspondence of high symmetry points in the BZ between graphene and the superlattices are shown in Figure 3.6(a) and (b) for $\lambda = 22°$, 11° and 7°. The symmetries of the systems with twist angles 5° and 3° are the same as those for 7°. The band structure for $\lambda = 22°$ is shown in Figure 3.6(c). In this case, **K** is mapped to $\boldsymbol{\kappa}$, and **M** to $\boldsymbol{\mu}$. Without the *h*-BN substrate, two-fold degenerated states are present in $\boldsymbol{\mu}$ at energies $-1\ 62$ eV and $+1\ 52$ eV (red lines in Figure 3.6(b)). The superlattice potential breaks these degeneracies by opening a gap of 128 meV in the valence band and 24 meV in the conduction band. Broken degeneracy is also present in $\boldsymbol{\kappa}$ around energies $\pm 2\ 48$ eV where three-fold bands are affected by the moiré potential more strongly in the conduction band than in the valence band. Figure 3.6(d) shows the bands for $\lambda = 11°$. Two-fold degenerate states are observed at $\boldsymbol{\mu}$ around $\pm 0\ 9$ eV (black dashed circle in Figure 3.6(d)). These degeneracies are not broken by the superlattice potential, and the only noticeable effect is a small shift with respect to pristine graphene in the valence bands close to the degeneracy. States of BN appear in the valence band for energies $\lesssim -1\ 4$ eV, and in the conduction band for energies $\gtrsim 3\ 5$ eV. The bands from *h*-BN in the conduction band make difficult to distinguish between graphene and BN states, and hybridizations may occur between bands from both monolayers. At $\boldsymbol{\Gamma}$, six-fold degenerated bands in pristine graphene around $-1\ 62$ eV and $+1\ 52$ eV are split into four and three sets of bands in the valence and conductions bands, respectively, with the two extra bands in the conduction band coming from *h*-BN states. Each set of bands is almost two-fold degenerated at $\boldsymbol{\Gamma}$ with gaps smaller than 9 meV breaking this degeneracy. In the case $\lambda = 7°$, the main Dirac cone is mapped to $\boldsymbol{\Gamma}$ as shown in the band structure of Figure 3.6(e). At $\boldsymbol{\mu}$, two sets of two-fold degenerate levels are present above and below $E_{\boldsymbol{\mu}} \approx \pm 0\ 96$ eV (black dashed circles in Figure 3.6(e)), whose degeneracy is not broken by the underneath BN potential. Around $E_{\boldsymbol{\kappa}} = \pm 1\ 21$ eV (green dotted line in Figure 3.6(e)), two sets of triple degenerate levels appear with broken degeneracy due to the potential. The

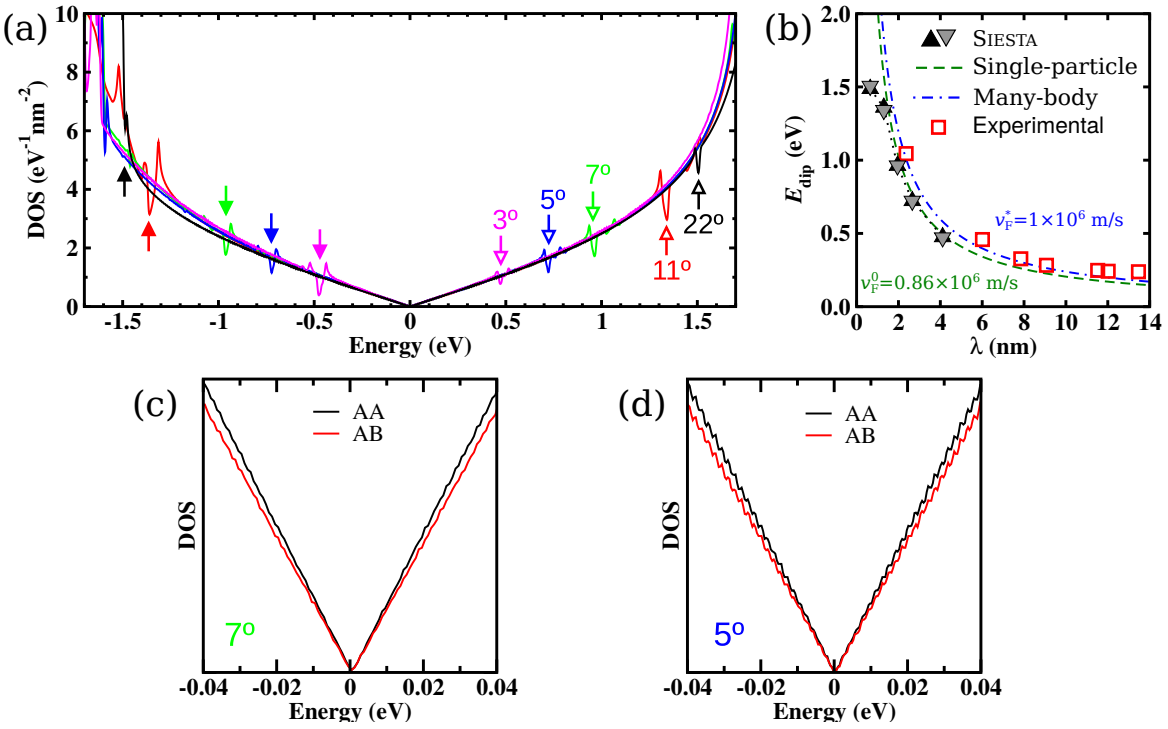

Figure 3.5: (a) DOS for different systems indicating the position of the dips for the different systems with arrows. The resolution of the DOS is 6 meV. (b) Position in energy of the dips taken as the local minimum in the DOS. Black up triangles correspond to dips in the valence band and grey down triangles to dips in the conduction band. For comparison, experimental data from Ref. [61] is shown. The lines represent the dip dependence given by Equation 3.8, taking v_F as the single-particle (green dashed) and many-body (blue dash-dotted) Fermi velocity. (c) PDOS for atoms localized at the AA (black) and AB (red) stacking zones for $\lambda = 7°$. (d) The same as in (c) for $\lambda = 5°$. The resolution of the PDOS is 1 meV.

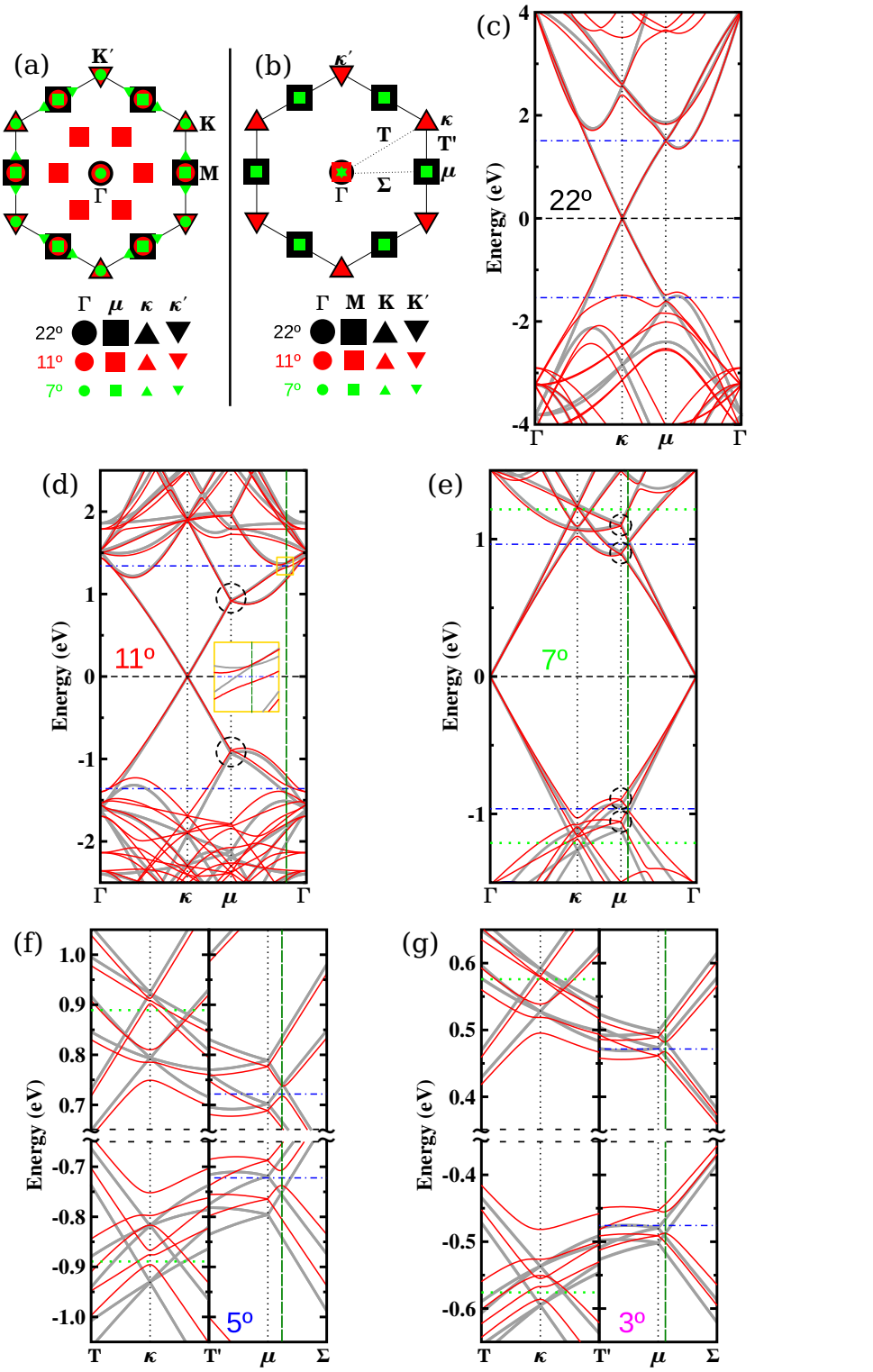

Figure 3.6: (a) BZ of graphene showing the location of high symmetry points of the supercells with twist angles 22°, 11° and 7°. (b) Mapping of high symmetry points of graphene onto the SBZ. Note that the BZ of graphene in (a) and the SBZ of the different systems in (b) are not in the same scale. (c)-(g) Band structure of the different moirés. Horizontal red dash-dotted lines designate the energy of the dips in the DOS. Horizontal light green dotted lines in (e)-(g) denote E_{κ} obtained from Equation 3.10. Vertical dark green dashed lines represent the position where gaps open due to the superlattice potential.

bands for 5° and 3° are shown in Figure 3.6(f) and (g), respectively, close to the $\boldsymbol{\kappa}$ and $\boldsymbol{\mu}$ points. The bands are similar to those of 7° with different energy scales.

The breaking of degeneracies lowers the number of states leading to depletions in the DOS. In the band structures of Figure 3.6, the position of the dips are marked as red dash-dotted lines. While it is considered that the gaps at non-zero energies due to the superlattice potential are located at the edge of the SBZ, of the systems studied here, only for 22° the dip in the DOS comes from broken degeneracy at $\boldsymbol{\mu}$. For $\lambda = 11°$ the only possibility for the origin of the dip occurs close to 1 3 of the $\boldsymbol{\Gamma}$ $\boldsymbol{\mu}$ path. For the conduction band, two-fold degenerate bands are found at this point for pristine graphene supercell, with the moiré potential breaking the degeneracy, as seen in the inset of Figure 3.6(d). For the valence band there is no band crossings, and we could not determine the exact origin of the lowering of states in the DOS, probably coming from bands avoiding each other along the $\boldsymbol{\Gamma}$ $\boldsymbol{\mu}$ path. For $\lambda = 7°$, 5° and 3°, the gap opens close to $\boldsymbol{\mu}$ in the path $\boldsymbol{\mu}$ $\boldsymbol{\Gamma}$. The point in the SBZ where this gap appears moves towards $\boldsymbol{\mu}$ as the angle is decreased, and for larger systems it can be expected to reach $\boldsymbol{\mu}$.

Atomic relaxation leads to in-plane and off-plane displacements in both, graphene and *h*-BN. In Figure 3.7(a), the corrugations of the graphene sheet for the different relaxed systems are shown. The maximum height is observed in the AA stacking zone (0.078 Å in the case $\lambda = 5°$) while the minimum is in the AB stacking zone ($-0\ 146$ Å in the case $\lambda = 5°$). The height of the BA zone is similar to that of the AA zone. In Figure 3.7(c), the maximum and minimum off-plane displacements are shown for each system, and the rms roughness of graphene in each system are listed in Table 3.3. It can be seen that the buckling increases with the size of the moiré, in agreement with experimental observations of graphene over *h*-BN in topographic measurements with STM.[57] For small systems, the stiffness of the sheet only allows a small modulation of the roughness, while in larger systems, since the area of each stacking zone increases, the transition from one zone to the others is softer having more freedom for out-of-plane displacements, and the layers try to reach the equilibrium distance at each zone.

Since both layers are being relaxed, the interlayer distance is not only defined by the off-plane displacements of graphene. In Figure 3.8(a) the interlayer distance for each atom in the graphene layer is shown for the case $\lambda = 5°$. The distance follows the single cell equilibrium separation between layers, with 3.33 Å for the AA stacking, and 3.22 Å for the AB stacking. The interlayer distance, then, has variations of 0.11 Å. The difference in the amplitude of the interlayer distance and the amplitud of the buckling in graphene comes from off-plane displacements in the *h*-BN layer, which can be seen in Figure 3.8(b). The BN sheet remains almost flat except in AB stacking zones, where it moves away from the

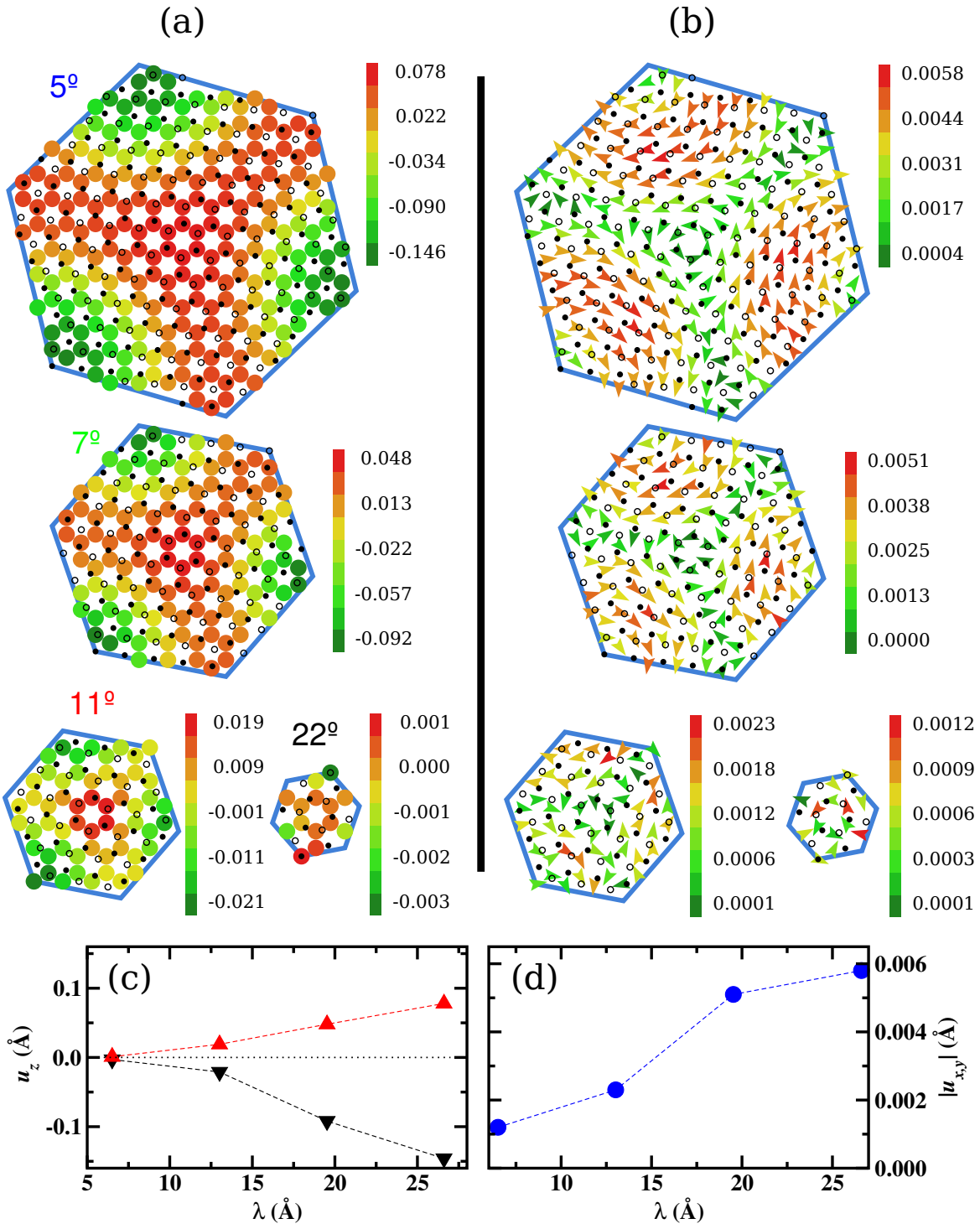

Figure 3.7: (a) Atomic corrugation for the different systems. The values are referenced to the average height of graphene in each case. (b) In-plane atomic displacement for the different systems. Scale bars are in Å. Small black filled circles represent the positions of N atoms, while small empty circles represent those of B atoms. (c) Maximum (red up triangles) and minimum (black down triangles) of the off-plane distortions as a function of the wavelength. (d) Maximum in-plane displacement as a function of the wavelength.

Table 3.3: Interlayer distance between graphene and h-BN layers and the rms roughness of graphene.

Angle (°)	Distance (Å)	RMS roughness (Å)
22	3.293	0.001
19	3.290	0.002
11	3.283	0.010
7	3.284	0.032
5	3.287	0.069

graphene sheet. It would be interesting to see what happens if the atomic positions of the h-BN monolayer are kept fixed, as in the case of a thick h-BN substrate. although this analysis is not presented here.

The atomic in-plane displacements of graphene for the different moirés are shown in Figure 3.7(b). Since the AB stacking is the most stable, atoms at this zone tend to rotate to maximize the area of the AB stacking. This same behaviour was found within the continuum theory of elasticity,[134] although the values of displacement are one order of magnitude smaller in the present work. The displacement of C atoms can become larger if the h-BN layer is not relaxed. Figure 3.8(c) shows that B and N atoms also rotate around the AB zone but in the opposite direction than C atoms, and the in-plane displacements are even larger than in graphene.

To investigate if there are compression and expansion of the graphene lattice depending on the zones of the moiré, the C C distances were analysed, finding that the variations in all zones for $\lambda = 5°$ are less than $\pm 0.1\%$ of the nearest neighbour distance, $d_{CC} = 1\ 42$ Å, showing that no important changes in the local lattice parameter are induced by the superlattice potential. However, for the moirés analysed here ($\lambda \geq 5°$) very small expansions are expected within the continuum theory of elasticity, and the effect could become more important for larger systems with $\lambda < 1°$.[134]

The controversial issue regarding the experimental observation of a gap in graphene over h-BN[62,133] has motivated different explanations. The strain and deformation of graphene lattice are considered to be the most prominent factors in inducing the gap opening.[134–136] Surprisingly, in the case of $\lambda = 5°$, off-plane modulations has variations of up to 0.22 Å without opening a noticeable gap within the DOS resolution of 6 meV (see Figure 3.5(a)). Estimations to the angle dependent gap within the continuum theory of elasticity give values of < 5 meV for $3°$.[134,135] To look for these small gaps, a DOS with more resolution is needed. Calculations of the DOS close to the Dirac point with k-samplings of 712×712 and 882×882 points are done for the systems with 5° and 7°, respectively, with a width of the Gaussians of 1 meV. Even at this resolution, there is no evidence of a gap at zero energy. To analyse

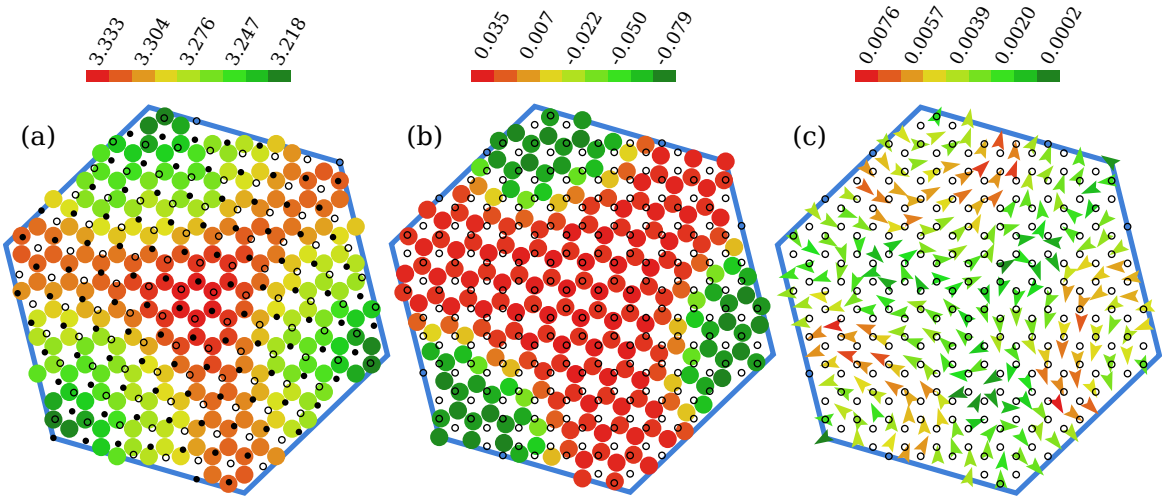

Figure 3.8: (a) Distance of C atoms to the h-BN layer. Small black filled circles represent the positions of N atoms, while small empty circles represent those of B atoms. (b) Off-plane displacement of B and N atoms. (c) In-plane displacement of B and N atoms. In (b) and (c), small empty circles represent the positions of C atoms. Scale bars are in Å.

if local gaps are opened, the projected DOS (PDOS) is obtained for different regions of the moirés considering one hexagon of C atoms at each zone. In the PDOS for the AA and AB stacking regions, shown in Figure 3.5(c) (d), no local gaps can be observed. The slope of the PDOS is different in each region and is related to the strength of the interaction between graphene and the substrate. Considering the relation DOS(E) E v_{F}^2, it follows that v_{F} is larger in the AB zone, while a stronger graphene/h-BN interaction is expected in the AA zone. This agrees with the behaviour of v_{F} for the single cell systems discussed above, and with the experimental observation of space-dependent Fermi velocity in graphene superlattices.[131] The different Fermi velocities can be explained in terms of the corrugation-induced strain[164,165] and v_{F} renormalization due to varying charge concentration.[162] The overall Fermi velocity is also changed depending on the wavelength. As seen in Figure 3.9, the Fermi velocity, measured from the slope of the bands close to E_{F}, decreases as the wavelength of the moiré increases, consistently with experimental observations of v_{F} changes for different moiré angles.[166] The reason for this decrease with the increase of the wavelength is the stronger interlayer coupling for larger moirés. For the case with $\lambda = 3^\circ$ ($\gamma = 41$ Å), the Fermi velocity shown in Figure 3.9 is expected to decrease even more if atomic relaxation is performed.

To quantify the strength of the substrate potential, the values of local energies are used, which can be roughly estimated, in analogy to the Mulliken charges, from[167,168]

$$E_i = \sum_{\nu\eta} \alpha_{\nu\eta} H_{\eta\nu} \tag{3.11}$$

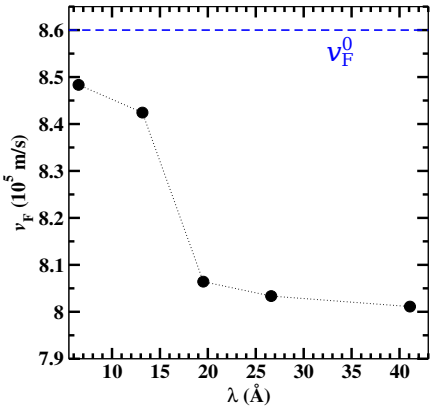

Figure 3.9: Fermi velocity considering moirés with different γ. The blue dashed line represent the Fermi velocity for pristine graphene.

where α is the electronic density matrix, H is the Hamiltonian matrix, ε, η denote localized atomic orbitals, and the sum include all the orbitals ε belonging to atom i. Only changes in the local energies induced by the h-BN substrate are considered by taking $\Delta E_i = E_i^{\mathrm{CBN}} - E_i^{\mathrm{C}}$, where E_i^{CBN} and E_i^{C} denote the local energies on C atoms in the moiré pattern and in isolated graphene, respectively. As an illustration, Figure 3.10(a) shows the energy profile for the moiré lattice with $\lambda = 5°$. This energy profile can be decomposed, following Equation 3.6, into a symmetric and an antisymmetric part. The antisymmetric part Δ_i can be obtained by calculating the difference in energy for the A and B sites within each unit cell of the moiré, and the symmetric part is therefore $V_i = \Delta E_i - \Delta_i$. The profile of the antisymmetric part of the potential is shown in Figure 3.10(b). From the profiles, intensities of the potential for each part can be obtained. One very simple model for such potentials was proposed by Sachs *et al.*[139] by considering $\Delta(\mathbf{r})$ as a sum of sine functions

$$\Delta_i = \frac{1}{2}\left[A\sin(2\beta x_i + \quad _1) + B\sin(2\beta y_i + \quad _2) + C\right] \tag{3.12}$$

where x_i and y_i are the relative position of atom i within the moiré cell, A and B are the amplitudes of the potential and C is the average of the energy difference between A and B sublattices, and is related to the gap of the system. Similarly, the symmetric part can be represented with the same functional form with parameters A^*, B^* and C^*, where A^* and B^* are the amplitudes and C^* represent a rigid shift in energy, which is found to be 0 for all the systems. Table 3.4 shows the values of the amplitudes for the symmetric and antisymmetric parts for different rotation angles. The strength of the potential increases with the wavelength of the superlattice due to the stronger interlayer coupling for larger systems. The parameter C remains always small, with vanishing values for 7° and 5°.

Lets focus now on the system with $\lambda = 19°$ and $n_{\mathrm{M}}^2 = 4$. Figure 3.11(a) shows the atomic

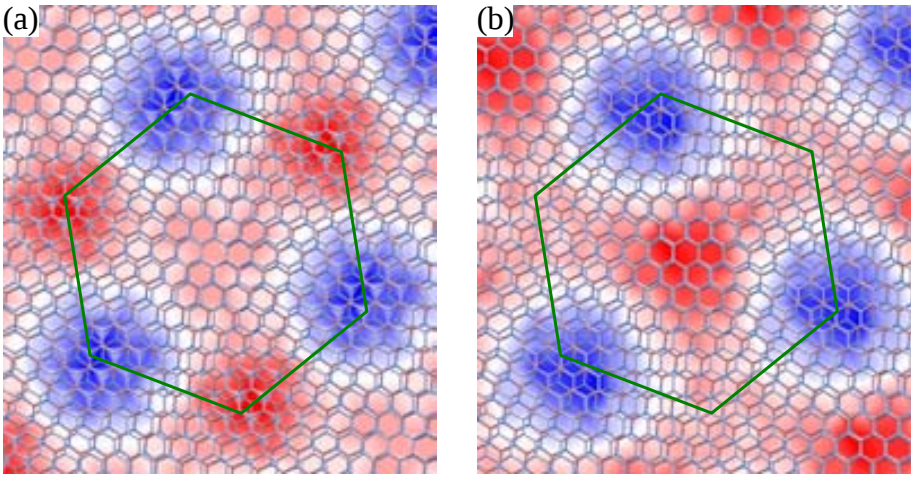

Figure 3.10: Profile of the symmetric (a) and antisymmetric (b) parts of the superlattice potential for $\lambda = 5°$.

structure indicating the different stacking zones. Since $n_{\mathrm{M}}^2 = 4$, four zones with each type of stacking are present in the supercell. Note that at the centre of the superlattice where one would expect to find the AA stacking, the large twist angle completely distorts the stacking and, even though the graphene and *h*-BN hexagons are one over the other, carbon atoms do not eclipse none of the B or N atoms. The other AA zones are located at the edges of the supercell, and in none of them a well defined AA stacking is observed. This is also the case for the AB and BA stackings. For each stacking type, the four zones along the supercell are dissimilar, but all of them resemble the corresponding stacking configuration. As can be observed in Figure 3.11(b), the DOS for this system does not show the clear dips seen for the other systems. A closer look reveals small features, as can be seen in the inset of Figure 3.11(b). These features have different energies for the valence and conduction bands. The energy for the valence band feature is -1 14 eV and that for the conduction band is 1.42 eV. The small dip in the valence band is more closely related to the periodicity of the supercell (15.36 Å), while the dip in the conduction band can be attributed to the periodicity of the moiré (7.68 Å). This can be seen more clearly in Figure 3.11(c), where a comparison is made with the dips of the others systems. The dip from the moiré potential is weak because the moiré symmetry is broken by the differences of the four zones of each type in the supercell. Since by construction a supercell periodicity is imposed, a fictitious dip

Table 3.4: Potential strength obtained from a fit of the local energies.

Angle (°)	A (meV)	B (meV)	C (meV)	A^* (meV)	B^* (meV)
22	17	14	6	3	7
11	28	25	2	11	9
7	34	34	0	13	10
5	39	39	0	17	17

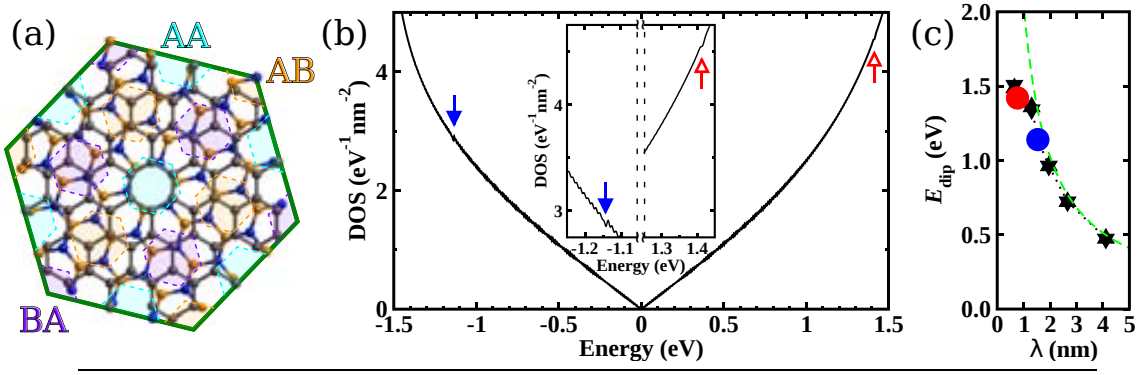

Figure 3.11: (a) Atomic diagram of the system with $\phi = 19°$. (b) DOS for $\phi = 19°$. The inset shows a zoom in to the zones marked with arrows. (c) Position in energy of the features from the DOS in (b). The wavelength of the feature in the valence band (blue circle) is taken as the size of the supercell, while for the feature of the conduction band (red circle) is taken as the size of the moiré.

appears corresponding to this superperiodicity. Hence, for real samples with large angles, the observation of the dips problematic not only because they appear at high energies, but also because the disorder within the moiré blurs their effect in the DOS. As the angle is decreased, different stacking zones of the same type become more alike and the effect of the moiré is enhanced affecting the electronic structure of graphene dramatically.

3.5 Encapsulated graphene

In many experiments, graphene is deposited over h-BN and then covered again with h-BN, leaving both layers at different angles with respect to the graphene lattice. The effect of encapsulated graphene is studied in this section. The systems 22°|22° and 22°|−38° are similar, except that B and N are interchanged one of the layers, so that for 22°|22°, B atoms are over B and N over N, while in 22°|−38°, B atoms are over N atoms. The DOS of the two systems are compared with the DOS of the non-encapsulated moiré in Figure 3.12(a). As can be seen in the inset, the dips in the DOS become deeper due to the enhanced potential of the two layers of h-BN that further increases the gap opening at . For the dip in the conduction band, there is a shift in its position due to a decrease in v_F, observed as an increase in the slope of the DOS that lowers the energy of the dip ($E \propto v_F$, DOS $\propto 1/v_F^2$). The dip in the valence band is hindered by BN bands and the effect of encapsulation is more difficult to see. There is little difference in the DOS of both encapsulated systems, with a small enhancement of the dips in the 22°|22° system, since the potential of both h-BN sheets are in phase.

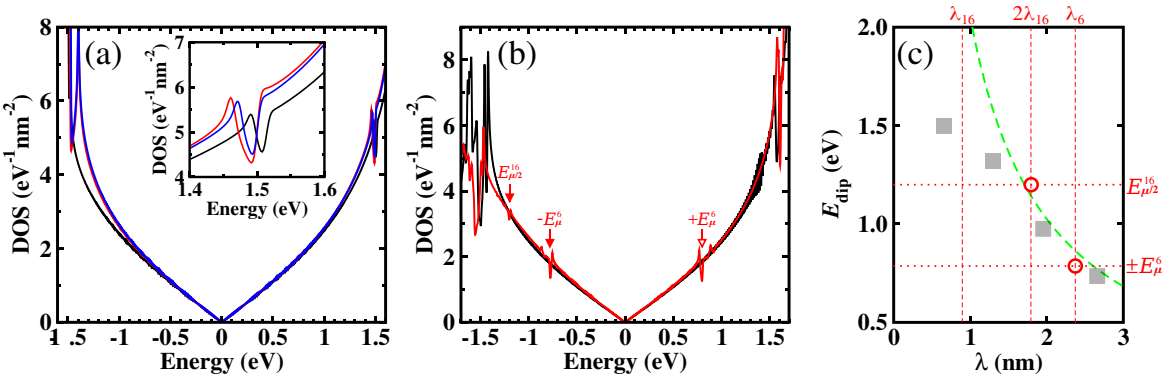

Figure 3.12: (a) DOS of the systems 22° (black), 22°|22° (red) and 22°|−38° (blue). The inset is a zoom in to the dip in the conduction band. (b) DOS of the systems 20°|26° (black) and 6°|−16° (red). (c) Position of the dips present in the DOS of the system 6°|−16°. Horizontal dashed lines correspond to energies of the dips. Vertical dashed lines represent different characteristic wavelengths of the system. Green dashed line represents the relation in Equation 3.8. Grey squares are the positions of the dips for the systems in Figure 3.5(b).

The DOS for the systems 20°|26° and 6°|−16° are shown in Figure 3.12(b). For these systems two dips are expected coming from both moiré patterns. In the case of the system 20°|26°, the energies at which the dips should appear according to Equation 3.8, are 2.8 eV for 20° and 3.8 eV for 26°, far above the linear regime of the band dispersion. At these high energies, a dip induced by the *h*-BN substrate would be difficult to observe since there appear bands from BN and C σ-orbitals. In the DOS of 20°|26°, strong features can be seen around ±1.5 eV. As in the case of the non-encapsulated system with 22°, lower dip energies could be expected. Even though, the observed features can hardly be attributed to the dips from the moiré superlattice, because similar features can be observed in other systems at the same energies. In the case of 6°|−16°, similar depletions are present close to ±1.5 eV. The dip corresponding to −16° is difficult to identify due to its high energy as in the case of the 20°|26° system. The dip that corresponds to the periodicity of the layer with twist angle of 6° is clearly seen. Unexpectedly, another dip appears at an energy that does not correspond to any of the two periodicities. In Figure 3.12(c), it can be seen that this dip can be related to an artificial periodicity twice as large as the one of −16°.

In Figure 3.13(a) and (b) the atomic structure of the system 6°|−16° is shown, along with the different stacking zones related to each of the two *h*-BN sheets. The off-plane atomic displacements of this systems is shown in Figure 3.13(c). The displacements are smaller than in the cases of non-encapsulated graphene (compared to 5° or even 7°), since there is a compromise between the coupling of graphene to both *h*-BN layers. Graphene is closer to the 6° sheet in zones that correspond to AA stacking for −16° and AB stacking for 6°; and detaches from the 6° sheet in some zones close to AB stackings of the −16° sheet.

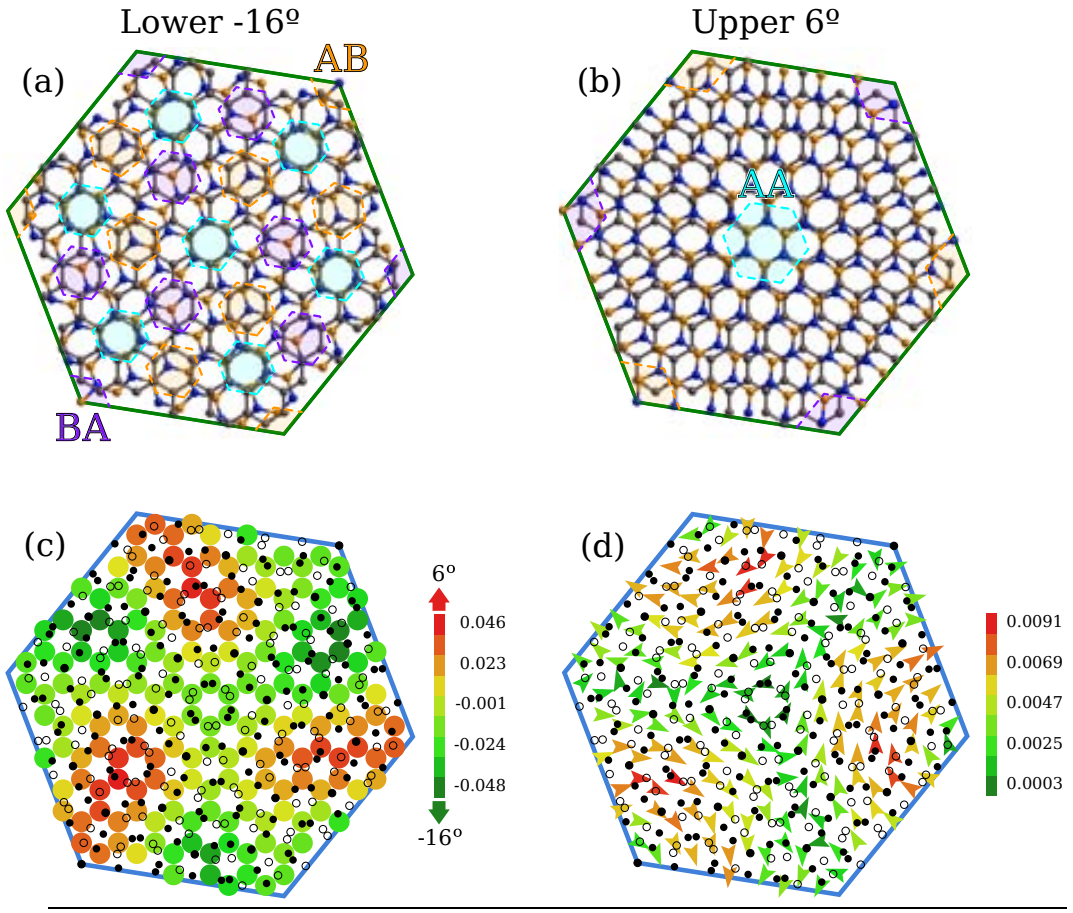

Figure 3.13: (a) and (b), atomic diagram of the system 6°|–16° showing the lower and upper layer of *h*-BN, respectively. (c) Off-plane displacements of graphene in 6°|–16°. Positive values correspond to graphene approaching the 6° layer, while negative values correspond to displacements closer to the −16° layer. (d) In-plane displacements of 6°|–16°. In (c) and (d), small black filled circles represent the positions of N atoms, while small empty circles represent those of B atoms. Scale bars are in Å.

Figure 3.13(d) shows the in-plane atomic displacements for the system 6°|−16° is shown. Opposite to off-plane displacements, in-plane displacements are greatly enhanced compared to non-encapsulated systems. The maximum displacements occur around the AB stacking zone of the 6° sheet.

3.6 Conclusions

DFT calculations were done for moiré superlattices with different twist angles. The most interesting systems are those with small angles where larger interlayer coupling and lattice deformations can change the properties of graphene more dramatically.[133 135] However, angles close to zero represent a great challenge for DFT calculations because the number

of atoms can increase to several thousands of atoms. Modern approaches for the calculation of large systems with thousands of atoms are useful to overcome these problem, like the PEXSI technique implemented in SIESTA.[169] Unfortunately, at the present time this methodology lacks k-sampling, which is mandatory if such important features of the DOS are to be analysed. Furthermore, to observe fine details in the DOS, like the dips induced by underneath h-BN, large k-samplings are needed to achieve high energy accuracy.

The dips in the DOS appear due to broken degeneracies at superlattice Dirac points. Unlike the main Dirac point at **K** in pristine graphene, which corresponds to the dispersion of massless particles,[9] the new Dirac points at finite energies do exhibit gaps, thus, representing the dispersion of massive relativistic particles.

Structural relaxations are quite significant leading to off-plane and in-plane modulations of the atomic displacements up to 0.2 Å. Although when the buckling is important, no gap opens at zero energy. However, many-body effects may play an important role in these systems,[136] making conventional DFT unable to describe correctly the moiré superlattices, and many-body corrections must be included, as those provided by the GW approximation.

The parametrization of the moiré potential is very useful to model in a simple way the effect of the h-BN substrate. The parametrization could be used, then, in large scale calculations within TB to study larger systems than those allowed with DFT. Although the substrate induced potential is not the only important effect in the moiré superlattices, it is a good starting point to model graphene over h-BN. Other parameters, like β σ hybridizations due to curvature, or hopping renormalizations could also be obtained from DFT data.

CHAPTER 4

Transport in moiré patterns

4.1 Introduction

The low-energy physics of graphene has drawn attention since its discovery.[6,9] In presence of electron-hole puddles (produced by screened trapped charges), the electronic conductivity exhibits an almost temperature independent minimum at the Dirac point which contradicts the scaling theory of localization in two-dimensional systems.[170] This theory establishes a dependence between the conductance and the size of the system in disordered systems, and for two-dimension (2D) excludes a metallic state.[171] Although h-BN couples only weakly to graphene, the 1.8% lattice mismatch between them, and any rotational orientation of their lattices give rise to moiré patterns that have been observed by scanning tunnelling microscopy (STM).[58,61] The presence of these patterns suggests that h-BN generates a superimposed periodic potential on graphene, significantly modifying its electronic spectrum, as evidenced by the formation of two electron-hole symmetric high-energy secondary Dirac points.[138] These superlattice features have been observed as dips in the density of states (DOS) with scanning tunnelling spectroscopy (STS), revealed in both atomic scale spectroscopic (STS) measurements[61] and as peaks in the resistivity in mesoscopic transport measurements.[62–64,172] These same measurements revealed the fractal spectrum that arises in presence of an external magnetic field: the Hofstadter butterfly.[158] The zero-field resistivity fingerprints of those secondary Dirac points remain however elusive, varying significantly from sample to sample, with values ranging from a few kΩ to about 15 kΩ. The

ratio between primary and secondary Dirac point resistivity is also not understood, sample-dependent, and the effects of disorder induced localization effects have not been studied.

Anderson localization can emerge in strongly disordered systems where charge carriers are trapped by the highly scattering medium, and the only allowed diffusion is via *quantum jumps*.[173] The conditions that induce this type of localization have been studied in graphene and graphene nanoribbons.[174] The model is based on a random distribution of impurities

4.2 Tight binding model for moiré superlattices

The effect from a substrate of *h*-BN is represented by adding superlattice terms to the Hamiltonian. One very important term for the construction of an effective Hamiltonian is a modulated potential that has the same periodicity of the moiré. In general, this potential has two components: a symmetric and an antisymmetric part with respect to sublattice sites (see Equation 3.6). Both parts are related to the formation of new Dirac points and renormalization of the Fermi velocity (v_F),[137,138,152,156] while the antisymmetric part has the additional effect of opening local gaps,[139] and breaking degeneracies in the band structure,[152] which cause the appearance of dips in the DOS. The symmetric part can be considered as additional disorder and, for simplicity, only the antisymmetric potential is considered here.

The moiré potential can be included in the Hamiltonian as a mass term:

$$H = \sum_{\alpha} \left({}_0 + \tfrac{1}{2}\pi\Delta_\alpha \right) \alpha \quad \alpha + \gamma_0 \sum_{\alpha\,\beta} \alpha \quad \beta \tag{4.1}$$

where α represents localized orbitals, ${}_0$ is the on-site energy (taken as zero), $\gamma_0 = 2\,7$ eV is the hopping parameter and $\pi = 1$ ($\pi = -1$) for A (B) sublattice. Δ_α is the moiré potential, which is considered to have the simple form proposed by Sachs *et al.*:[139]

$$\Delta_\alpha = A \sin\left(\frac{2\beta x_\alpha}{\gamma} + \lambda_1\right) + B \sin\left(\frac{2\beta y_\alpha}{\gamma} + \lambda_2\right) + C \tag{4.2}$$

where x_α and y_α are the components of the position of orbital α , considered to be along the lattice vectors of the supercell and γ is the wavelength of the moiré. The parameters A and B are the amplitudes of the potential, and C is the average value of the modulated mass term and is related to the band gap width of the system. The parameters λ_1 and λ_2 represent phases related to the relative displacement of graphene and *h*-BN layers and have no important influence in the modelling of the moiré superlattices.

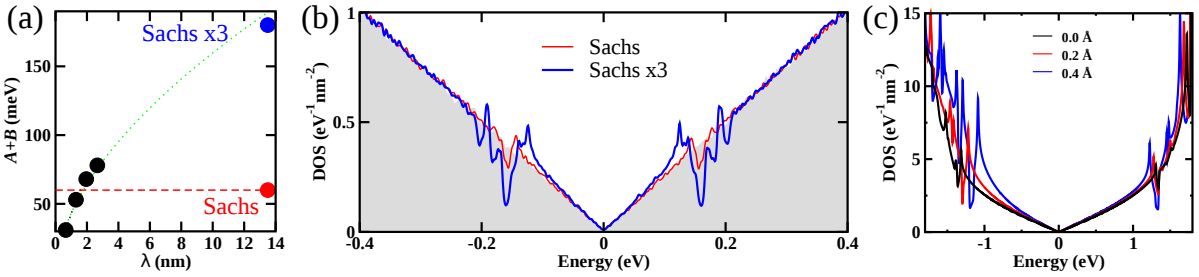

Figure 4.1: (a) Amplitudes of Δ_α taken as $A + B$, as a function of the moiré wavelength. Black circles correspond to DFT local energies. Red circle represents the value for the largest moiré ($\sim$ 13 5 nm) given in Ref. [139], and the blue circle is this same value multiplied by 3. Dotted green line is a power law fitting with $y = 43\ 5x^{0\ 56}$. (b) DOS computed from the TB model including the moiré potential. The values of the amplitude are those of the original paper[139] (red line) and with a threefold magnification (blue line). The filled grey curve represents the DOS for pristine graphene. (c) DOS from DFT considering $\lambda = 11°$, and reducing the interlayer distance by 0 Å (black), 0.2 Å (red) and 0.4 Å (blue), with respect to the equilibrium distance.

In chapter 3, moirés with different wavelengths were considered using DFT. The wavelengths of the moirés are defined by the rotation angle between graphene and h-BN (λ), and the lattice mismatch ($\delta = a_0\ a_{\mathrm{BN}} - 1$, a_0 and a_{BN} are graphene and h-BN lattice constants, respectively). In order to obtain an energy landscape of the moiré patterns, local atomic energies were obtained for systems with twist angles of 5°, 7°, 11° and 21°. From these landscapes, the amplitudes of the potential were extracted finding that the strength of the potential is wavelength-dependent. The amplitudes obtained are shown in Table 4.1 and plotted in Figure 4.1(a). The value of C is found to be very small, and therefore taken as $C = 0$ unless stated otherwise. As the wavelength increases, the interlayer coupling increases resulting in stronger potentials, and the amplitude easily becomes larger than previously reported.[139]

Secondary Dirac points are more easily accessible by gating when they occur at energies close to the Fermi energy, E_{F}. Since the position in energy of these secondary Dirac points (E_{dip}) is angle dependent, increasing with larger angles, it is better to focus on the transport properties of the graphene/h-BN structure with the largest possible moiré periodicity, i.e. when $\lambda = 0°$, which has a wavelength of $\sim$ 13 5 nm. This system is out of reach for first principles simulations since it represents a structure with around 12,000 atoms. For this system, Sachs *et al.*[139] proposed the values $A = 18\ 6$ meV and $B = 42$ meV, which were obtained from DFT calculations considering a single cell of graphene on top of h-BN with different stacking configurations. The supercell potential from DFT local energies, calculated in the previous chapter, shows that the amplitudes are larger even for the system with $\lambda = 5°$, which is considerably smaller than that with $\lambda = 0°$. Using a power law

Table 4.1: Potential strength obtained from a fit of the DFT local energies of systems with different twist angles.

Angle (°)	A (meV)	B (meV)
22	17	14
11	28	25
7	34	34
5	39	39

fitting, the amplitudes of the system with $\lambda = 0°$ are estimated to have a strength of the modulated mass term three times larger than the amplitudes in Ref. [139] (see Figure 4.1(a)). To better contrast the superlattice potential effects with experimental transport data, the values $A = 56$ meV and $B = 126$ meV are hence used in the TB model. Notice that in STM measurements, the tip can induce a compressive strain, which is found to increase the effect of the superlattice potential, as shown in Figure 4.1(c). Here, the DFT DOS is calculated for a moiré with $\lambda = 11°$. As the interlayer distance is reduced, the dips become deeper and the van Hoove singularities around the dips more pronounced. A reduction in v_{F} due to the enhancement of the substrate potential, leads to a shift in energy of the position of the dips, becoming closer to E_{F}. Additionally, the potential becomes stronger due to encapsulation of graphene within h-BN layers, as explained in chapter 3 (see Figure 3.12(a)). Such variability in the values of A and B translates into changes in the depth of the dips in the DOS related to the secondary Dirac points, which is demonstrated in Figure 4.1(b).

4.3 Computational methodology

Transport calculations are done following the Kubo-Greenwood formalism using a real-space implementation that has been validated for disordered graphene calculations.[174,175] The quantum wave packet dynamics and Kubo conductivity are calculated using the order N Lanczos approach.[125,174–176]. The DC-conductivity $\sigma(E\ t)$ for energy E and time t is given by

$$\sigma(E\ t) = e^2 \alpha(E) \Delta X^2(E\ t)\ t \tag{4.3}$$

where e is the electron charge, $\alpha(E)$ is the DOS and $\Delta X^2(E\ t)$ is the mean quadratic displacement of the wave packet at energy E and time t, given by

$$\Delta X^2(E\ t) = \frac{\mathrm{Tr}\left[\delta(E-H)\ X(t) - X(0)\ ^2\right]}{\mathrm{Tr}[\delta(E-H)]} \tag{4.4}$$

A key quantity in the analysis of the transport properties is the diffusion coefficient $D(E\ t) = \Delta X^2(E\ t)\ t$. $D(E\ t)$ exhibits different regimes depending on the nature of the studied

system. In the diffusive regime, a transition from a short-time ballistic motion to a saturation regime occurs, giving a maximum in $D(E\ t)$. The mean free path, $_e$, is extracted from

$$_e(E) = \frac{D^{\max}(E)}{2v(E)} \tag{4.5}$$

where $v(E)$ is the initial velocity of the wave packet derived at short times. The maximum of the diffusion coefficient, $D^{\max}(E)$, can also be obtained in systems that present localized regimes, in contrast to ballistic systems, where no maximum is found. In the localized regime, contributions from quantum interferences are evidenced by a time-dependent decay of $D(E\ t)$ for long elapsed times. The semi-classical conductivity is given by

$$\sigma_{\rm sc} = \frac{1}{2} e^2 \alpha(E) D^{\max}(E) \tag{4.6}$$

and the semi-classical resistivity $R_{\rm sc} = 1\ \ \sigma_{\rm sc}(E)$. The spin degree of freedom is included as a factor of two for σ and α. The length of the moiré superlattice is taken to be $55a_0 = 13\ 5$ nm. The entire simulation system considered is constructed by repeating the moiré cell 60 times in each direction, which gives a total of 21,780,000 atoms, and a length of the simulation cell lattice vector of ~ 812 nm. The energy resolution of the different quantities calculated is 0.54 meV. The number of recursion steps used in the Lanczos method is 4,000, while the number of Chebyshev polynomials to represent the time evolution operator is 110.

To represent the disorder in the graphene sample, an additional random modulation of the potential profile is introduced on top of the above described TB model by taking on-site energies at random within $[-W\gamma_0\ \ 2\ \ W\gamma_0\ \ 2]$, a common model for short range scattering potentials.[170,177] A strength of $W = 0\ 5$ is considered for Anderson disorder. The Gaussian potential is defined by a chosen density of Coulomb impurities (0 125%) and a long range scattering potential, following commonly used parameters to mimic screened charges trapped in the substrate.[175,178–181] The contributions from $N_{\rm I}$ impurities randomly distributed at positions $\mathbf{r}_i$ is given by renormalized on-site energies at orbital α with

$$_\alpha = \sum_{i=1}^{N_{\rm I}} \epsilon_i e^{-\frac{|\mathbf{r}_\alpha - \mathbf{r}_i|^2}{2\xi^2}} \tag{4.7}$$

where $\pi = 0\ 426$ nm, defines the effective potential range, while ϵ_i are chosen at random within $[-W\gamma_0\ \ 2\ \ W\gamma_0\ \ 2]$, with W monitoring the total disorder strength. Two representative values, $W = 1$ and $W = 2$, are chosen to introduce weak and strong intervalley scattering, respectively. The results presented are obtained by averaging over six different random configurations, both for Anderson disorder and Gaussian impurities. Note that the energy scales for the disorder considering the Anderson model ($\sim$0.67 eV) and the Gaussian model (2.7 eV) are much larger than the modulation of the symmetric part of the moiré

potential $V(\mathbf{r})$ in Equation 3.6 (34 meV, for 5°), which can therefore be neglected as an additional long-range and sublattice-symmetric contribution. The same criterion cannot be applied to the antisymmetric part, since its effect is not hidden except for very large values of W, as shown below.

4.4 Mean free path

Figure 4.2 compares the mean free paths computed for graphene on top of h-BN and without the moiré potential, both with superimposed short range Anderson (a) and long range Gaussian disorder potentials (b). The mean free paths, in both types of disorder, are generally lower in presence of the moiré potential, being this more clearly seen away from E_{F}. Peaks can be observed at energies $\pm E_{\mathrm{dip}}$, with a more prominent amplitude in the case of short range disorder, becoming even larger than in the case without the h-BN potential. Notice that for most of the chosen disorder parameters, localization effects remain extremely weak, as evidenced by a saturation behaviour of the diffusion coefficient shown in the inset of Figure 4.2(a) for the case of Anderson disorder. For the Gaussian disorder with $W = 1$, the diffusion remains ballistic for $E = 0$ and diffusive for $E = E_{\mathrm{dip}}$ (see Figure 4.5(b)). For a stronger disorder, an almost energy-independent $_e(E) \sim 10$ nm is obtained as seen in Figure 4.2(b) for Gaussian impurities and $W = 2$. For such disorder strength, as seen in the inset of Figure 4.2(b), the diffusion coefficient shows strong decay after reaching its maximum value, pinpointing the emergence of quantum interferences.

For 2D systems, it is expected a localized behaviour to emerge at long enough length scales.[182] Even for small disorder, the perturbative localization length is estimated as π_{loc} $_e \exp(\beta\sigma_{\mathrm{sc}}\ G_0)$,[174,182] where G_0 is the conductance quantum. For the moiré superlattices with low enough disorder, the transport regime at the secondary Dirac points as well as at the primary Dirac point remain far from a strong insulating regime given the large values of the $_e(E)$ [80 nm 1 ϵ m]. The estimations suggest localization lengths of several microns. Therefore, a description of the temperature-dependent conductivity within the Mott s variable-range hopping model is limited to very small temperatures.[183]

4.5 Resistivity

The corresponding behaviours of the semi-classical resistivity are reported in Figure 4.3. The changes of the mean free path in the vicinity of the high-energy Dirac points are transformed into a reinforcement of the resistivity, which stems from the strongly reduced DOS. In addition to the standard zero-energy peak of the longitudinal resistivity, two satellite

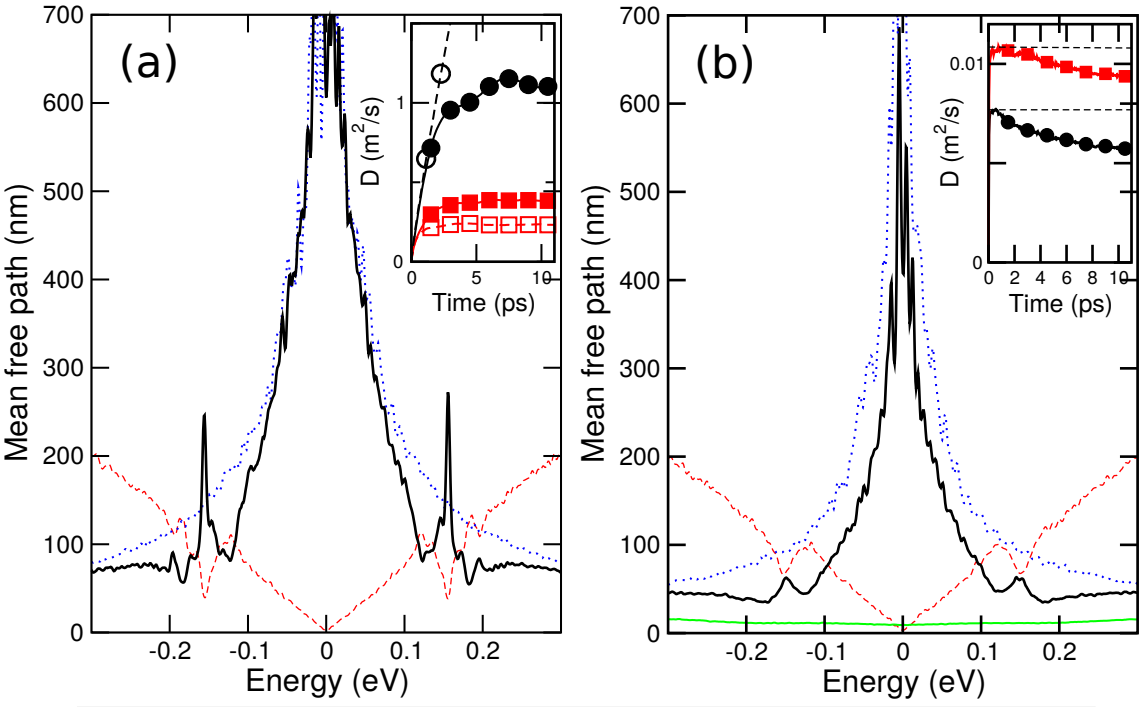

Figure 4.2: Mean free path for disordered graphene without (dotted blue) and including the moiré potential Δ_α. (a) Case with Anderson disorder for $W = 0\,5$ (solid black), and (b) Gaussian long range disorder for $W = 1$ (solid black) and $W = 2$ (solid green). Rescaled DOS are shown as dashed red lines. Inset (a): $D(E = 0\ t)$ (black circles) and $D(E = E_{\text{dip}}\ t)$ (red squares) for Anderson disorder with moiré potential (filled) and without moiré potential (empty). Inset (b) : $D(E = 0\ t)$ (black circles) and $D(E = E_{\text{dip}}\ t)$ (red squares) for the case $W = 2$. The dashed lines correspond to the maximum diffusion for each case.

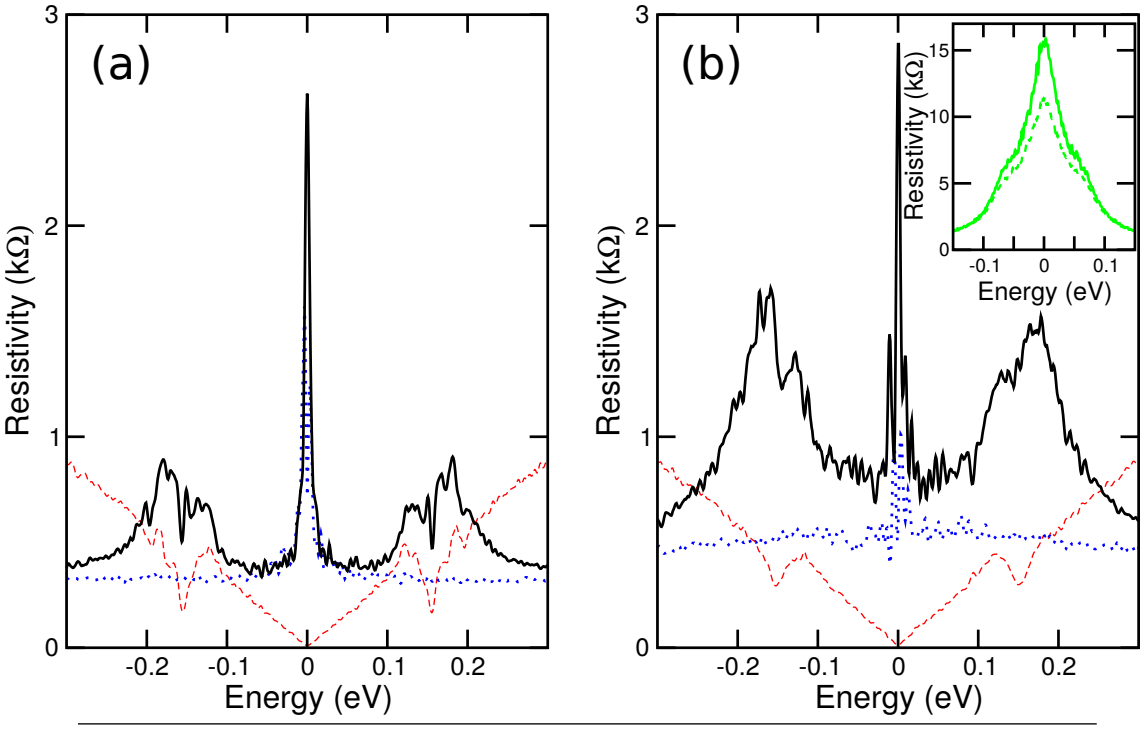

Figure 4.3: Resistivity with (solid black) and without (dotted blue) moiré potential. (a) Case with Anderson disorder ($W = 0\,5$). (b) Case with Gaussian potential ($W = 1$). The rescaled DOS is shown for comparison (dashed red). Inset (b): Resistivity for the case $W = 2$ using the semiclassical expression (dashed) and the quantum resistivity at time $t = 10$ ps (solid).

resistivity peaks are formed in presence of the substrate-induced moiré potential, in clear agreement with experimental results.[62–64]

The satellite resistivity peaks remain therefore observable as long as quantum interferences are negligible, whereas the emergence of localization effects is concomitant to the vanishing of transport signatures of the secondary Dirac points. This can be seen when varying the disorder strength from $W = 1$ to $W = 2$. For $W = 2$, as seen in the inset of Figure 4.2(b), the diffusion coefficient exhibits a marked time-dependent decay after initial saturation, evidencing the significant contribution of quantum interferences induced by intervalley scattering.[184] The corresponding resistivities reported in the inset of Figure 4.3(b), show no traces of secondary Dirac point, but an increasing resistivity with enhancement of coherent localization effects (dashed line gives R_{sc} whereas solid lines denotes the quantum resistivity computed at a length scale longer than $_e$, that is including localization contribution).

An increase in disorder translates into a degradation of the moiré fingerprints in the resistivity close to the secondary Dirac points. Eventually, the dips in the DOS can not be seen for both, Anderson and Gaussian disorders, as shown in Figure Figure 4.4(a) and (b), respectively. This enhancement of disorder brings reinforcement of quantum interferences

and localization effect. For Anderson disorder (Figure 4.4(a)), it can be seen a shift in E_{dip}, coming from the reduction of v_{F} as the disorder increases. In Figure 4.4(c) the resistivity is plotted for different values of W considering Gaussian disorder. The enhancement of the resistivity comes with a broadening of the principal peak that eventually eclipses the features at the dip energies. Figure 4.4(d) shows the quantum resistivity for short and long times. The time of 1 ps corresponds to the maximum of the diffusion coefficient at the main Dirac point. At this energy the resistivity increases for long times due to quantum interferences, while at the energy of the secondary peaks the quantum effects are not important.

To address the dependence of the results with the strength of the potential, parameters that correspond to a weaker mass term modulation ($A + B = 80$ meV) are also considered. The resistivity considering these parameters is shown in Figure 4.4(e) (red line). The effect of the moiré potential is still notorious even with these smaller amplitudes. The intensity of the resistivity peak at the main Dirac point is comparable to that of the secondary peaks. Although the fingerprints remain, the values for the peaks in the resistivity are smaller to those reported experimentally.[63,64,172]

4.6 Effect of a band gap

The possible formation of a band gap is a debated issue, both experimentally and theoretically. Although, Hunt *et. al.*[62] reported transport measurements in moiré patterns of graphene on h-BN with small twist angles that suggest an angle-dependent band gap opening of up to 30 meV, the work by Ponomarenko *et al.*[64] does not support the idea of band gaps induced by the superlattice potential.

In absence of many-body corrections, commensurate layers are predicted to exhibit large band gaps due to AB sublattice symmetry breaking, in the order of 30 meV.[129] On the other hand, in the incommensurate case the gap is found to be considerably small.[139,155] As discussed in the previous chapter, DFT calculations for the moiré patterns studied do not show traces of any significant gap opening due to the underlaying h-BN monolayer. The contribution of many-body effects reinforces the formation of a wider band gap in single cell systems, which has been extrapolated to larger supercells.[136] More work is needed to confirm the global modifications of the graphene band structure in presence of the moiré potential and accounting for many-body corrections (such as those which go beyond standard DFT, including the GW corrections), although the computational cost of such calculations makes this unfeasible at this time for large moiré supercells. Another explanation to the gaps observed experimentally, are lattice distortions in graphene,[133–135] arising from a

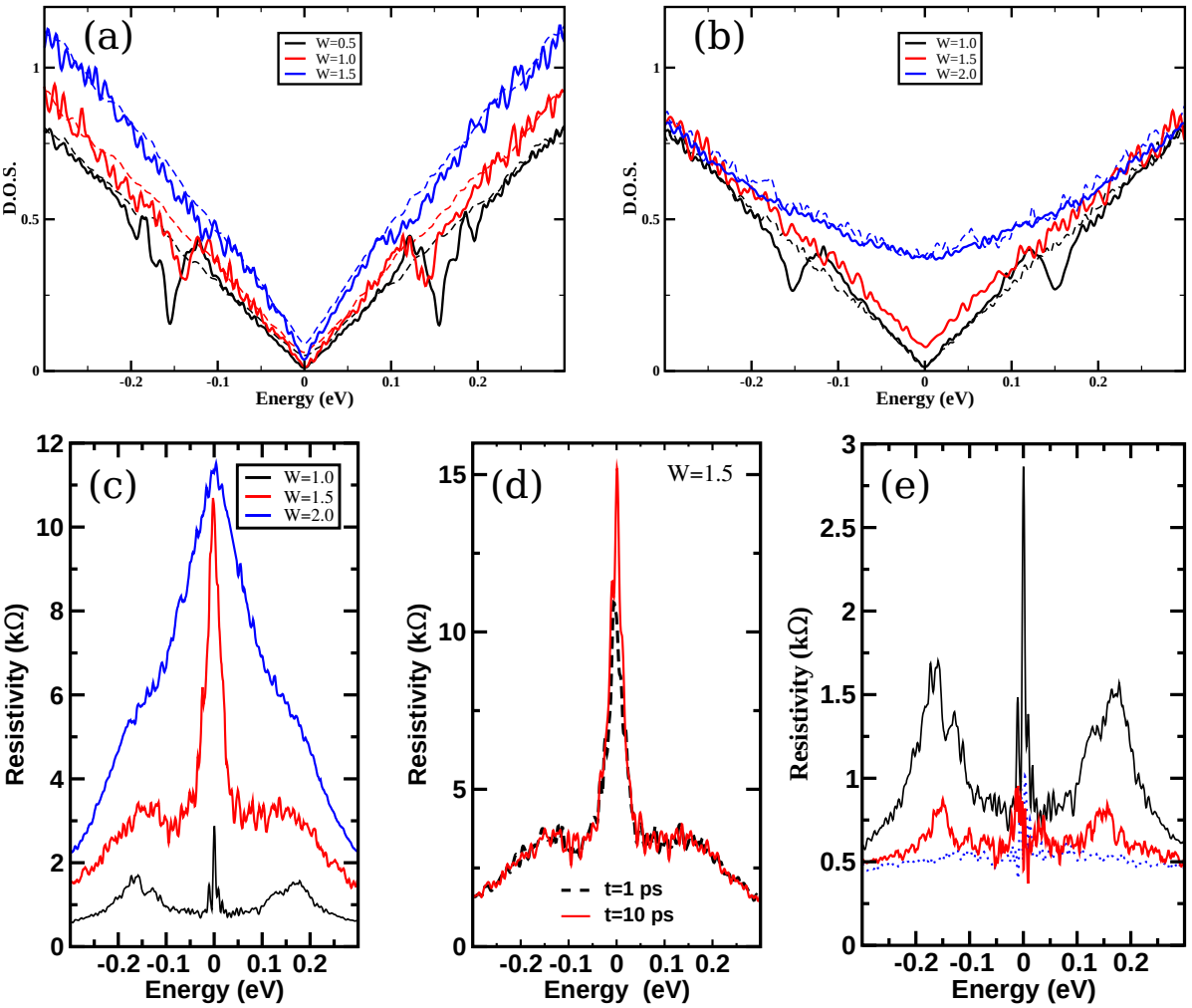

Figure 4.4: (a) DOS for the case with Anderson disorder, considering different strengths of the disorder: $W = 0\,5$ (black), 1.0 (red) and 1.5 (blue). (b) DOS for the Gaussian potential, with values of the disorder strength of $W = 1\,0$ (black), 1.5 (red) and 2.0 (blue). Dashed lines are the DOS for disordered graphene without the moiré potential. (c) Semi-classical resistivity considering Gaussian long range potential with $W = 1$ (dashed blue), $W = 1\,5$ (solid red) and $W = 2$ (dotted black). (d) Kubo conductivity at $t = 1$ ps (red) and $t = 10$ ps (black), with Gaussian disorder and $W = 1\,5$. (e) Semi-classical resistivity considering Gaussian long range potential with $W = 1$. Dotted blue corresponds to the case without moiré. Solid red line is the resistivity using the original values of the potential from Ref. [139], while solid black is the system with values of the amplitude three times larger.

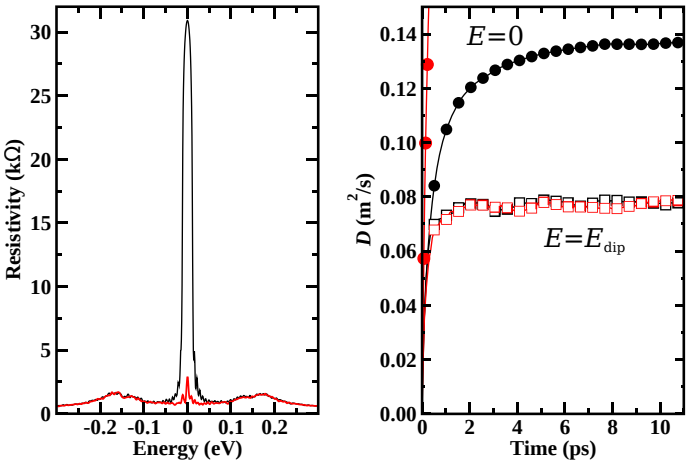

Figure 4.5: (a) Semi-classical resistivity with Gaussian long range potential for $W = 1$, and considering $C = 0$ meV (red) and $C = 30$ meV (black). (b) Diffusion coefficients for gapped (black) and ungapped (red) systems for energies $E = 0$ (circles) and $E = E_{\text{dip}}$ (squares).

competition between elastic and adhesion energies, becoming more important in systems with small misalignment angles ($< 1°$).

Within the model of modulated potential used here, the parameter C is responsible for the gap opening. To explore the consequences of a small gap in graphene under the moiré potential induced by h-BN, a finite value for C of 30 meV is considered. As seen in Figure 4.5(a), the opening of a gap primarily affects the principal peak at the Dirac point, increasing the resistivity around this energy by one order of magnitude, while the features around the secondary resistivity peaks remain mostly unchanged. In Figure 4.5(b) the diffusion coefficients for systems with and without a gap are shown. At the main Dirac point, the diffusion changes from the ballistic regime to the diffusive regime as an effect of the finite gap. On the other hand, the diffusion coefficients at the energy of the dips remains the same if non-zero values of C are considered.

4.7 Effect of a magnetic field

The effect that a static magnetic field has in graphene on top of h-BN is discussed in the following. A magnetic field perpendicular to the plane of graphene is applied and varied up to ∼12 T. The DOS at each value of the magnetic field is calculated. The obtained spectra are shown in Figure 4.6. The usual Landau levels from graphene are clearly observed. Additionally to these Landau level, more features appear due to the effect of the substrate potential. It can be distinguished four additional sets of lines, two in the valence band, and two in the conduction band, represented as red and green line in Figure 4.6(f). The sets above and below E_{F} are symmetric, and we focus in the part of the spectrum below

the Fermi level (Figure 4.6(b) and (d)). The red line in Figure 4.6(f) represents gaps that correspond to the dip in the DOS at zero field. This gap is split and has a linear dependence with the magnetic field. The green lines are originated from Van Hove singularities close to the dip at zero field. Their dependence with the magnetic field is also linear. Massless relativistic particles under the effect of a magnetic fields have an energy dependence that is quadratic, as observed for the main Landau levels of graphene. On the other hand, features in the spectrum coming from the substrate potential, do not behave as massless Dirac fermions. This is evidence that gaps opening at non-zero energies, has to be described as non-relativistic (Schrodinger) particles.

The effect of disorder is also considered by adding to the on-site energies the effect of long range Gaussian potential, with a strength of $W = 1$. As in the case of the DOS at zero field, the features of the superlattice potential are blurred and for strong disorders it is expected that the fingerprints of the moiré pattern are completely erased.

4.8 Conclusion

Fundamental transport features in graphene induced by a Moiré superlattice potential have been unravelled. At the energy of the superlattice (secondary) Dirac points, an increase of both the mean free paths and resistivity has been obtained, confirming experimental data but also quantifying the role of superimposed disorder in tuning the relative resistivity between primary and secondary Dirac points. The long localization lengths deduced from the mean free path indicate a modest contribution of quantum interferences and weak intervalley scattering. In contrast, whenever static disorder leads to mean free paths in the order of 10 nanometers, sizable quantum interferences develop and jeopardize the identification of satellite resistivity peaks.

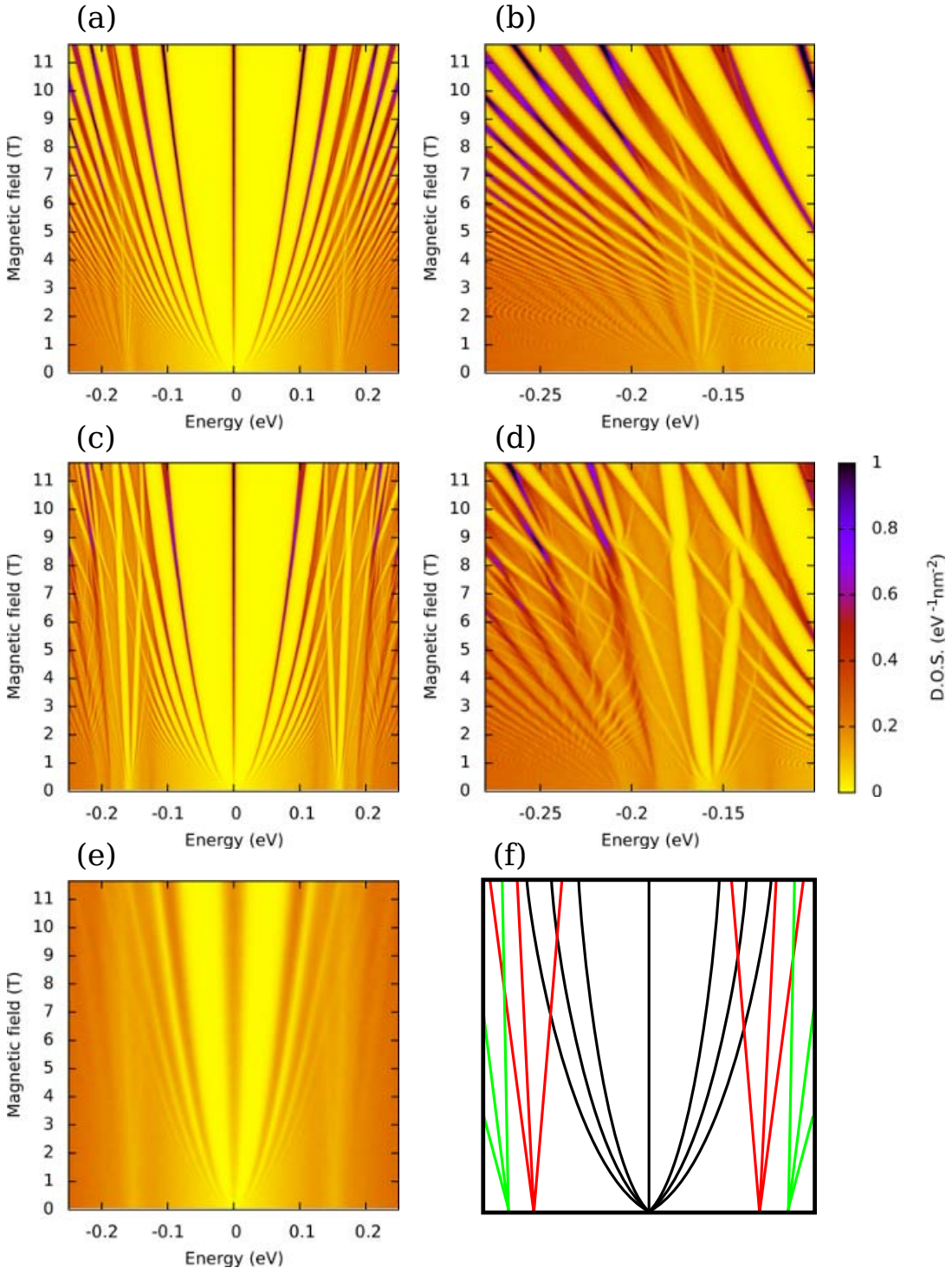

Figure 4.6: Hofstadter butterflies spectrum of moiré superlattice under the effect of a magnetic field for different values of the intensity of the potential. (a) and (b) $A + B = 60$ meV. (c)-(e) $A + B = 180$ meV. (b) and (d) are zoom in to the zone of the dip in the conduction band of (a) and (c), respectively. In (e), besides the moiré potential, Gaussian disorder with $W = 1\,0$ is included.(f) Schematic representation of the features in the spectrum. Black lines: relativistic Landau levels from graphene. Red lines: gaps from the superlattice potential. Green lines: Landau levels from the superlattice potential.

CHAPTER 5

Tight binding model for coplanar hybrids

5.1 Introduction

The intrinsic properties of graphene make it a promising material for technological applications in electronics.[185] In order to use graphene as the principal component in devices traditionally fabricated with semiconductors, the semimetallic condition of graphene must be lifted. There are several forms to induce a gap, from which superlattice patterning[50,53] and dimensional confination[186,187] are some examples. Etching techniques are a common strategie to design antidot superlattices and nanoribbons (NR) to induce a gap in graphene.[188–191] The threshold for the resolution in these techniques is the design of features as small as ∼10 nm. Patterning graphene in a smaller scale is difficult with this approach and even if it becomes possible in the future, the obtained structures would be mechanically unstable and difficult to manipulate.

Another method to open a gap is to embed graphene into another supporting material. Graphene and h-BN have very similar lattice parameters (2.46 Å for graphene and 2.50 Å for h-BN) making them compatible for the synthesis of heterostructures. In recent years, the improvement of growth techniques, principally by chemical vapour deposition (CVD), has allowed the synthesis of coplanar hybrid sheets of graphene and h-BN.[98–100,103,104] Remarkably, using this same technique, graphene NR (GNR) can be obtained embedded in a BC_2N alloy, with widths of the ribbons of ∼5 Å.[106] Theoretically, graphene/h-BN hybrid systems have probed to be capable of tuning the gap of graphene, becoming larger

as the concentration of BN increases.[92,94,192] Also, it has been found that the properties of these hybrids depend on the geometry of the interfaces. For triangular domains of h-BN on graphene, the system becomes metallic, as this geometry introduces holes or electrons, depending on whether B or N are in excess.[92,93] The effect of doping comes with the appearance of partially filled bands that can give rise to magnetic ordering at the interface C atoms.[92,93]

Interfacial effects have a primal role in graphene/h-BN heterostructures. The modelling of such systems is important to understand and explore the properties that arise with different concentrations and geometries. Since the characteristics of these hybrids are sensitive to interface termination, a suitable theoretical model to describe all the cases is valuable.

The objective of this chapter is to get a tight binding (TB) model capable of describing in-plane interfaces between graphene and h-BN. To understand the phenomena that take place in these interfaces, the properties of edge states in GNR and boron nitride NR (BNNR) are first revised in section 5.2. The form of the TB Hamiltonian and how to obtain it from DFT calculations is then discussed in sections 5.3 and 5.4. In section 5.5, a TB model for pristine graphene and h-BN is obtained, while in section 5.6 the model is extended to hybrid systems, studying several cases of these systems.

5.2 Edge states in graphene and h-BN nanoribbons

Just as in bulk materials the presence of surfaces is unavoidable (as infinite crystals do not exist), in two-dimensional (2D) materials, the appearance of edges is inevitable and at the nanoscale the properties of these edges can become dominant over the whole structure. In honeycomb lattices, the basic shapes of the edges are zigzag and armchair, depending on the crystallographic direction of the edge. As shown in Figure 5.1(a), the direction of zigzag edges is $\mathbf{a}_{\mathrm{Z}} = -\mathbf{a}_1 + \mathbf{a}_2$, and that of armchair edges is $\mathbf{a}_{\mathrm{A}} = \mathbf{a}_1 + \mathbf{a}_2$. All other edge shapes, referred as chiral edges, can be modelled as a combination of zigzag and armchair edges. Therefore, by studying the basic types of edges we expect to be able to make a generalisation for any other shape.

If the dimension of the layer is reduced to a one-dimensional (1D) system, by further cutting the layers exposing two edges, nanoribbons are obtained. In Figure 5.1(b) NR with the two basic edge shapes are shown. The lowering of dimensionality comes with the appearance of new properties mostly determined by the kind of termination of the edges, which can become dominant over the properties of the inner part of the layer when the thickness of the ribbon is sufficiently small. Hence, an important structural parameter is the width of

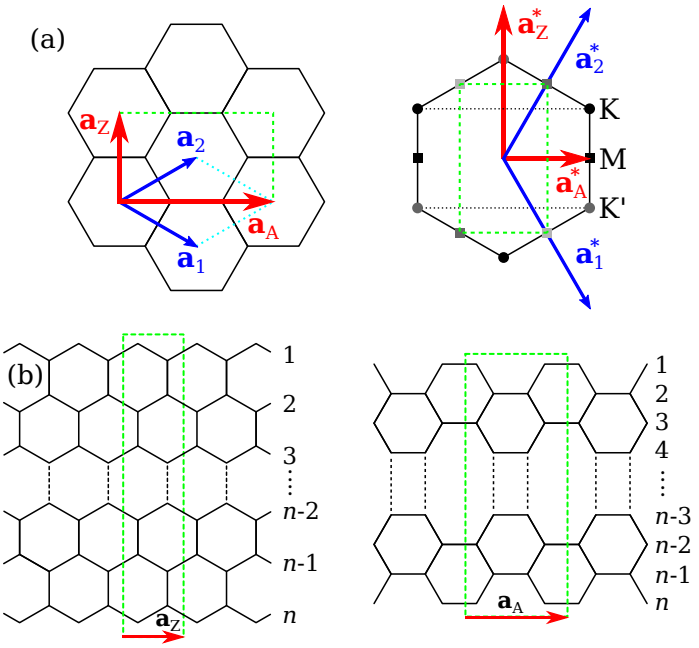

Figure 5.1: (a) Unit cells of an hexagonal lattice in real (left) and reciprocal (right) space. Blue arrows represent lattice vectors and red arrows are the directions of periodicity of zigzag ($\mathbf{a}_Z$ $\mathbf{a}^*_Z$) and armchair ($\mathbf{a}_A$ $\mathbf{a}^*_A$) ribbons. (b) Schematic of NR with zigzag (left) and armchair (right) edges. The parameter n refers to the number of chains in the ribbon. The unit cells are marked with a green dashed box, and the lattice vectors with red arrows.

the ribbon, characterised by the number n of dimers that form the chains of atoms (see Figure 5.1(b)).

The Brillouin zone (BZ) of the NR is defined by the 1D reciprocal vector, whose orientation is determined by the edge type. In Figure 5.1(a), the real space unit cell and the first BZ of an hexagonal lattice are shown. For armchair ribbons, the reciprocal lattice vector ($\mathbf{a}^*_A$) is in the direction of the **M** point. In the case of zigzag ribbons, the reciprocal lattice vector ($\mathbf{a}^*_Z$) is in the direction of the **K** point.

Unlike CNT, where there are families of metallic and semiconductor tubes depending on the chiral direction,[186] GNR lose the semimetallic character and are all semiconductors.[187,193,194] The dependence of the gap with the width of the ribbon varies with the edge type. For armchair GNR (AGNR) three families can be distinguished with different width dependences.[187] As seen in Figure 5.2(a), the families are sorted depending on n: the gap is smallest for ribbons satisfying $n = 3p+2$, p a positive integer; becomes larger for the $n = 3p$ family; and is largest when $n = 3p + 1$. As p increases, independently of the family, the gap tends to zero corresponding to the limit of semimetallic graphene. For zigzag GNR (ZGNR), the gaps are smaller than AGNR and also tend to zero for wider ribbons, as shown in Figure 5.2(b). Even though the **K** point of graphene is in the $\mathbf{\Gamma}$ **X** path of ZGNR, with $\mathbf{X} = \mathbf{a}_Z$ 2, the semimetallic character is lost by electron-electron interaction at the

edges, leading to a gap opening and the appearance of magnetic coupled states between the edges.[187,195,196] The band structure of a ZGNR with $n = 8$ is shown in Figure 5.2(d). The bands are all spin-degenerated though edge states for each spin are spatially separated at each edge. The magnetic ground state, shown in Figure 5.2(c), is antiferromagnetic where spins at each edge have the same alignment but with antiparallel orientation between edges. When applying an in-plane homogeneous electric field $\mathcal{E}$, as the one shown in Figure 5.2(c), the resulting potential difference ($\Delta V = \mathcal{E} w_{\mathrm{Z}}$) across the ribbon shifts the bands near the Fermi level (E_{F}) The effect of this shift is shown schematically in Figure 5.2(e) (yellow arrows). The right edge (β-spin occupied) is shifted to lower energies, since the potential is negative in that zone. In the same manner, the left edge (α-spin occupied) is shifted to higher energies. The result is a gap opening of the β-spin band while the gap of the α-spin band decreases. For sufficiently strong electric field, the unoccupied α-spin band, located at the right edge, starts to populate with electrons completely closing the gap for one of the spins (α), while for the other (β) the bands remains as a semiconductor.[197] This peculiar behaviour is known as half-metallicity, and has an important role in spin-based electronics, or spintronics,[198] making GNR potentially useful for new devices and applications.

In h-BN NR (BNNR), besides the edge states of the ribbons, the polarization plays an important role. In Appendix B, expressions for the formal bulk polarization, $\mathbf{P}_{\mathrm{bulk}}$, are introduced. Taking electrons as point charges located at their corresponding Wannier centres (see Appendix A for an introduction to Wannier functions), it is possible to define a set of *Wannier ions*,[120] from the nominal valence charge placed at the positions of each ionic core within the crystal. Considering this for h-BN, the charge of B is $+3e$, and that of N is $-3e$. $\mathbf{P}_{\mathrm{bulk}}$ is a multivalued quantity, since there are infinite many choices for the unit cell and the basis of atoms. In Figure 5.3(a), three different unit cells for h-BN are shown, and their corresponding values of polarization are presented in Figure 5.3(b). In presence of edges, the bound charge is calculated as $\sigma_b = \mathbf{P}_{\mathrm{bulk}} \cdot \mathbf{n}$, where $\mathbf{n}$ is a vector normal to the edge, and $\mathbf{P}_{\mathrm{bulk}}$ is calculated taking a conveniently chosen unit cell. For the cell used in zigzag BNNR (ZBNNR), shown in Figure 5.3(c), the polarization is $\mathbf{P}_{\mathrm{bulk}} = e\ a_0(\ \overline{3}\ 1)$, where a_0 is the lattice constant. This type of ribbons have the edges terminated with different species, one with B and the other with N. Thus, the bound charge has opposite signs at each edge, with values $\sigma_b = \pm 1e\ a_0$. In the case of armchair BNNR (ABNNR), $\mathbf{P}_{\mathrm{bulk}} = e\ a_0(0\ -2)$, and the edge is perpendicular to the polarization, as shown in Figure 5.3(d), resulting in a non-polar edge.

ZBNNR can present metallic states if bare edges are considered.[199–201] This give raise to magnetic ordering at the edges, with the ground state, shown in Figure 5.3(e), being antiferromagnetic at the B edge, and ferromagnetic at the N edge.[200–202] The metallicity disappears by passivating the edges, becoming insulators with a decreasing gap for wider

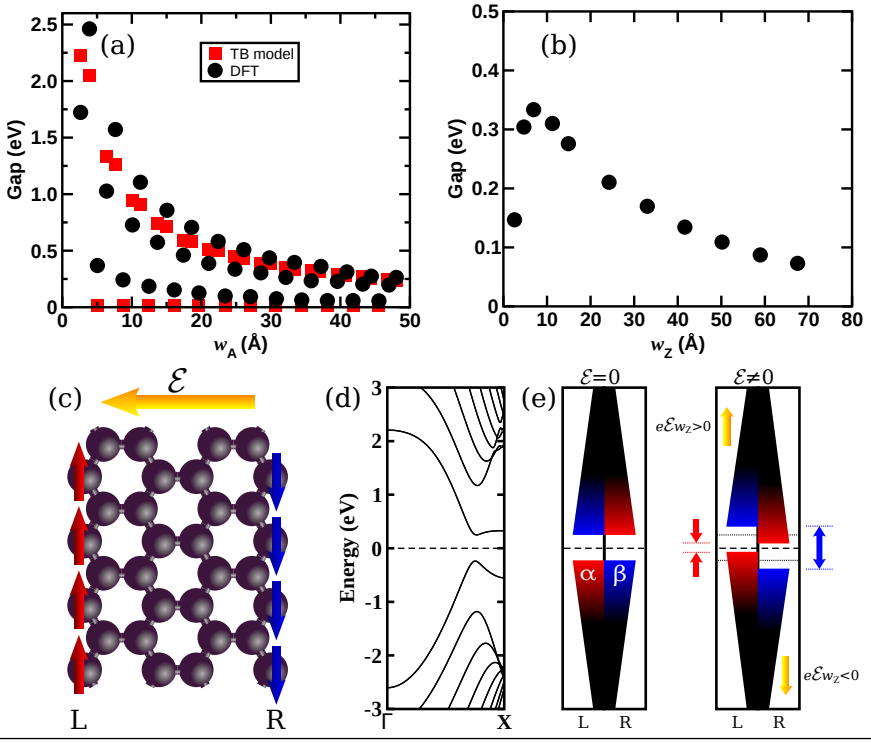

Figure 5.2: (a) Band gaps for AGNR with different widths $w_A = na_0\ \ 2$, using TB and DFT. (b) Band gaps for ZGNR using DFT, with widths $w_Z = \ \ \overline{3}na_0\ \ 2$. Data in (a) and (b) taken from Ref. [187]. (c) Magnetic ground state for ZGNR. Red arrows denote α-spin localized edge states, while blue arrows denote the same for β-spin. The yellow arrow indicate the direction of the in-plane electric field $\mathcal{E}$. (d) Band structure of a ZGNR with $n = 8$. (e) Schematic partial DOS for the left (L) and right (R) edges in (c), with red zones denoting α-spin only states, blue zones β-spin only states, and black zones spin degenerated states. The cases with $\mathcal{E} = 0$ (left panel) and $\mathcal{E} = 0$ (right panel) are presented.

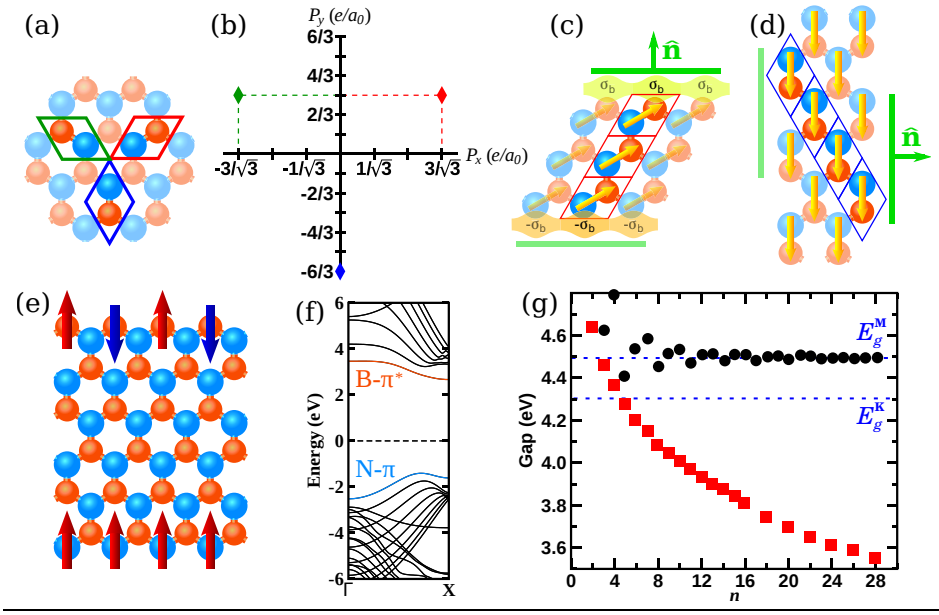

Figure 5.3: (a) h-BN lattice with three equivalent unit cells. Blue atoms represent N, while orange atoms represent B. (b) Polarizations corresponding to different choices of unit cells. The colour of each diamonds representing the polarization vectors corresponds with the colour of the unit cells in (a). (c) and (d), schematic showing zigzag and armchair edges, respectively, with the yellow arrows denoting the bulk polarization. The green lines are parallel to the edges in each case, and the vector $\hat{\mathbf{n}}$ is normal to the edge. In (c), σ_b represents the bound charge at the edges. (e) Magnetic ground state of ZBNNR with bare edges. Red arrows denote α-spin localized edge states, while blue arrows denote the same for β-spin. (f) Band structure of a ZBNNR with $n = 8$. (g) Electronic gap of BNNR. Black circles correspond to ABNNR, and red squares to ZBNNR. Dashed blue lines denote the gap at the **K** point ($E_g^{\mathbf{K}}$) and at the **M** point ($E_g^{\mathbf{M}}$) for pristine h-BN. Data taken from Ref. [204].

ribbons.[203 205] As shown in Figure 5.3(f), the highest valence band of ZBNNR is composed of π-orbitals from edge N atoms, and the lowest conduction band comes from π^*-orbitals of edge B atoms. According to DFT calculations, the gap can become even smaller to the one in h-BN sheets (denoted as $E_g^{\mathbf{K}}$ in Figure 5.3(g)). To compensate the bound charges present at the edges of ZBNNR a charge transfer from the N edge to the B edge lowers the conduction band (localised at the B edge) and raises the valence band (localised at the N edge) decreasing the gap. The potential generated by the bound charges at the edges can be modelled as an exponential function that decays far from the edges.[205] In the case of ABNNR, for wide ribbons, the gap approaches $E_g^{\mathbf{M}}$, the gap of a h-BN layer at the **M** point,[203,204] which corresponds to the direction of periodicity of armchair edges.

With these different characteristics for graphene and BN NRs, heterostructures made from both materials can present varied interfacial effects. Planar hybrid systems share many properties with NT made of B-C-N, that were theoretically studied in the 1990's.[77,206 208] In NT with highly homogeneous BC_2N mixing, the electronic properties depend not only

on the amount of C and BN, but in the structural atomic arrangement, with the most stable structures being semiconductors.[77,207] In phase separated NT, the gap is mainly determined by the amount of C, since states around E_F are mostly localized in the C part, and to a lesser but not negligible extent, in the first rings of the BN part.[208] More recently, the electronic and magnetic properties of these hybrids have been studied in more detail, finding that these systems can be semimetallic,[87,88] half-metallic[89], and present magnetic states at the interfaces.[86]

Very similar behaviour is found when joining GNR and BNNR to form hybrid 1D ribbons. The orbitals of C atoms at the interface mix with either B or N, forming hybridized β and β^* bands,[209] changing the character of valence and conduction bands near E_F. In armchair junctions, the band gap changes with respect to AGNR, resulting in larger gaps for the $n = 3p + 2$ family (which has the smallest gaps in AGNR) due to the interfacial charge reconstruction, which changes the potential near edge atoms.[210] For zigzag hybrid NR, the effect of the interface can lead to semiconductor, half-metallic and metallic band structures.[211,212] This same features are present in 2D systems of periodically repeated strips of graphene and BN, where half-semimetallicity and gap opening have also been found.[90–92,94]

In zigzag interfaces, the gap of the hybrid system will depend on the widths of both, graphene and BN, becoming smaller for wider ribbons (with a more important contribution of graphene to the closing of the gap, since its gaps decay to zero more quickly than in ZBNNR). Being ZBNNR polar, and ZGNR non-polar, there is a polar discontinuity at the interface, which gives an excess interfacial bound charge that can be calculated by the interface theorem, formulated by Vanderbilt and King-Smith,[119,213] which states that

$$(\mathbf{P}_1 - \mathbf{P}_2) \cdot \mathbf{n} = \sigma_b \tag{5.1}$$

As graphene has inversion symmetry, the bulk polarization is taken as zero. Thus, the bound charge at the interface is $\sigma_{int} = \pm e\ a_0$, being positive at the C-B interface, and negative at the C-N edge. This form of determining the interface charge of coplanar hybrids of polar compounds with hexagonal lattice has been used previously, showing that at the zigzag edges, there forms a one-dimensional electron/hole gas.[214] Mobile electrons from ZGNR will tend to screen this excess charge at the interface, by transferring electrons from one edge to the other, changing the potential profile across the ribbon, which produce and effective electric field capable of induce half-metallicity when it is strong enough to produce a Zener-like breakdown. For wider ZGNR, the gap is so small for both spins that it is very easy to close it in the hybrid systems, becoming metallic.[91]

5.3 Model Hamiltonian

The DFT description of hybrid graphene/BN systems provides an accurate picture of the physics inside the metal/semiconductor junction obtained. The counterpart is the required computational cost which limits the size of systems that can be studied to a few hundred atoms. This is an issue when attempting to simulate the systems observed experimentally, where large samples are grown, and the effects of disorder, grain boundaries and random distribution of features like electron puddles or interfaces are important. For these large systems, simpler models are useful. The TB model is capable of such simple representation preserving the fundamental behaviour of the heterostructures by including the appropriate parametrization.

The electronic properties of graphene are described correctly with very simple TB models, reproducing faithfully many properties like the linear dispersion at the **K** point.[5,8,215,216] Graphene has four valence electrons, three of which form tight σ-bonds which lie far below the Fermi level. The fourth electron forms the β-bonds that mostly determine the electronic behaviour of the system.[8] A simple model with one β (bonding) and one β^* (anti-bonding) bands per unit cell gives a good representation for graphene. The elements of the model Hamiltonian matrix take this form:

$$H_{\alpha\beta} = \ _{\alpha 0}\delta_{\alpha\beta} + \sum_{\mathbf{R}} \gamma_{\alpha\beta}^{(\mathbf{r}_{\alpha\beta})} e^{i\mathbf{k}\cdot\mathbf{r}_{\alpha\beta}} \tag{5.2}$$

where the first term stands for the on-site energy of orbital α, and the second term represents the electron hopping between orbital α at position $\mathbf{r}_\alpha$, and orbital β at position $\mathbf{r}_\beta + \mathbf{T}$, being $\mathbf{r}_{\alpha\beta} = \mathbf{r}_\alpha - (\mathbf{r}_\beta + \mathbf{T})$ the distance between both orbitals, and $\mathbf{T}$ a lattice vector. This same model can be used for h-BN by using two different on-site energies $_{\alpha 0}$ for the sublattice A and B sites.[217] Many systems have been studied using this simple TB, bilayer graphene[218–220], h-BN bilayers[221] and graphene on top of h-BN.[130,222]

The parameter $\gamma_{\alpha\beta}$ in Equation 5.2 is the hopping integral which reflects the interactions between different atomic orbitals. An accurate description for both, graphene and h-BN, can be obtained by including up to third-nearest-neighbour interactions, thus, the parameter $\gamma_{\alpha\beta}^{(\mathbf{r}_{\alpha\beta})}$ can take the values $\gamma_{\alpha\beta}^{(0)}$, $\gamma_{\alpha\beta}^{(1)}$ and $\gamma_{\alpha\beta}^{(2)}$, which represent first-, second- and third-nearest neighbour hoppings, respectively, and all other interactions are neglected. The different hoppings are shown schematically in Figure 5.4. If only low energy electronic levels are required (close to E_F), then longer range interactions can be ignored working only up to first or second nearest neighbours.

Due to the simplified nature of the TB model, the physics is not always well represented. For instance, the band structure of GNR is not in agreement with DFT calculations due to the erroneous modelling of edge states, and it is not possible to obtain the gap opening in ZGNR unless a Hubbard term is added to the Hamiltonian.[223–225] The Hubbard model considers on-site repulsion of electrons with different spin at doubly occupied orbitals, and can be included in the Hamiltonian as $H^U = U \quad {}_i n_i \; n_i$,[226] where U is the interaction energy, $n_{i\sigma}$ is the number operator and the sum is over all the orbitals.

For AGNR, as can be seen in Figure 5.2(a), the TB gap does not follow the DFT trend for none of the three families, and notoriously, the family $n = 3p + 2$ is always semimetallic.[187,195,227–229] To better represent edge states, explicit changes in the hopping integral between β-orbitals for edge atoms should be considered.[187,230] In armchair hybrids of GNR and BNNR, a exponentially decaying potential has been used to describe the effect of charge redistribution in C atoms close to the interface.[210]

In this work, to model the effect of polarization produced by edge effects in BNNRs, the on-site term is modified to include an electrostatic potential. In this way, the new position-dependent on-site energy becomes

$$ {}_\alpha(\mathbf{r}) = \quad {}_{\alpha 0} - e\Phi(\mathbf{r}) \tag{5.3}$$

where Φ is an effective potential,[231] which is considered to be a decaying function that vanishes in the centre of the ribbon, as explained later in section 5.6.

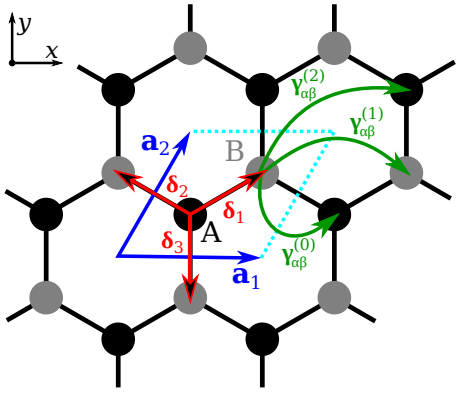

Figure 5.4: Hexagonal lattice showing the lattice vectors $\mathbf{a}_1$ and $\mathbf{a}_2$ (blue), vectors to nearest neighbour $\boldsymbol{\delta}_j$ (red) and the hoppings $\gamma_{\alpha\beta}$ (green) for first-, second- and third nearest neighbours.

As shown in Figure 5.4, the honeycomb lattice is taken to be formed by unit cell vectors $\mathbf{a}_1 = a_0(1 \;\; 0)$ and $\mathbf{a}_2 = a_0\left(\frac{1}{2} \;\; \frac{\overline{3}}{2}\right)$, and atoms within the unit cell at positions $\mathbf{r}_\mathrm{A} = \frac{1}{3}\mathbf{a}_1 + \frac{1}{3}\mathbf{a}_2$ for atoms in the A sublattice, and $\mathbf{r}_\mathrm{B} = \frac{2}{3}\mathbf{a}_1 + \frac{2}{3}\mathbf{a}_2$ for those in the B sublattice. The values of $\mathbf{r}_{\alpha\beta}$ for the three first-nearest neighbours are $s_i\boldsymbol{\delta}_j$, with $i = \mathrm{A}\;\mathrm{B}$; $s_\mathrm{A} = 1$, $s_\mathrm{B} = -1$ and $j = 1\;2\;3$; $\boldsymbol{\delta}_1 = a_0\left(\frac{1}{2} \;\; \frac{1}{2\;\overline{3}}\right)$, $\boldsymbol{\delta}_2 = a_0\left(-\frac{1}{2} \;\; \frac{1}{2\;\overline{3}}\right)$ and $\boldsymbol{\delta}_3 = a_0\left(0 \;\; -\frac{1}{\overline{3}}\right)$. For the six second-nearest neighbours, $\mathbf{r}_{\alpha\beta I}$ is $\pm a_0\,(1 \;\; 0)$, $\pm a_0\left(\frac{1}{2} \;\; \frac{\overline{3}}{2}\right)$ and $\pm a_0\left(\frac{1}{2} \;\; -\frac{\overline{3}}{2}\right)$; and for the three third-nearest neighbours, $a_0\left(\frac{s_i+1}{2} \;\; \frac{s_i-3}{2\;\overline{3}}\right)$, $a_0\left(\frac{s_i-1}{2} \;\; \frac{s_i+3}{2\;\overline{3}}\right)$ and $a_0\left(\frac{s_i-3}{2} \;\; \frac{s_i-3}{2\;\overline{3}}\right)$.

5.4 Hamiltonian in WF basis

The parameters for the TB are computed from the Hamiltonian expressed in the basis of Wannier functions (WF) basis, which are obtained from wannierisation of the Bloch states calculated from first principles. The DFT calculations are done using norm-conserving Troullier-Martins pseudopotentials,[159] and the PBE generalized gradient approximation[232] as implemented in the SIESTA code.[122] The wavefunctions for the valence electrons are described using a linear combination of pseudo-atomic numerical orbitals with a double-ζ polarized basis (DZP).[123] A Monkhorst-Pack k-sampling[161] of 48×48 is used for the pristine systems. A vacuum space of ∼40 Å between layers is taken to prevent interactions between them under periodic boundary conditions. The atomic positions are relaxed until the forces are smaller than 0.01 eV/Å. Once the density matrix is converged the expansion coefficients of the Bloch wave functions obtained from the SIESTA Kohn-Sham Hamiltonian, $c_{\mu n}$, (see subsection 2.2.3) can be used to obtain the unitary matrix $U_{mn}(\mathbf{k})$ necessary for the construction of WF (see Appendix A). This is done via $M_{mn} = \langle u_{m\mathbf{k}} | u_{n\,\mathbf{k}+\mathbf{b}} \rangle$ and $A_{mn} = \langle u_{m\mathbf{k}} | g_n \rangle$, the overlap matrices between the periodic part of the electronic wavefunctions, and the trial orbitals g_n, respectively, as described in Ref. [233]:

$$M_{mn}(\mathbf{k}, \mathbf{b}) = \sum_{\mu\nu} \sum_{\mathbf{T}} c^*_{\mu m}(\mathbf{k}) c_{\nu n}(\mathbf{k}+\mathbf{b}) e^{i\mathbf{k}\cdot(\mathbf{T}-\mathbf{r}_\mu+\mathbf{r}_\nu)} \mathcal{M}_{\mu\nu}(\mathbf{T}, \mathbf{b}) \tag{5.4}$$

and

$$A_{mn}(\mathbf{k}) = \sum_{\mu} c^*_{\mu m}(\mathbf{k}) \sum_{\mathbf{T}} e^{-i\mathbf{k}\cdot(\mathbf{T}+\mathbf{r}_\mu)} \mathcal{A}_{\mu n}(\mathbf{T}) \tag{5.5}$$

where

$$\mathcal{M}_{\mu\nu}(\mathbf{T}, \mathbf{b}) = \int \phi^*_\mu(\mathbf{r}+\mathbf{T}-\mathbf{r}_\mu+\mathbf{r}_\nu) e^{-i\mathbf{b}\cdot\mathbf{r}} \phi_\nu(\mathbf{r}) d^3\mathbf{r} \tag{5.6}$$

and

$$\mathcal{A}_{\mu n}(\mathbf{T}) = \int \phi^*_\mu(\mathbf{r}-\mathbf{T}-\mathbf{r}_\mu) g_n(\mathbf{r}) d^3\mathbf{r} \tag{5.7}$$

For both, graphene and BN, a good choice for the trial functions $g_n(\mathbf{r})$ is to represent the electronic orbitals as sp^2 and p_z. Then, for each unit cell with two atoms, there are three sp^2 and two p_z orbitals. This gives a total of five basis functions, of which four are occupied states and one is an empty state, enough to achieve a good description of the valence bands and the first conduction band. Since the first conduction band crosses higher energy bands, a band disentanglement procedure is used[234] following the prescription implemented in the WANNIER90 code[235] for maximally localised WF (MLWF). The inner window is taken from the lowest σ-band up to E_F. The outer window is set to include the inner window plus the β^* conduction band. This is pictured in Figure 5.5(a).

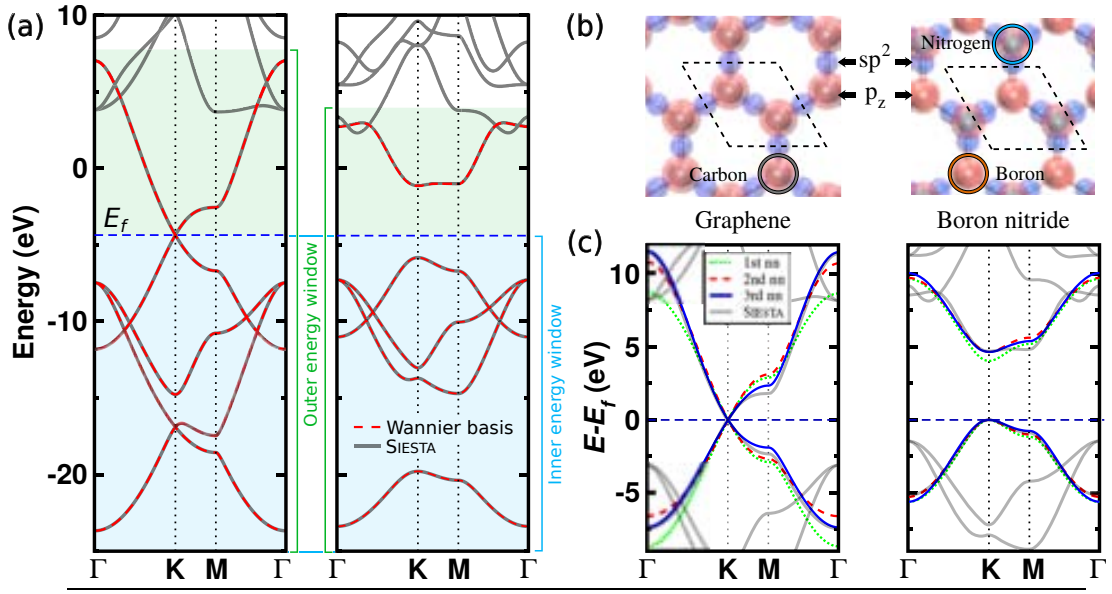

Figure 5.5: (a) Bands from SIESTA (grey) and with Wannier interpolation (dashed red) for graphene (left) and BN (right). The outer and inner windows considered for the Wannierisation are shown. (b) Graphene (left) and BN (right) structures showing the final positions of the Wannier centres as red spheres for p_z orbitals and blue spheres for sp^2 orbitals. (c) TB bands for graphene (left) and BN (right) using the parameters obtained from WANNIER90 and considering first- (dotted black), second- (dashed red) and third-nearest neighbours (solid blue). The bands from SIESTA are also shown (in grey) for comparison.

The unitary matrix $U_{mn}(\mathbf{k})$ is found by minimising the gauge dependent part of the spread functional using Equation A.5 and Equation A.6, which involve the use of the overlap matrix M_{mn}. For disentanglement, $U^{\text{dis}}_{mn}(\mathbf{k})$ is found by minimising the gauge invariant part of the spread functional. Having the unitary matrices, the Hamiltonian in the basis of MLWF is

$$\hat{H}^{\text{W}}(\mathbf{k}) = \left(\hat{U}(\mathbf{k})\right)^{\dagger} \left(\hat{U}^{\text{dis}}(\mathbf{k})\right)^{\dagger} \hat{H}(\mathbf{k})\hat{U}^{\text{dis}}(\mathbf{k})\hat{U}(\mathbf{k}) \tag{5.8}$$

where $H_{mn}(\mathbf{k}) = \varepsilon_{n\mathbf{k}}\delta_{mn}$, and $\varepsilon_{n\mathbf{k}}$ are the eigenenergies of the Kohn-Sham Hamiltonian from SIESTA. This Hamiltonian can be seen as a representation of the interactions between localised functions that, by construction of the trial orbitals, have great resemblance with the chemical σ- and π-bonds of graphene and BN. Consequently the relevant TB parameters can be straightforwardly extracted from this Hamiltonian.

5.5 Graphene and *h*-BN parameters

Let us first analyse the simplest systems, i.e. pristine graphene and *h*-BN. To start the minimisation, sp^2 trial orbitals are placed at the centres of the bonds between atoms, and p_z orbitals at the same position as atoms. In the case of π-orbitals, the final positions remain

at the centres of the atoms. For graphene, the MLWF with σ-bond character are localised midway between the two atoms comprising the unit cell, highlighting the covalent nature of the bonding. Differently, for BN the centres of this type of MLWF are located closer to N atoms, evidencing an ionic type of interaction, where B is the cation and N the anion. The final positions of the MLWF are sketched in Figure 5.5(b). The spread of the p_z orbitals in the final minimisation is 0.932 Å^2 for both C atoms in graphene, and 2.111 Å^2 for B atoms and 1.033 Å^2 for N in *h*-BN; for sp^2 orbitals, the spread is 0.615 Å^2 in graphene, and 0.593 Å^2 in BN.

The band structures obtained with Wannier interpolation in both systems, are in excellent agreement with those obtained with SIESTA, as can be seen in Figure 5.5(a). From the Wannierised bands, only the two bands closest to E_F, namely the β and β^* bands, are taken for the TB model.

Table 5.1: Tight binding parameters for graphene and BN, taken from the Hamiltonian in the basis of Wannier functions. Values in parenthesis are those obtained with QUANTUM ESPRESSO. All data in eV.

	C	B	N
$\varepsilon_{\alpha 0}$	0 39 (0 41)	4 32 (4 47)	0 28 (0 37)
$\gamma_{\alpha\beta 0}$	−2 89 (−2 72)	−2 46 (−2 63)	−2 46 (−2 63)
$\gamma_{\alpha\beta 1}$	0 23 (0 20)	−0 11 (0 01)	0 09 (0 19)
$\gamma_{\alpha\beta 2}$	−0 25 (−0 23)	−0 11 (−0 19)	−0 11 (−0 19)

The value of the on-site energy $\varepsilon_{\alpha 0}$ depends on the zero-energy reference. To have a common reference the values obtained from the wannierisation ($\varepsilon^{\mathrm{W}}_{\alpha}$) are shifted to $\varepsilon_{\alpha 0} = \varepsilon^{\mathrm{W}}_{\alpha} - E_F - E_0$, where the Fermi level E_F is taken as the highest energy of the valence band, and E_0 is the vacuum level. The TB parameters obtained from the Hamiltonian in MLWF basis are listed in Table 5.1. For comparison, values obtained with MLWF constructed from calculations using the QUANTUM ESPRESSO package[236] are also shown. The TB bands are compared to those obtained with SIESTA in Figure 5.5(c). The best description is attained with the inclusion of third-nearest neighbours interactions, and as can be seen, considering only first-nearest neighbours results in a less accurate description far from E_F. For both, graphene and BN, the bands near the **K** point are very accurate, while close to the **M** point, the dispersion differs noticeably from that of the DFT calculations. In order to improve the description at the **M** point, long-range interactions between β-orbitals should be considered, which mean taking into account neighbour orbitals as far apart as >5 Å, corresponding to sixth-nearest neighbours, which is not practical in a simplified TB model.

5.6 Hybrid systems parameters

Systems with zigzag and armchair edges

The first hybrid systems studied are constructed by joining graphene and BN nanoribbons so that heterojunctions with zigzag or armchair interfaces are obtained. A diagram of the systems is shown in Figure 5.6(a). Periodic boundary conditions are used, with the x parallel to the interfaces and z perpendicular to the layer. To describe edge states, a dense k-sampling along the interface is needed. Here, a 67×1 Monkhorst-Pack sampling is used for the hybrid systems. The number of C zigzag or armchair chains in the system is labelled n_{C}, while n_{BN} designates those for BN. For notation purposes, let $\mathrm{Z}_{n_{\mathrm{C}}\, n_{\mathrm{BN}}}$ and $\mathrm{A}_{n_{\mathrm{C}}\, n_{\mathrm{BN}}}$ be the systems with zigzag and armchair interfaces, respectively, composed of a ribbon of graphene with n_{C} rows, and a ribbon of BN of n_{BN} rows. Systems with compositions in the range of $5 \leq n_{\mathrm{C}} \leq 9$ and $5 \leq n_{\mathrm{BN}} \leq 12$ have been studied in the case of zigzag interfaces. For armchair systems, values of $9 \leq n_{\mathrm{C}} \leq 12$ and $12 \leq n_{\mathrm{BN}} \leq 15$ are used. In the case of zigzag ribbons, the supercell is defined by lattice vectors $\mathbf{a}_1^{\mathrm{Z}} = a_0(1\ \ 0)$ and $\mathbf{a}_2^{\mathrm{Z}} = a_0\left(0\ \ \frac{\bar{3}}{2}(n_{\mathrm{C}} + n_{\mathrm{BN}})\right)$. For the armchair case, $\mathbf{a}_1^{\mathrm{A}} = a_0\left(\ \ \bar{3}\ \ 0\right)$ and $\mathbf{a}_2^{\mathrm{A}} = a_0\left(0\ \ \frac{n_{\mathrm{C}}+n_{\mathrm{BN}}}{2}\right)$. The different values of the lattice parameter for pristine graphene and h-BN, give rise to strains between domains in the superlattices formed. After full relaxation, the cell parameter a_0 takes values between that of BN (2.52 Å) and graphene (2.47 Å), being larger for systems with larger size of the BN region, and smaller for those with more C. This tendency can be seen in Figure 5.6(b) for the case of zigzag hybrids, where the norm of the vector $\mathbf{a}_1^{\mathrm{Z}}$ is plotted as a function of the difference between the number of zigzag rows of C and BN. Furthermore, the relaxation induces an inhomogeneity in the lattice parameter breaking the C_3 symmetry, as the competition in strains between graphene and BN acts mainly in the x axis, having more freedom to expand or shrink in the y direction.

As can be seen in Figure 5.6(c), the interatomic distance between carbon atoms has one behaviour for the bonds oriented parallel to the y axis, and other for the bonds that have also a component in the x axis. Near the edges the distances are modified mainly to compensate the charge redistribution. In the middle, the C C distance along y are shorter, and hence more alike the C C distance in pristine graphene, due to the freedom above mentioned. In the BNNR, the distribution of B N bond distance parallel to y is asymmetric, with a noticeable decrease in distance near the N edge.

In Figure 5.7(a), the macroscopic average[113] of the electronic charge density ($\bar{\alpha}_e$) and the effective potential ($\bar{V}_{eff}$) are displayed for the armchair system $\mathrm{A}_{12\,12}$, and in Figure 5.7(b) for the zigzag system $\mathrm{Z}_{9\,9}$. The average electronic charge density far from the interface in

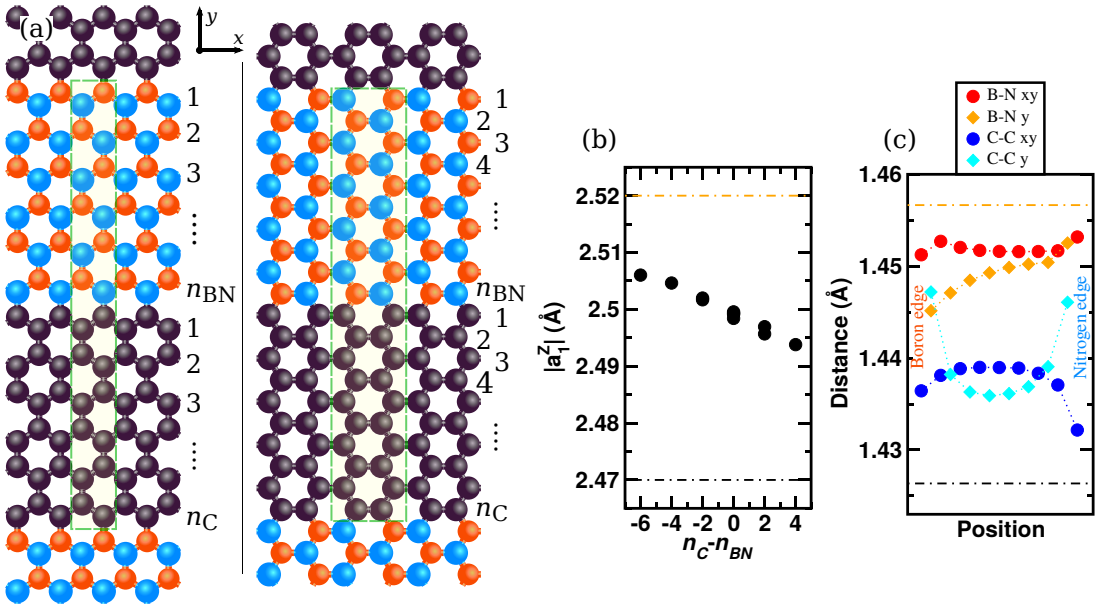

Figure 5.6: (a) Diagram of the hybrid systems consisting of nanoribbons of graphene and BN joined by the zigzag (left) and armchair (right) interface. The systems are defined by the number of rows of each material, denoted n_C for graphene and n_{BN} for BN. The unit cell is enclosed in the dashed green box. (b) Size of the cell in the x direction as a function of the difference between n_C and n_{BN}, considering all the zigzag systems studied. (c) Interatomic distances for the $Z_{9,9}$ system. Dash-dotted lines in (b) and (c) correspond to the lattice parameter and interatomic distance, respectively, in pristine graphene and h-BN.

both, zigzag and armchair systems is 0.430 electrons/Å^3 for graphene and 0.423 electrons/Å^3 for BN. Despite the fact that each region has the same number of electrons per unit cell, the difference in charge density is due to the different lattice parameters, being smaller in graphene, hence having a more dense packaging of the electrons. This was verified by counting the number of electrons in a single unit cell (two atoms) obtaining 8 electrons/unit cell all across the flat regions of the charge density. At the interface of armchair ribbons, there is a soft change in the charge density due to charge redistribution at the C–B and C–N bonds as seen in Figure 5.7(a). Following Equation 1.2, the band offset of graphene and h-BN can be obtained from the macroscopic profile of the potential for the armchair systems as

$$\Delta E_{\mathrm{VBO}} = \left(E_v^{(\mathrm{G})} - E_0^{(\mathrm{G})}\right) - \left(E_v^{(\mathrm{BN})} - E_0^{(\mathrm{BN})}\right) + \Delta\tilde{V}, \tag{5.9}$$

resulting in a band offset of 1.28 eV, while the difference in the potential $\Delta\tilde{V}$ is 0.12 eV.

In the zigzag case, abrupt changes in the charge density can be observed at the interface (Figure 5.7(b)). The accumulation of electrons in the C-N side and a depletion in the C-B interface comes from the bound charges of the polarization discontinuity. To counteract the effect of BN polarization, free carriers from graphene must screen out the bound charges by moving electrons from the C–N side to the C–B side. The result is a lack of electrons

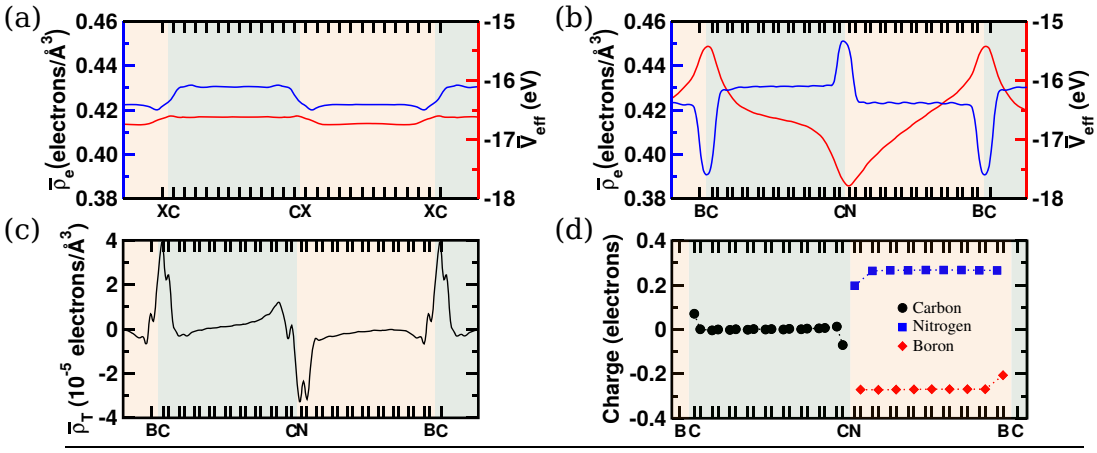

Figure 5.7: (a) Macroscopic average of the electronic charge density (blue) and effective potential (red) across the y direction for the system $A_{12,12}$ (b) The same as in (a) for the system $Z_{9,9}$. (c) Macroscopic average of the total charge for $Z_{9,9}$. (d) Hirshfeld atomic charges for $Z_{9,9}$. The ticks at the bottom mark the positions of atoms within the cell.

in the net charge at the C–N interface and an excess of electron in the net charge at the C–B interface as can be seen in Figure 5.7(c). This same behaviour is shown by a Hirshfeld population analysis [237] of the atomic charges, as seen in Figure 5.7(d). The C atoms at the interfaces have a charge of $\pm 0.07|e|$. Interfacial N has a charge of $-0.20|e|$, which is $0.07|e|$ higher than the Hirshfeld charge in pristine h-BN ($-0.27|e|$). In the other hand, interfacial B has a charge of $0.21|e|$, with a difference with respect to pristine h-BN of $-0.06|e|$, which means there is a difference of $0.01|e|$ between B and N interfacial charges. Comparing the charges of all C atoms with those of B and N, there is a charge transfer of $0.03|e|$ from BN to graphene, part of which should come from the lack of electrons at the B edge. The localized charges at the interface cause a change in the potential as seen in Figure 5.7(b), and is essential to model the electronic properties of hybrid systems with zigzag interface. The potential has a maximum at the C–B interface, with less charge, and a minimum at the C–N interface, with more charge.

The effect of interfacial reconstruction is more remarkable in zigzag systems, so special care must be taken to consider the physics that rule their properties. The charges at the 1D interfaces can be simplistically seen as two lines of charge, placed at $\pm L/2$ and having a linear charge density $\pm Q_\lambda$. This is schematized in Figure 5.8(a). The problem of a line of charge is a well known problem in electrostatics, [238] that in this case with two opposite charged lines results in the potential:

$$\Phi(x) = \frac{Q_\lambda}{2\pi\epsilon_0} \ln\left(\frac{L+2x}{L-2x}\right), \tag{5.10}$$

where ϵ_0 is the vacuum permittivity. This potential is plotted in Figure 5.8(a), and has

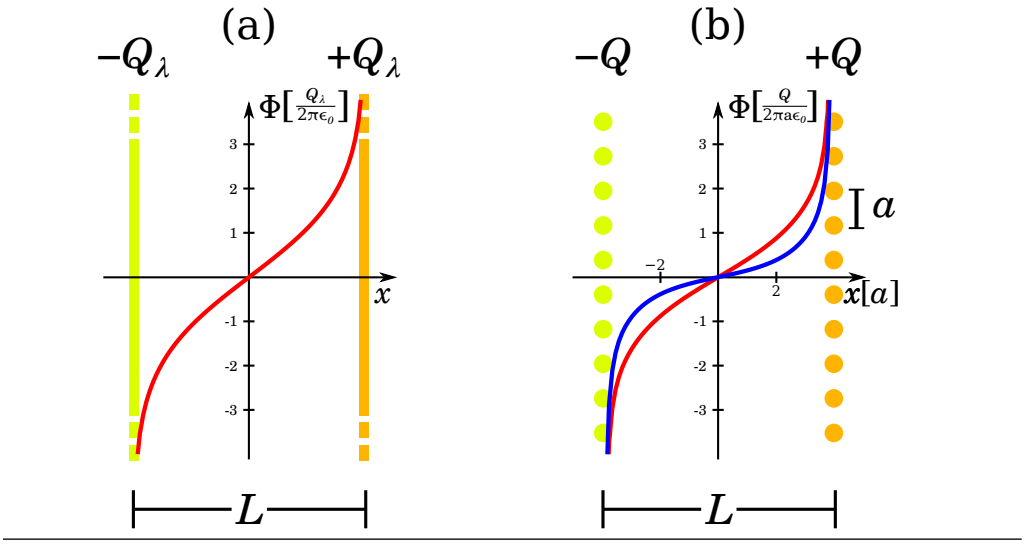

Figure 5.8: (a) Parallel charged lines with opposite charges ($\pm Q_\lambda$) situated at $\pm L$ 2. (b) Discretized problem with point charges $\pm Q$ situated at $\pm L$ 2. At each side, the charges are equally spaced a distance a. The value $L = 8a$ is considered. Two different damping factors (γ) of the screened potential are used, $\gamma = 7a$ (red) and $\gamma = 2a$ (blue).

similar shape to the one shown in Figure 5.7(a). The differences in the functional shape come from the fact that the potential from the DFT calculation corresponds to a periodically repeated array of linear charges, which have some spatial spread (more similar to a cylindrical charge distribution) and acts over different materials, each one with its own permittivity, which leads to a different screening due to valence electrons in each region. For the model to be computationally efficient, instead of considering an infinite line, it is better to discretize the problem considering an infinite array of point charges along the interfacial axis, as shown in Figure 5.8(b). The position of the point charges is taken to be midway the C B and C N interfacial bonds.

Due to the semi-metallicity of graphene, the electric field in this region will be damped by the redistribution of valence electrons. The screened Poisson equation describes systems with this kind of screened Coulomb interactions, and here is considered to model the interfacial potential. The screened potential for an arrange of point charges has the form

$$\Phi(r) = \sum_i \frac{Q_i}{4\beta\epsilon_0 r_i} e^{-\frac{r_i}{\lambda}} \tag{5.11}$$

where Q_i are the charges, r_i is the distance between r and the charge Q_i, and γ is a damping factor related to the mobility of electrons in the material. The functional form of this type of potential is plotted in Figure 5.8(b). The case in Figure 5.8(a) corresponds to Equation 5.11 in the case of γ and [taking the sum/summing] over an infinite number of point charges (assuming $L \geq a$). The potential profile of the graphene part in Figure 5.7(a), looks more

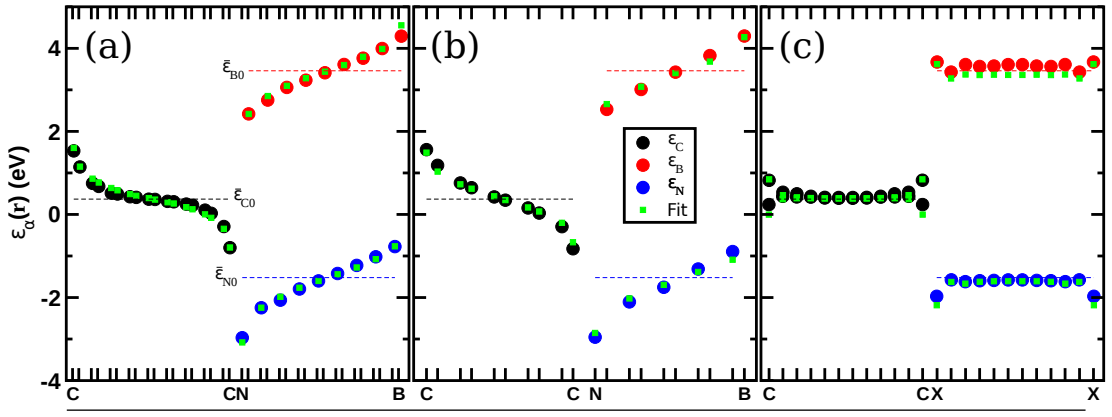

Figure 5.9: On-site energy values as a function of the atomic positions for the systems (a) $Z_{9\,9}$, (b) $Z_{5\,5}$ and (c) $A_{12\,12}$. Black circles correspond to C atoms, red circles to B and blue circles to N. Green squares are the on-site terms $_\alpha(\mathbf{r})$ with the functional form in Equation 5.12 and the parameters from Table 5.2. The values $^-_{\alpha 0}$ for the different species are shown in dashed lines.

like the screened potential with short γ, since the availability of electrons to screen the potential is large. The effect of the potential can be included in the on-site term of the TB Hamiltonian as in Equation 5.3, considering the sum of two screened-like potentials with opposite signs, corresponding to both interfaces:

$$_\alpha(\mathbf{r}) = {}^-_{\alpha 0} + \sum_i^{n_q} \frac{A_\alpha^{\mathrm{B}}}{\mathbf{r}-\mathbf{r}_i^{\mathrm{B}}} e^{-\frac{|\mathbf{r}-\mathbf{r}_i^{\mathrm{B}}|}{\lambda_\alpha}} - \sum_i^{n_q} \frac{A_\alpha^{\mathrm{N}}}{\mathbf{r}-\mathbf{r}_i^{\mathrm{N}}} e^{-\frac{|\mathbf{r}-\mathbf{r}_i^{\mathrm{N}}|}{\lambda_\alpha}} \tag{5.12}$$

which represent the diagonal term for an atom of species α at position $\mathbf{r}$, with $^-_{\alpha 0}$ being the on-site energy in absence of the potential; A_α^{B} and A_α^{N} the amplitudes of the potential for that species in the B and N interfaces, respectively; $\mathbf{r}_i^{\mathrm{B}}$ and $\mathbf{r}_i^{\mathrm{N}}$ the positions of the charges at the C B and C N interfaces, respectively; γ_α the damping factor; and the sum is done for all n_q charges, in the unit cell and in all periodically repeated neighbour cells within the cutoff radius r_{cut}. The parameter r_{cut} is taken so that changes in the on-site term due to point charges far away are less than 0.02 eV, which gives $r_{\mathrm{cut}} \sim$10 Å. The amplitudes of the potential for B and N are taken to be equal ($A_{\mathrm{B}}^{\mathrm{B}} = A_{\mathrm{N}}^{\mathrm{B}}$ and $A_{\mathrm{B}}^{\mathrm{N}} = A_{\mathrm{N}}^{\mathrm{N}}$) as well as their damping lengths ($\gamma_{\mathrm{B}} = \gamma_{\mathrm{N}}$).

Table 5.2: Parameters obtained from the fit to the on-site energies of the zigzag systems.

	C	B	N
$^-_{\alpha 0}$ (eV)	1 13	4 22	−0 76
A_α^{B} (eV·Å)	0 61	0 46	0 46
A_α^{N} (eV·Å)	0 54	0 62	0 62
γ_α (Å)	6 78	12 56	12 56

The parameters A_α^{B}, A_α^{N}, γ_α and $^-_{\alpha 0}$ are fitted to the data from the diagonal of the Wannier Hamiltonian using the simplex algorithm.[239] As shown in Figure 5.9, the on-site energies

from H^W are in good agreement with the form of the potential in Equation 5.12, and the fitted values reproduce well these on-site energies. The obtained parameters for the on-site potential are shown in Table 5.2. Although the on-site energies are fitted from zigzag systems, it gives a good description for edges with any chirality.

Table 5.3: Summary of the parameters considered in the non-spin polarized TB model.

Parameter	Units	Value	
$\bar{}_{\mathrm{C0}}$	eV	0 00	On-site
$\bar{}_{\mathrm{B0}}$	eV	3 09	
$\bar{}_{\mathrm{N0}}$	eV	−1 89	
A_{P}	eV·Å	0 56	
γ_{C}	Å	6 78	
γ_{BN}	Å	12 56	
m_{C}	eV/Å	3 72	1st nn.
m_{BN}	eV/Å	3 11	
b_{C}	eV	−12 14	
b_{BN}	eV	−10 68	
$\gamma^{(0)}_{\mathrm{CB}}$	eV	−2 68	
$\gamma^{(0)}_{\mathrm{CN}}$	eV	−2 79	
$\gamma^{(1)}_{\mathrm{CC}}$	eV	0 23	2nd nn.
$\gamma^{(1)}_{\mathrm{BB}}$	eV	0 14	
$\gamma^{(1)}_{\mathrm{NN}}$	eV	0 18	
$\gamma^{(1)}_{\mathrm{CB}}$	eV	0 19	
$\gamma^{(1)}_{\mathrm{CN}}$	eV	0 19	
$\gamma^{(2)}_{\mathrm{CC}}$	eV	−0 24	3rd nn.
$\gamma^{(2)}_{\mathrm{BN}}$	eV	−0 15	
$\gamma^{(2)}_{\mathrm{CB}}$	eV	−0 16	
$\gamma^{(2)}_{\mathrm{CN}}$	eV	−0 18	

For systems with armchair edges, the charge rearrangement at the interface changes the potential locally, as can be observed in Figure 5.7(b), where the potential remains flat in the central part of both, AGNR and ABNNR, but presents small fluctuations near the edges. This is reflected in the values of the on-site terms in the Wannier Hamiltonian which are almost constant except near the interface. As seen in Figure 5.9(c), the on-site terms for armchair hybrids can also be well represented with the potential model of Equation 5.12, which is a generalization for all interfaces between graphene and h-BN.

The value of the reference energy in the on-site energies for the TB model is completely arbitrary, and for easiness, a shift is applied to the on-site values so $\bar{}_{\mathrm{C0}} = 0$ eV. As a final consideration for the potential and to simplify the model, the amplitudes A^{X}_{α} are taken as a single value obtained from the average of those presented in Table 5.2 and denoted in the following as A_{P}. The final values for the on-site energies and the parameters of the potential are listed in Table 5.3.

The values of the nearest neighbour hoppings vary from system to system and inside each system changes for each pair of atoms. In the graphene region, $\gamma^{(0)}_{\mathrm{CC}}$ has values from −3 04 to −2 81 eV for all the considered systems, while $\gamma^{(0)}_{\mathrm{BN}}$ is in the range −2 96 to −2 79 eV. In Figure 5.10(a), the hopping energies for nearest neighbours are plotted as they change along the ribbons for the system $\mathrm{Z}_{9\,9}$. The dependence of $\gamma^{(0)}_{\alpha\beta}$ with the position resembles that in Figure 5.6(c) for the interatomic distances. Since the hopping parameter

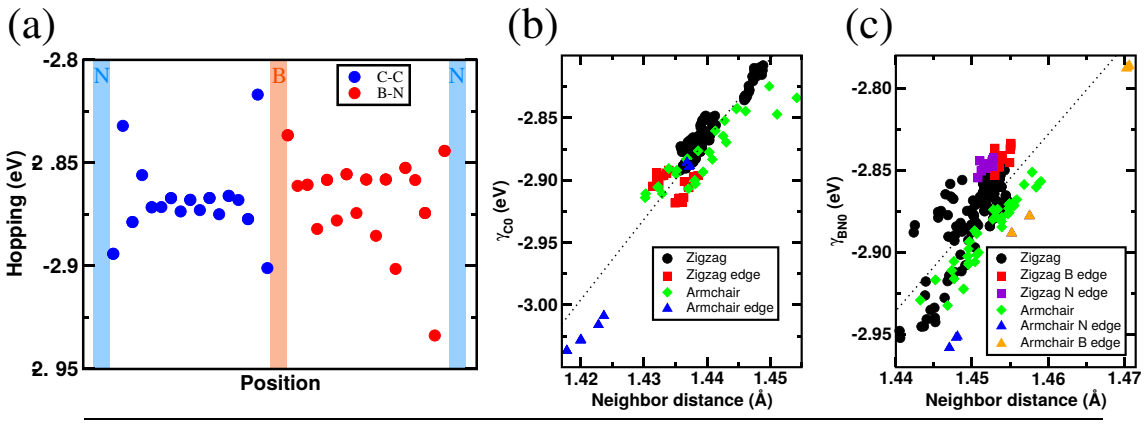

Figure 5.10: (a) Hopping energies as a function of the position along the y axis for the system $Z_{9,9}$. (b) Hopping energies as a function of the interatomic distance between neighbour atoms for C, considering all zigzag and armchair systems. (c) The same as in (b) for B–N neighbours. The dotted lines are best linear fits for all the hoppings.

depends on the distance between atoms and the specificities of each orbital, small variations are present in all the systems due to the anisotropies of the cell and atomic relaxation, and the chemical environment of each atom within the ribbon. In Figure 5.10(b) and Figure 5.10(c), the values of the hopping parameter between C-C and B-N are plotted as a function of the atomic distance. It is observed a general tendency where $|\gamma^{(0)}_{\alpha\beta}|$ decreases as the interatomic distance increases. Although a precise description of the hopping is only possible by considering the specific characteristics of the orbitals of each atom, considering the hopping to depend linearly with the distance is enough to get a practical approximation. The linear fit is done considering the expression

$$\gamma^{(0)}_{\alpha\beta} = m_\alpha a_0 + b_\alpha, \tag{5.13}$$

which only applies for C–C and B–N hoppings, and $m_B = m_N = m_{BN}$ and $b_B = b_N = b_{BN}$. Considering the different hoppings among all atoms in the structure to depend on their distances requires a structural relaxation, which is impractical. Thereby, the hopping is taken as a single value (for each type of species) that depends only on the chosen lattice parameter a_0, which varies according to the amount of C and BN in the system, as in Figure 5.13(b). Below, it will be shown that the band structure of hybrid systems are not affected importantly by the details of the hopping parameter. The values for the other hoppings (C–B, C–N) are taken as the average among all the systems considered and are shown in Table 5.3.

The model is tested for the $A_{11,13}$, $Z_{5,5}$ and $Z_{9,9}$ systems. The band structure of the system $A_{11,13}$ is shown in Figure 5.11(a). It can be observed that the valence and conduction bands are in better agreement with DFT close to E_F than they are for higher energies. The

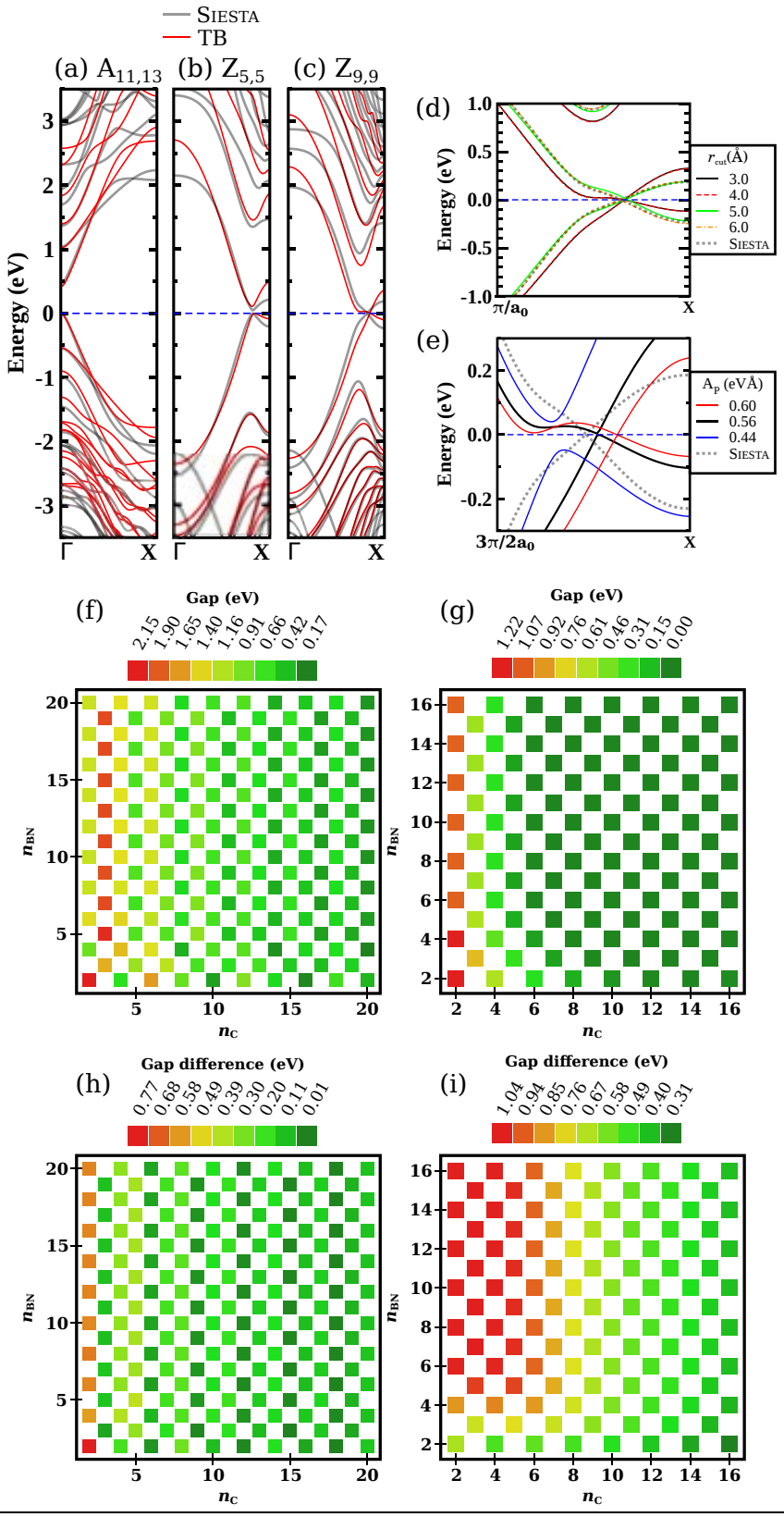

Figure 5.11: Comparison of DFT and TB bands for the (a) $A_{12,12}$, (b) $Z_{5,5}$ and (c) $Z_{9,9}$ systems. The bands from SIESTA are shown in grey, and those of TB in red. (d) Bands of $Z_{9,9}$ using the Hamiltonian of WANNIER90 with a cut-off of 3, 4, 5 and 6 Å. (e) Bands of $Z_{9,9}$ using different values of A_P.

differences between the SIESTA bands and TB bands are larger for the unoccupied bands, which are more dispersive with TB, while the TB occupied bands, although being more localized than in DFT, are in better agreement than the unoccupied bands. The gap with TB is 0.41 eV in good agreement with the 0.46 eV gap given by SIESTA. If the interface potential is not taken into account, i.e. $A_P = 0$, the gap would be 0.61 eV, showing that the potential has an important effect over the gap. In Figure 5.11(f), the energy gaps for different armchair systems are shown. It can be observed that the gap tends to be smaller as n_C increases. The smallest gaps are obtained for systems that satisfy $n_C = 3p+2$, as in isolated AGNR.[187] To examine the influence of the interface potential, the difference of the TB gap with $A_P = 56$ eV and $A_P = 0$ eV is obtained for different armchair systems, as shown in Figure 5.11(h). For $n_C = 2$, the gap difference is maximum, and decreases as n_C becomes larger. For systems with $n_C = 3p$, the interface potential has little effect in the value of the gap.

The band structure of the system $Z_{5\,5}$ is shown in Figure 5.11(b). This system is semiconductor with a small DFT band gap of 0.05 eV. Using TB with $A_P = 0$ 56 eV, the gap is 0.11 eV which is an improvement over the gap of 1.09 eV using $A_P = 0$ eV. As in the armchair case, the TB occupied bands are in better agreement with DFT than the unoccupied ones. The different TB gaps for zigzag systems are shown in Figure 5.11(g). The gap decreases as both, n_C and n_{BN} increases, with a faster decay for n_C. A comparison between the gap with and without the interfacial potential is shown in Figure 5.11(i) as the difference of both cases. The gap difference is smaller as n_C increases, but has the opposite tendency for n_{BN}. With larger values of n_{BN} the polarity increases, and the effect of the interface potential is more important. For larger values of n_C, the gap without the potential term decreases approaching to zero and the error in the gap decreases.

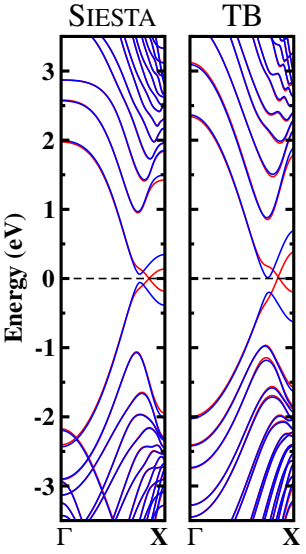

Figure 5.12: Band structure of $Z_{9\,9}$ considering spin polarization. The bands correspond to calculations made with SIESTA (left) and TB (right). Red and blue bands represent α and β spin components, respectively.

For the system $Z_{9\,9}$, the gap of graphene is small enough and the polarization from BN strong enough to close the gap becoming semimetal, as can be observed in the band structure of Figure 5.11(c). The bands close to E_F are found to be very sensitive to long range interactions. The effect of considering hoppings to atoms farther than third nearest neighbours is investigated. For this, the Wannier Hamiltonian is truncated to include only the elements whose WF are within a certain cut-off radius r_{cut}. The bands near E_F of the

system $Z_{9\,9}$ considering different r_{cut} are shown in Figure 5.11(d). For $r_{cut} \leq 4$ Å, which corresponds to taking into account up to 4th nearest neighbours, the bands are very similar to what is obtained with the TB model including the interface potential and third nearest neighbours interactions. Note that in the Wannier Hamiltonian, the different hoppings, which depend on geometric details, are explicitly taken into account, and in the TB model they are not, making no significant difference and validating our assumption of taking the hopping as a single value for the different species. For $r_{cut} = 5$ Å the bands are already in very good agreement with those of SIESTA, but that requires considering up to 6th nearest neighbours interactions.

Table 5.4: Parameters used in the spin polarized calculation.

Parameter	Value
U_{C} (eV)	5 20
U_{BN} (eV)	4 50
A^{N} (eV·Å)	0 75
A^{B} (eV·Å)	0 45
γ_{C} (Å)	5 50
γ_{BN} (Å)	12 56

The specifications of the potential at the interface are also important for the description of the bands close to the Fermi level. In Figure 5.11(e), the band structures of the system $Z_{9\,9}$ using different values of A_{P} are shown. The values considered are around $A_{\mathrm{P}} = 0\ 56$ eV·Å, the one obtained from the fit. If the strength of potential is increased, the bands near E_{F} become more localised being more noticeable for the highest valence band. The most important contributions to this band are from C and B orbitals of the interface where mobile electrons attempt to screen the bound charge from BN.[91] If the potential is increased, more electrons are going to participate in the screening and the localization at the C-B edge will increase. On the other hand, if the potential is decreased, the system becomes semiconductor as the induced electric field will not be strong enough to close the gap. The gap keeps opening up to the point where the potential is zero and the gap is that of the ZGNR. From this, it is clear that the electronic properties of these hybrid layers can be changed by varying the interface potential. One way to do this is by applying strain taking advantage of the piezoelectric properties of BN. Thus, zigzag systems that are initially semiconductor can become semimetallic as an effect of straining the lattice along the y axis. The subject of piezoelectricity in hybrid systems will be treated in chapter 6.

The effect of spin polarization is important in these systems, as previously discussed, and for the system $Z_{9\,9}$ it is primordial, since in its ground state the system is half-metallic, as can be observed in the band structure of Figure 5.12. In the TB model, the Hubbard term should be added to consider the on-site repulsion of electrons with different spin. By doing this, slightly different parameters must be considered to get a better fit to the spin-polarized band structure. Electron-electron interactions are localized features that take place mainly at the edge and would only affect the parameters of the screened potential. The values listed in Table 5.4 are found to give good results. Note that the amplitudes of the potential, A^{N}

and A^{B}, should be different, and taking an average (as done in the non-spin-polarized case) leads to wrong results. Since the bands for each spin are localized at opposite edges, the potential at each side will primarily affect only one of the spins, hence, it is important to consider differently the potential for each spin channel.

Systems with non-regular edges

Apart from zigzag and armchair edges, it is interesting to study systems with other edge type. The TB model previously described, is intended to work not only with zigzag and armchair interfaces, but with all types and shapes of interfaces. To explore the transferability of the model, systems with non-regular edges are studied. The different systems are schematized in Figure 5.13 (left). In all the systems, the number of B atoms is different to the number of N atoms. Thus, all are n- or p-doped systems, depending on whether there is more N or B, respectively. The different systems are labelled S1 to S4, and to distinguish between B- and N-rich systems the suffixes -B and -N are used. All the systems have mostly zigzag-like interfaces. System S1 is formed by non-regular strips of graphene and BN. The BN nanodomain of system S2 has armchair-like interfaces, besides the zigzag ones. Systems S3 and S4 are composed of triangular domains of BN in graphene. Using $A_{\mathrm{P}} = 0\,56$ eV·Å, the bands crossing the Fermi level of all the Sn-B systems, are more localized than those obtained with DFT. A value of 0.3 eV·Å is in better agreement with first principles. The inclusion of the interface potential represents a crucial improvement in the band structure of systems S1-B and S2-B. In systems S3-B and S4-B the inclusion of the potential is not so crucial but represents an improvement in the band structure. In the systems Sn-N, considering different values for the strength of the potential at each side makes the band structures to be in better agreement with DFT, and the values $A^{\mathrm{B}}_{\alpha} = 0\,5$ eV·Å and $A^{\mathrm{N}}_{\alpha} = 0\,8$ eV·Å are good choices to improve the bands. As in the case of B-rich systems, changes in the band structure due to the interface potential are more noticeable for the S1-N and S2-N systems. From these results, the failures of the model can be predicted, and the parameters readjusted to improve the results. In B-rich systems it is preferable to decrease the strength of the potential, while in N-rich systems it is better to increase it. This is in accordance with the Hirshfeld analysis of charges, which shows that at the B edge the interfacial charge is lower than in the N edge.

5.7 Conclusions

The properties of hybrid systems of graphene and BN are highly dependent on interfacial effects. The bound charge from the zigzag edges of h-BN induces a potential that mobile

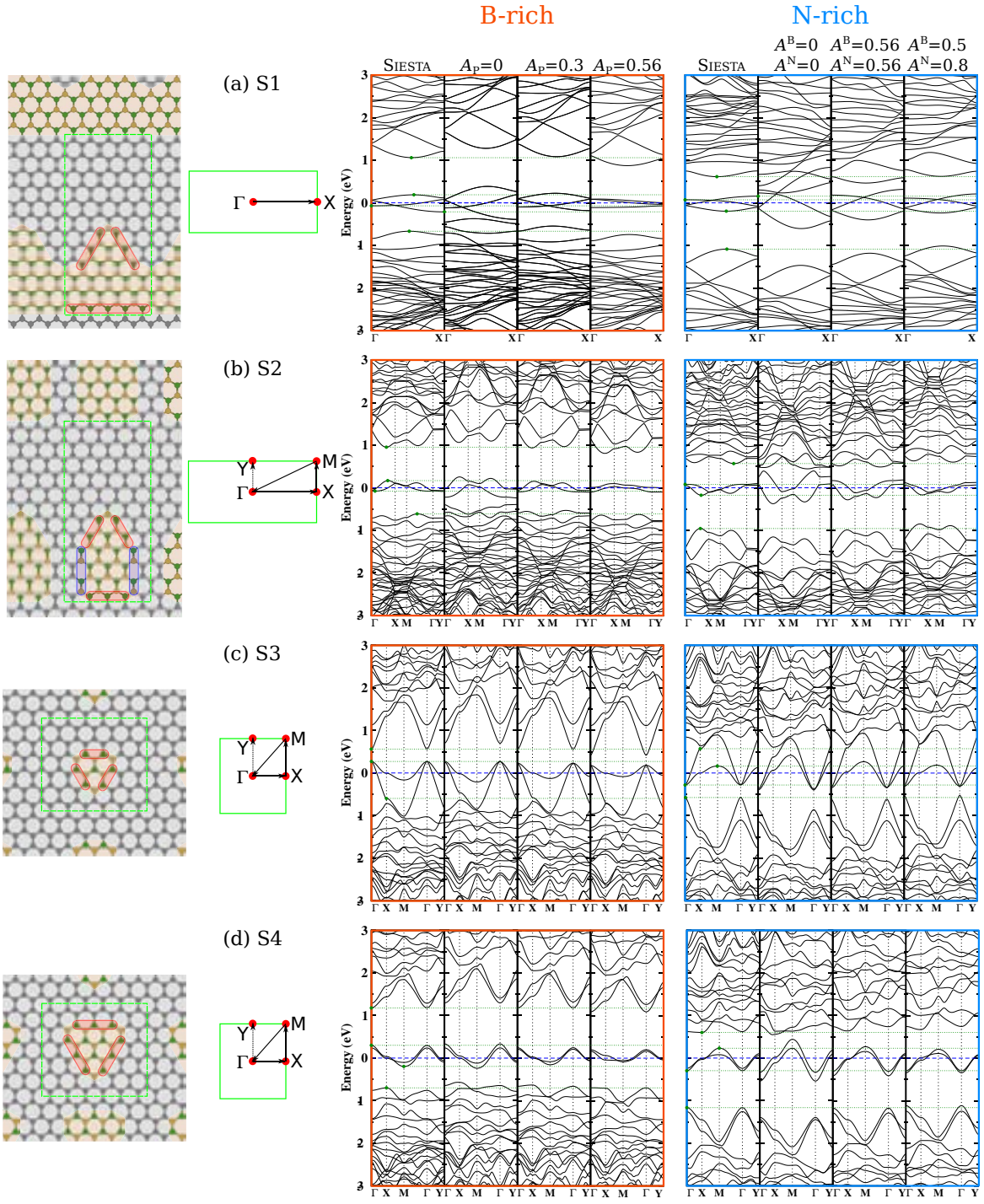

Figure 5.13: Systems with non standard edges. (a) Irregular strips of graphene and h-BN. (b) Graphene with nanodomains of h-BN with zigzag and armchair-like edges. (c) and (d) Triangular domains of h-BN in graphene of different sizes. From left to right: schematic of the systems showing the unit cell (green box) and the zigzag (red) and armchair-like (blue) interfaces; the BZ showing the path followed in the band structure calculations; band structures of Sn-B systems; band structures of Sn-N systems. The band structures show those obtained with SIESTA and with TB using different values of the potential. Dotted green lines denote important features in the bands obtained with SIESTA.

electrons from graphene tend to screen. This is represented in the TB model as a screened Coulomb potential that is added to the diagonal terms of the Hamiltonian. Suitable values for the different parameters of the potential are given. The band structures of different systems, with regular (zigzag and armchair) and irregular edges, are calculated with the TB model and compared with DFT, being in very good agreement. It is found that B-rich systems require smaller values for the amplitudes of the potential, while the opposite happens for N-rich systems. The case of spin polarized systems is also considered and appropriate values for the repulsion terms are given.

Due to its simple form, this model is suitable to study large scale systems. Electronic transport calculations could be done in systems designed with the characteristics present in experimental samples, reproducing the domain size, geometry and compositions observed in synthesised hybrid systems. Even more, a wider systematic study of different systems could reveal the most promising geometries, and serve as a guide for experimentalist to pattern graphene/h-BN in a more convenient way. Synthesized

CHAPTER 6

Strain engineering interfacial properties in coplanar C/BN hybrids

6.1 Introduction

Great experimental efforts are being devoted to tune and control the growth of hybrid systems made of C and BN,[84,98–100,103] which are also being intensively studied by first principles simulations.[87,88,90,91,95,240–242] Due to the energetics of the bonds between C, B and N,[85] it is expected a phase segregation in hybrid graphene/h-BN systems forming well separated domains of C and BN. Moreover, high-resolution scanning tunneling microscopy images show that zigzag interfaces are preferably formed in these systems.[100,103] As explained in chapter 5, the polarity of the h-BN NR (BNNR) gives an interfacial dipole, hence producing an effective electric field that acts on the graphene NR (GNR),[91] which, in turn, can become half-metallic by application of a sufficiently large in-plane electric field perpendicular to the edges of the GNR.[197] These characteristics make zigzag-edged heterostructures (both planar and tubular) particularly appealing for spintronic applications.

Due to the low atomic number of carbon, spin-orbit interactions are weak, hence, carbon-based materials are expected to have long spin-relaxation times, which are fundamental to preserve the spin state. Many devices have been designed to study the spin injection into graphene[243] and carbon nanotubes[244], the magnetoresistance in graphene nanoribbons[245,246], or graphene-based spin transistors,[247] using ferromagnetic electrodes to set

the spin orientation. However, electric field control of spin transport in a carbon-based nanodevice has advantages over magnetic-field control, like a reduced power consumption or an enhanced miniaturization, and hence, magnetoelectric effects in these carbon-nanostructures are of much interest. In addition to the half-metallicity induced by transversal external electric fields on free-standing GNR[197], magnetoelectric couplings were predicted for bilayer GNR on silicon substrates by electric bias control of charge carrier,[248] and as means to favor antiferromagnetic over ferromagnetic configurations in doped ribbons.[249] Similarly, control of magnetism through mechanical deformation would be valuable for applications.

Both, graphene and *h*-BN, have remarkable mechanical strength and flexibility, and are able to sustain huge elastic structural deformations. Although strain-modulation of bandgaps have been studied before,[55,250] little is known about the coupling of mechanical and electrostatic properties of hybrid C/BN nanostructures. This becomes critical taking into account that in non-centrosymmetric dielectric crystals, such as *h*-BN, application of mechanical strains gives rise to polarization fields, as response of the direct piezoelectric effect. Remarkable piezoelectric and flexoelectric properties in *h*-BN have been theoretically predicted,[51,52,251] and pose an alternative route for controlling electronic properties in hybrid C/BN heterostructures.

In this chapter, zigzag-edged interfaces between C and BN domains are studied to demonstrate electromechanical control of the charge and spin densities. It will be shown that the interfacial bound charges and associated electric fields can be tuned by application of an external mechanical force (stress) on the system, through direct piezoelectric effect. The modulation of the charge at the interface gives the possibility to transform a semiconducting heterostructure into a half-metal. The case of C/BC_2N heterostructures is also considered, yielding similar results to the C/BN case. The inverse effect (application of an external electric field to induce a mechanical deformation) goes together with a magnetoelectric response, that is estimated to be comparable to that of prototypical Cr_2O_3.

6.2 Computational methodology

Hybrid systems with zigzag interfaces are considered, having n_C zigzag rows of C, and n_{BN} zigzag rows of BN, with the interface along the x axis (see Figure 6.1). For notation purposes, the systems are labelled as $C_{n_C}/BN_{n_{BN}}$. Periodic boundary conditions are considered, and a vacuum layer of ~ 40 Å along the normal direction to the sheet is included to avoid spurious interactions between periodic images. Different chemical compositions and domains sizes are studied within *ab initio* density functional theory, using the spin-polarized generalized-gradient approximation,[232] as implemented in the SIESTA code.[122] Troullier-Martin type

pseudopotentials [159] and numerical atomic orbitals with double-ζ plus polarization [123] were used to describe the electronic valence states. In Figure 6.1 a diagram of tensile and compressive strain fields is shown. In the case of tensile strain, the superlattice periodicity of the planar systems is fixed imposing strains along the y axis, while relaxing the atomic positions. Compressive strains, on the other hand, result in non-planar ground-state geometries that are modelled with periodic out-of-plane displacements

$$u_z(y) = A\sin(\mathbf{k}\cdot\mathbf{r} + \quad) \tag{6.1}$$

where $\mathbf{k}$ is the corrugation wave vector and is a phase. Compressive strains along both, the armchair (perpendicular to the interface) and zigzag (parallel to the interface) directions are considered, thus, $\mathbf{k}$ takes the values $2\beta\boldsymbol{y}\ \gamma$ or $2\beta\boldsymbol{x}\ \gamma$. To model the systems with strains along the zigzag direction, a supercell of 4 unit cells repeated in the x direction is used. γ and γ are defined by the length of the supercell in the x and y directions, respectively (see Figure 6.1), while the amplitude A is determined by structural relaxation of the atoms. The atomic positions are optimized until the forces are lower than 0.02 eV/Å. An accurate description of the boundary electronic states requires a smooth sampling of the reciprocal space, and typically Monkhorst-Pack grids of at least $67 \times 1 \times 1$ are used to sample the Brillouin zone.

Piezoelectric constants

In dielectric materials without inversion symmetry, an electric moment is developed by application of stress. This is known as the direct piezoelectric effect. Inversely, when an electric field is applied to a crystal, it can develop a deformation in the crystalline structure, in what is known as the converse piezoelectric effect. Both phenomena are characterized by the third-rank piezoelectric tensors, which relate the stress, σ_{ij}, and strain $_{ij}$, with the polarization of the crystal, $\mathbf{P}$, and the applied electric field, $\mathbf{E}$. The components of the piezoelectric tensors are calculated as

$$d_{i\,jk} = \left(\frac{P_i}{\sigma_{jk}}\right) = \left(\frac{\ _{jk}}{E_i}\right) \tag{6.2}$$

$$e_{i\,jk} = \left(\frac{P_i}{\ _{jk}}\right) = -\left(\frac{\sigma_{jk}}{E_i}\right) \tag{6.3}$$

where i, j, k denote Cartesian components. For the purposes of this chapter, we are interested in variations of the polarization with changes in the strain, which are captured by $e_{i\,jk}$, and in the following only the coefficients of this tensor are considered. Due to the D_{3h} symmetry of h-BN, the piezoelectric response is characterized by a single element of the

piezoelectric tensor, $e_{y\,yy} = e_{yy}$.[251] To obtain e_{yy}, the polarization of h-BN under different strains is calculated with SIESTA using the geometric Berry phase approach,[252] resulting in a piezoelectric constant of $2\,06 \times 10^{-10}$ C/m, in good agreement with the values reported by Naumov *et al.*[51] ($\sim 2\,68 \times 10^{-10}$ C/m), Duerloo *et al.*[251] ($1\,38 \times 10^{-10}$ C/m), and López-Suárez *et al.*[253] ($3\,08 \times 10^{-10}$ C/m).

6.3 Tensile strain

The tensile strain field is depicted in Figure 6.1(a). Different superlattices are considered with sizes of the C and BN domains in the range $3 \leq n_{\mathrm{C}} \leq 9$ and $3 \leq n_{\mathrm{BN}} \leq 10$. Strains as large as 15% are applied to the different systems. Larger strains break the layer at the C B edge. The relevant bands close to the Fermi level (E_{F}) are the bonding C B (β_{B}), and anti-bonding C N (β^*_{N}), which are mainly localized at carbon atoms close to the B and N edges, respectively (see Figure 6.4).[91] In the half-metallic phase, these two edge states become spin-polarized with antiferromagnetic coupling due to the intrinsic electrostatic potential induced by the polar BN interface. The difference in formal polarization values between graphene and h-BN domains gives rise to bound charges at the edges of BN, which are partially compensated by charge carriers from graphene, resulting in the C atom at the B edge ($\mathrm{C_B}$) to be negatively charged, while the C atom at the N edge ($\mathrm{C_N}$) is positively charged.

Application of a tensile strain in planar C/BN heterostructures increases the effective in-plane polarization of BN domains and consequently the bound (polarization) charge at the interface. To compensate this bound charge, electrons are transferred from B to N edges. Figure 6.2(a) plots the Hirshfeld population analysis for the C, B and N atoms at the C/BN interfaces, as a function of the applied uniaxial strain for the system $\mathrm{C_4/BN_{10}}$. Boron and nitrogen atoms have positive and negative charges, respectively, and under strain their values increase almost linearly due to the direct piezoelectric response in h-BN. Changes in the polarization due to the strain, result in changes in the bound charge at the same rate. Thus, the evolution of the charge at the interface can be described as

$$\gamma(\ _{yy}) = \gamma_0 + e_{yy}\ _{yy} \tag{6.4}$$

where γ_0 is the interfacial charge in the unstrained system. As all the charge redistribution takes place within the edge electronic states which are very localized, the total edge charges can be defined as the sum of the Hirshfeld populations for the B atom at the edge and $\mathrm{C_B}$, and the N atom at the edge and $\mathrm{C_N}$. As seen in Figure 6.2(a), these total charges (diamond symbols) nicely follow the curve predicted by e_{yy} (red dashed lines). Notice that $\mathrm{C_B}$ ($\mathrm{C_N}$),

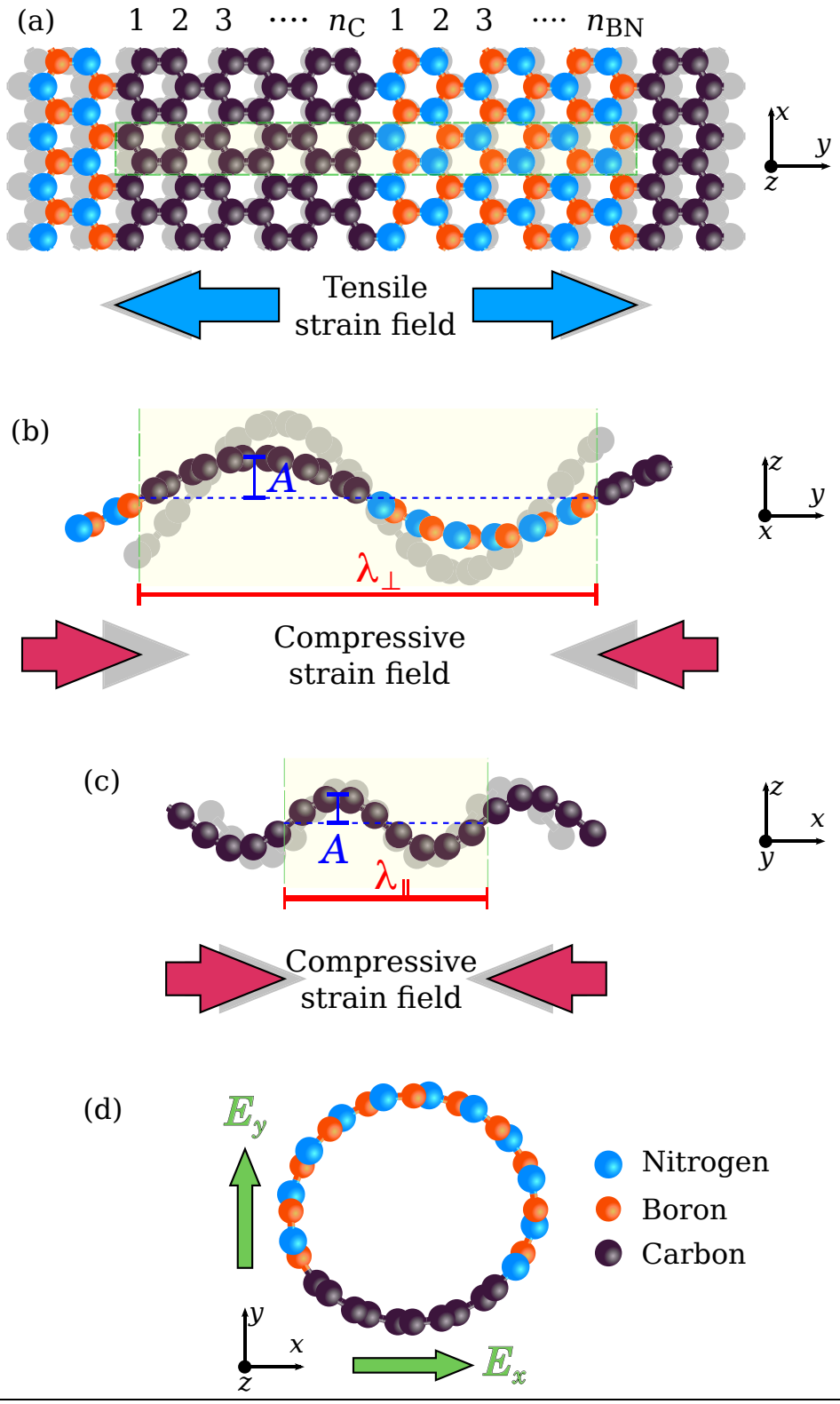

Figure 6.1: (a) Model geometry for planar C_6/BN_6 ($n_C = 6$, $n_{BN} = 6$) superlattice. Simulation unit cell is shown as a dashed green box. Number of graphene and *h*-BN zigzag chains are marked on top. (b) Lateral view of the C_6BN_6 monolayer under compressive strain perpendicular to the interface. (c) Lateral view of a monolayer with four cells repeated along the x direction and compressive strain parallel to the interface. (d) Geometry for the (8,8) hybrid C/BN armchair nanotube, composed of a C strip with 5 zigzag chain and a BN strip with 11 zigzag chains.

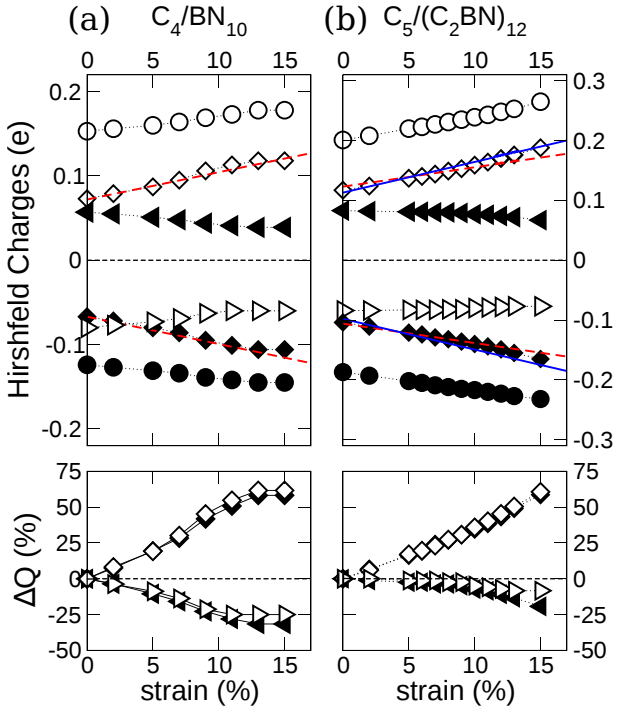

Figure 6.2: Hirshfeld population analysis for atoms at the boron-edge (empty) and nitrogen-edge (filled symbols), as a function of tensile strain field perpendicular to the interface between (a) C/BN and (b) C/BC_2N domains. Atomic charges for C (BN) are shown as triangles (circles), while diamonds correspond to the sum of charges of C and B (N) at the C–B (C–N) interface. Dashed red (solid blue) line corresponds to the theoretical prediction for the bound charge due to the BN (BC_2N) polarization. Bottom panels plots the change in the atomic charge at each interface.

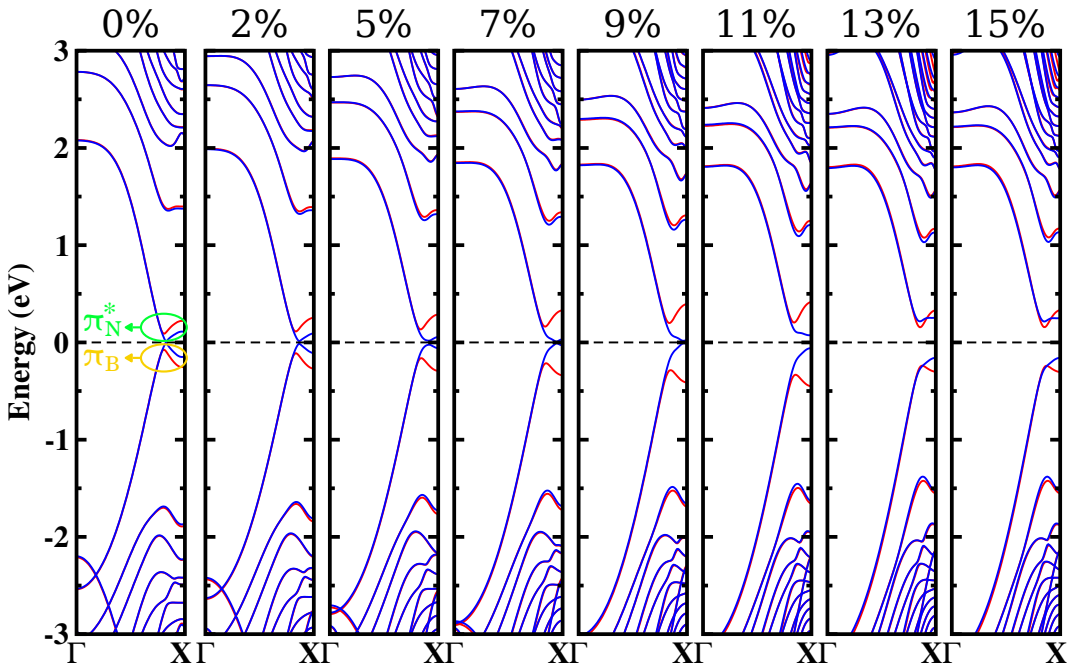

Figure 6.4: Evolution of the spin-resolved band structure of the system C_4/BN_{10} with the applied strain. Red lines correspond the α spin, while blue lines correspond to β spin. The strain in each case is indicated on top. The circles in the band structure with zero strain denote the character of the bands close to E_F.

is negatively (positively) charged and its net charge decreases for increasing strains, because free electrons (negatively charged) in the carbon strip are transferred from B-edge to N-edge. This results in an increased stabilization of the β^*_N state. Figure 6.4 shows the evolution of the band structure for a half-metallic phase under strain, and how the lowering of the β^*_N band with β-spin comes at the expense of the depopulation of the β_B band with the same spin. This translates into an increase in the edge magnetization, that is characterized in terms of the Mulliken populations on the C atoms at the edges, C_B and C_N, plotted in Figure 6.5(a). For large strain fields however, the β-spin β^*_N band becomes fully occupied (β_B empty) and a gap opens. At this point, the occupied bands close to the Fermi level are localized at the N-edge for β-spin and the B-edge for α-spin, while the empty bands are B- and N-edge localized (for β- and α-spins, respectively).

Interestingly, one can use strain not only to tune the gaps in systems that are originally half-metallic, but also to induce such state for systems that, unstrained, are semiconducting. This is illustrated in Figure 6.6, where the band gaps for each spin component, as well as the inter-atomic distances for C N and C B at the edges are plotted as a function of tensile strain for a variety of chemical compositions. For the semiconducting systems, the increased polarization of BN domain under strain triggers the half-metallic instability in the graphene domain. Under extreme strain loads, the nanosheet breaks at the C B junction,

as illustrated by the dramatic increase in the interatomic distances (striped region). The strain threshold needed to close the gap depends on the width of both, C and BN ribbons. Once the system becomes half-metallic, further strain will open the gap for both spins as in previously analysed C_4/BN_{10} case. Consequently, there is a range of strain values under which one could tune half-metallic properties in these hybrid C/BN heterostructures (white regions in the figure).

Graphene/BC_2N hybrids

Recently, ultrathin graphene nanoribbons segregated from boron-carbon-nitride domains have been experimentally observed.[106] Scanning tunnelling microscopy imaging found two dominant configurations for stoichiometrically percolated BC_2N, that correspond to the type I and type II polymorphic structures theoretically predicted in the late 80 s.[254] The structure of the different types of BC_2N proposed by Liu *et al.*[254] are shown in Figure 6.7. From the isomers found experimentally, type II does not have inversion symmetry (nor 3-fold symmetries) making it a piezoelectric material. The calculated piezoelectric coefficient is $e_{yy} = 3\ 89 \times 10^{-10}$ C/m, which is found to be larger than that for h-BN, and in fact, unlike h-BN, type II BC_2N has a formal in-plane polarization of $0\ 713 \times 10^{-10}$ C/m pointing along the armchair direction.

Strain-induced half-metallicity is possible for C-domains broader than 5 zigzag chains, while the band gaps in ultra-narrow graphene ribbons are too large to experience the Zener-breakdown mechanism induced by the polarization discontinuity. The strain-evolution of the atomic charges at the interface are again in agreement with the prediction obtained from the piezoelectric response (Equation 6.4), as shown in Figure 6.2(b) for the $C_5/(BC_2N)_{12}$ system. The edge magnetization plotted in Figure 6.5(b) reveals the critical strain to develop half-metallicity in the system (around 8%), and the steep increase in the edge magnetization unravels a piezo-antiferromagnetic effect.

Remarkably, strain-engineering the electronic properties at zigzag-interfaces is not limited to the C/BN hybrid monolayers discussed here, but could also be applicable to other bidimensional dielectric materials and interfaces, and we suggest that ultra-narrow graphene ribbons embedded in BC_2N would be an excellent playground to explore the experimental realization of these effects.

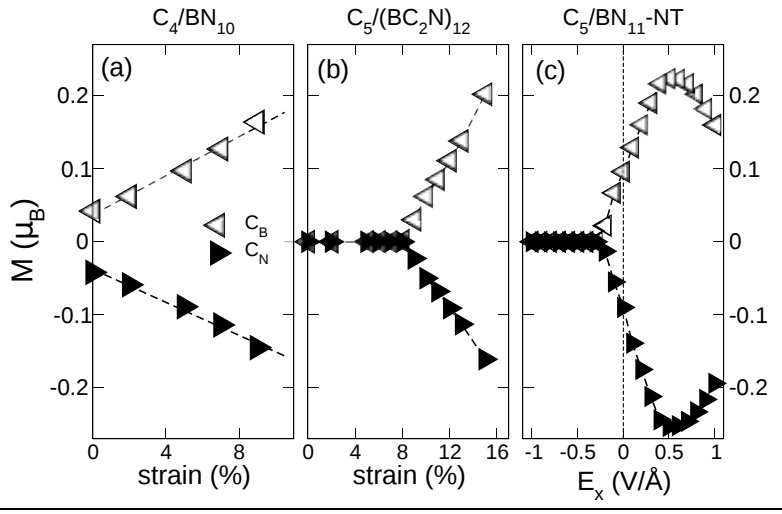

Figure 6.5: Evolution of edge magnetization, defined from the Mulliken populations for carbon atoms at the interfaces, as a function of tensile strain for (a) C_4/BN_{10} superlattice, and (b) $C_5/(BC_2N)_{12}$ superlattice, and (c) as a function of external electric field for C_5/BN_{11} armchair nanotube.

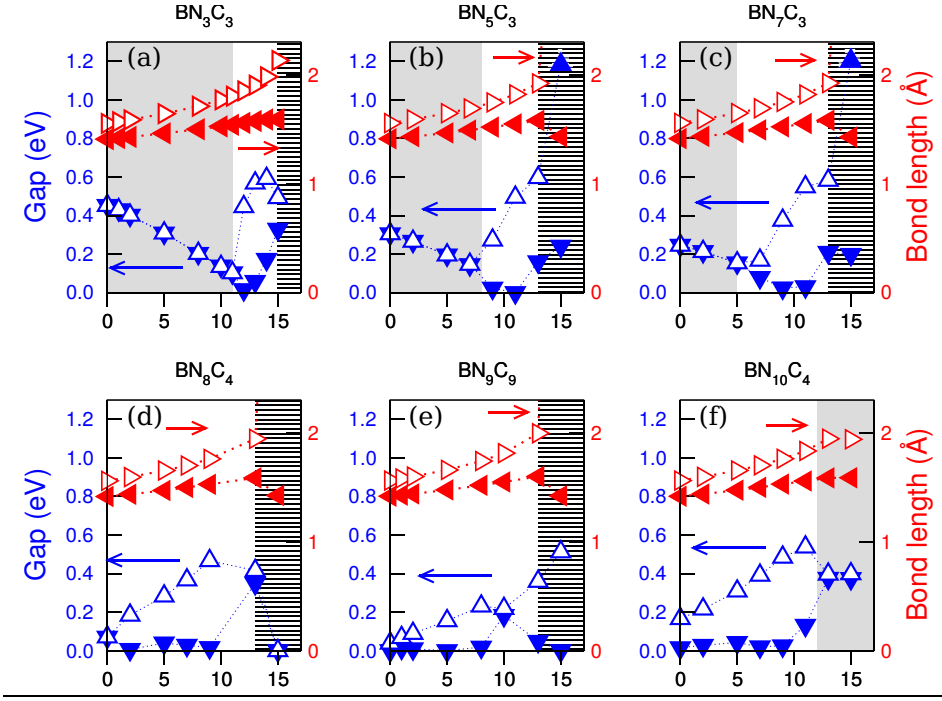

Figure 6.6: Band gaps for both spin components (up and down blue triangles) as a function of tensile strain for (a)-(d) semiconducting, (e) semimetalic and (f) half-metallic C/BN zigzag-edged superlattices. Right empty and left filled red triangles show the C–B and C–N bond lengths, respectively. Energy (left) and length (right) scales are in eV and Å.

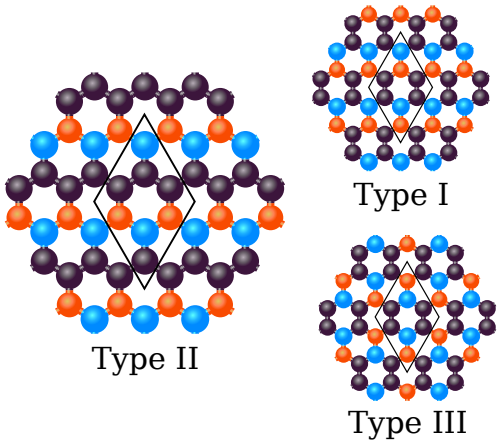

Figure 6.7: Atomic structure of the different types of BC_2N proposed in Ref. [254].

6.4 Compressive strain

Uniaxial compressive strains applied perpendicularly to the C/BN interface results in an armchair-oriented corrugation of the monolayer, and a locally induced polarization pointing in the opposite direction to the formal polarization,[51] hence reducing the value of the bound charge at the interface. However, a compressive strain parallel to the C/BN interface, as that shown in Figure 6.1(c), would result into an increase in the polarization-induced interfacial charge, and a tunability of the bandstructure. The effects of this strain are characterized by the factor $f = A\ \gamma$. The amplitude A is measured in the relaxed structure and has different values for the graphene and BN parts due to the different lattice parameters, being A always larger in the h-BN region. The C/BN superlattice is repeated four times in the x direction and different wavelengths γ are imposed to induce different strains.

In Figure 6.8(a), the band structures considering different strains are shown for the system C_5/BN_5. Although the system remains as a half-semimetal under all strains considered, the enlargement of the gap for the α spin is noticeable. While tensile strain perpendicular to the interface increases the charge at the edges with a very localized effect, for compressive strain along the x axis, the effect is more delocalized. The Hirshfeld charge population for each atom in the hybrid C_5/BN_5 under different strains is shown in Figure 6.8(b). The charge at the interfacial atoms varies very little, with the changes being comparable to those of other *bulk* atoms. In C atoms, the changes are negligible, while the charge in B (N) atoms tend to decrease (increase) with the applied strain. Remarkably, there are changes in the charge of B and N that not depend in the position with respect to the interface, but with respect to the curvature of the sheet, as in the case of BN nanotubes.[255,256] For $f_{BN} = 0\ 2$, it can be seen in Figure 6.8(b) that atoms at the same distance from the interface have

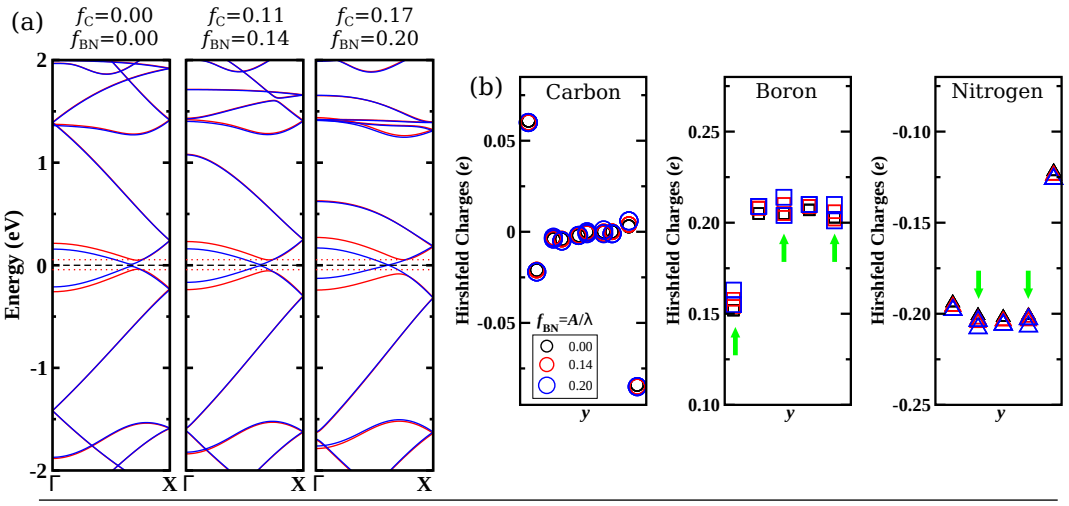

Figure 6.8: (a) Evolution of the band structure with the applied compressive strain. The factors $f = A\ \gamma$ for the graphene and BN strips are indicated on top. (b) Hirshfeld charges plotted in dependence with the position along the y axis for different strains with $f_{\mathrm{BN}} = 0$ (black), 0.14 (red) and 0.20 (blue). Green arrows denote cases where a clear dependence of the charge with the curvature of the sheet is observed for $f_{\mathrm{BN}} = 0$ 2.

different charges (green arrows), with the largest charge corresponding to atoms at zones with maximum curvature.

Considering larger values of γ (by repeating the superlattice in the x direction) could produce a modulation of the bound charges along the interface, and a stronger compression would increase the curvature, and hence induce larger charge differences. More work is needed in this respect, and interesting phenomena may rise in hybrid systems due to variable polarizations and magnetization at the interface.

6.5 Magnetoelectric effect

Now, possible magnetoelectric effects are explored. Tubular geometries are considered with transversal electric fields applied along the C strip and perpendicular to the periodic tube axis, as shown in Figure 6.1(d). With this geometry, the difficulties to simulate electric fields under periodic boundary conditions, due to the intrinsic non-periodic nature of the position operator,[257] are avoided. Algo aqui, molecular dynamics simulation had shown that GNR and BNNR placed one atop the other can spontaneously bind forming a hybrid NT.[87] The nanotube considered is the armchair (8,8) nanotube with zigzag-edged C/BN domains composed of n_{C} zigzag chains of C and n_{BN} zigzag chains of BN along the tube axis following the geometries discussed in the literature.[87–89,241,242]. The values of n_{C} and n_{BN} considered, cover several types of systems including semiconducting ($n_{\mathrm{C}} = 3$, $n_{\mathrm{BN}} = 13$), metallic ($n_{\mathrm{C}} = 11$, $n_{\mathrm{BN}} = 5$) and half-metallic ($n_{\mathrm{C}} = 5$, $n_{\mathrm{BN}} = 11$) nanotubes. An additional

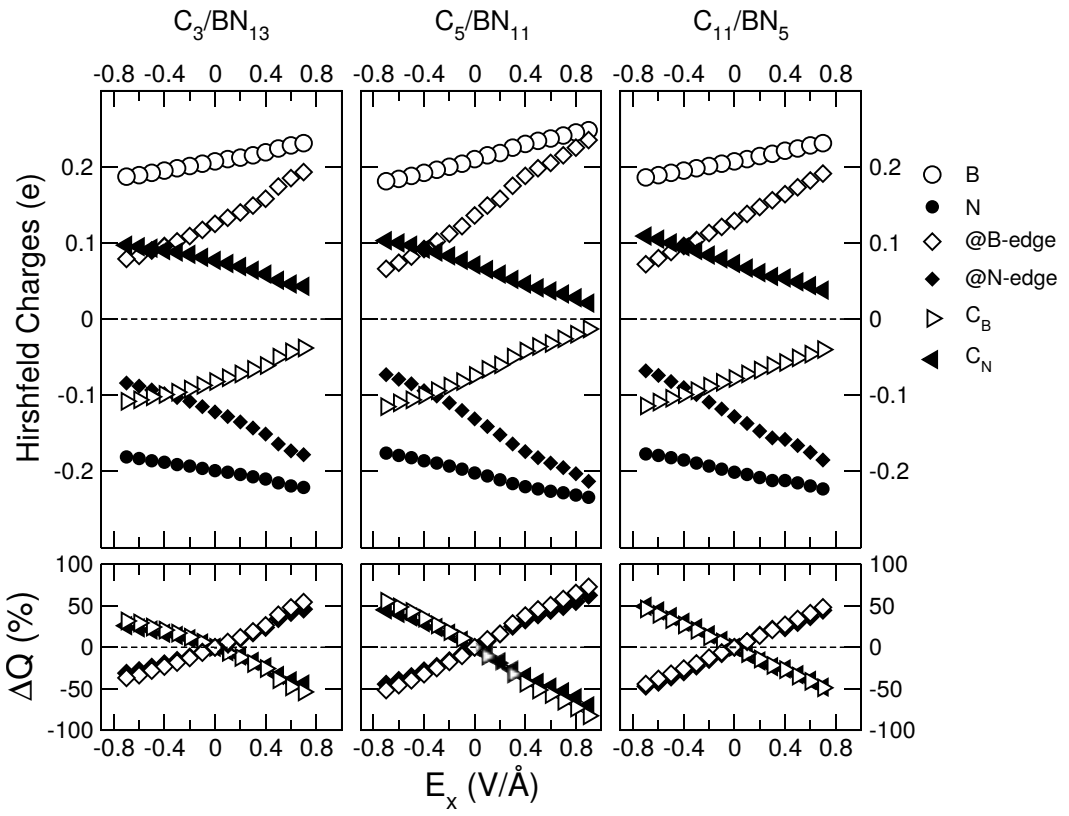

Figure 6.10: Hirshfeld charge population for hybrid nanotubes with different chemical compositions. The notation is the same as in Figure 6.2.

set of *ghost* orbitals (*s*- and *p*-like) cylindrically distributed around the tube axis are used to improve the description of nearly free electron states known to exist in BN nanotubes.[258]

The system with $n_C = 5$ and $n_{BN} = 11$, for this particular chirality results in a half-metallic ground state.[242] Without electric field, C_B and C_N have $\sim 0.1\ \mu_B$ aligned antiparallel at each interface. When an electric field is applied in the positive (negative) x direction of the C/BN nanotube, electrons in the C-ribbon are pushed towards the N-edge (B edge), and depleted at the B edge (N edge). The change in C_N (C_B) charge Hirshfeld population increases (decreases) linearly with the external field strength (Figure 6.10). This charge reorganization has a direct effect on the edge magnetic properties. For fields below -0.3 V/Å edge magnetism is killed, as shown in Figure 6.5(c). The linear magnetoresistance at low-field, defined as:

$$\alpha_L = \mu_0 \frac{\Delta M_L}{E}, \tag{6.5}$$

where ΔM_L denotes the change in linear magnetization at the C/BN interface, can be obtained from this figure, and is four times larger than the value obtained for bilayer GNR on silicon substrates.[248] The bulk magnetoelectric coefficient (considering the volume of the whole hybrid C/BN nanotube) would be ~ 1 ps/m, comparable to that of prototypical

magnetoelectric material Cr_2O_3. Notice that the dependence of the edge magnetism on the external electric field is completely different to that observed in graphene nanoribbons. [248] To understand this behavior the nature of the edge bands must be considered.

Figure 6.12 shows the band structure close to the Fermi level for both spin orientations, as a function of the electric field. As for tensile uniaxial strains, an electric fields pointing in the positive x direction, stabilizes the β^*_{N} band, and conducting electrons (β spin) are transferred to the N-edge from the B-edge (β_{B} band moves to higher energies), increasing the magnetization at the former interface. At approximately $+0\ 4$ V/Å, a small gap opens and the edge magnetization reaches a maximum. Stronger electric fields move the α-bands (β_{B} up and β^*_{N} down) closer to the Fermi level, and for $E \geq 0\ 9$ V/Å,the gap closes and the system becomes again *half-semimetallic*, with a spin-inversion from the original state. An electric field pointing in the negative x direction would give a response similar to that of a compressive uniaxial strain, shifting the β_{B} valence band towards lower energies (and moving up β^*_{N}), so that extra electrons populate the β-spin metallic levels. Eventually, the β_{B} β-band becomes completely filled (as was its α-spin counterpart), edge magnetization disappears, and a gap opens below -0.3 V/Å.

Electric fields oriented along the y axis do not have a large effect on the edge-state populations. This is because the conducting electrons, localized at both C N and C B interfaces are equally perturbed by the electric field, and no, or very little, charge-reorganization takes place at the edge C atoms for fields below $0\ 5$ V/Å. Most of the changes affect the charge populations at the nanotube s top (center of BN strip) and bottom (center of C strip), although some charge redistribution takes place at the interfacial B atoms, that linearly increase with the electric field.

6.6 Conclusions

Using first-principles electronic structure calculations, we have shown that the electronic properties of hybrid C/BN nanostructures can be tuned taking advantage of the dielectric properties in the BN domains. In particular, for zigzag-shaped interfaces, uniaxial strains or external electric fields, can regulate the edge magnetism (piezomagnetic, flexomagnetic, or magnetoelectric response) and tune half-metallicity through control of the polarization-induced interfacial bound charges.

Although only the field-response of CBN nanotubes has been studied, some results can be extrapolated to planar geometries. In particular, similar ME effects can be expected for hybrid CBN nanosheets when an in-plane electric field is applied perpendicular to the C/BN interface. In this configuration, the piezoelectric response of BN and the edge-state

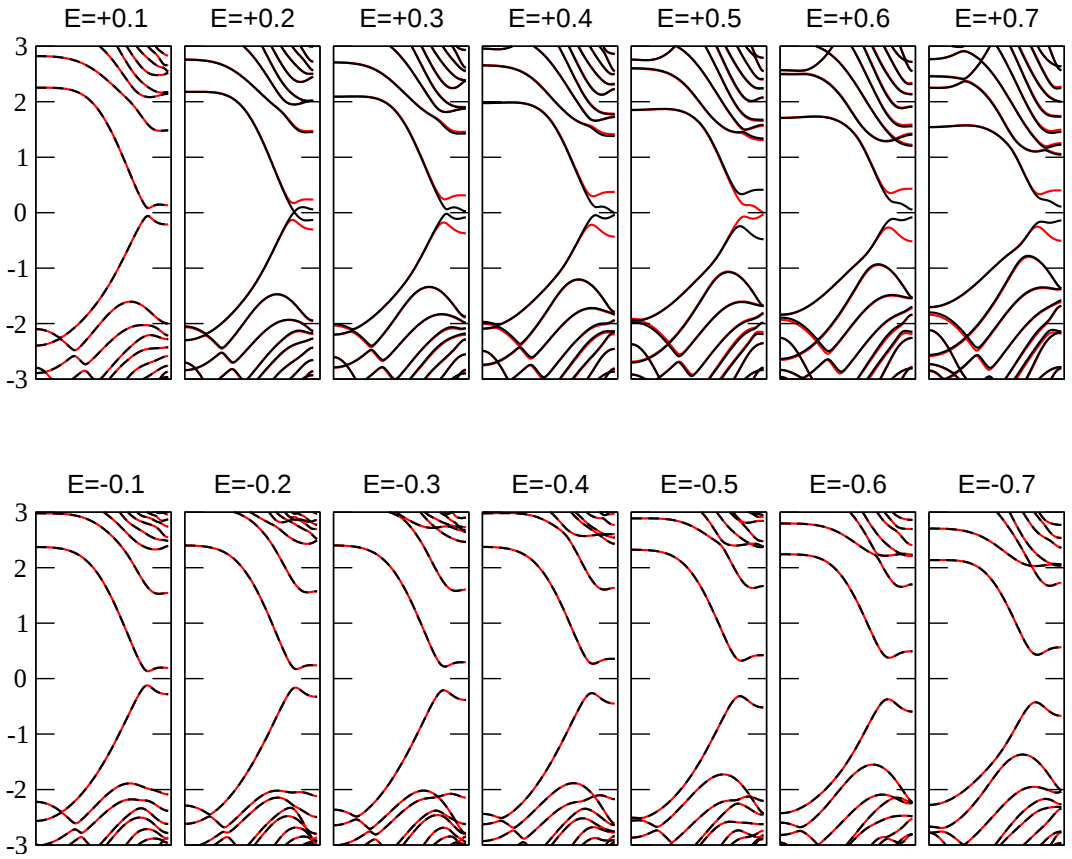

Figure 6.12: Bandstructure close to the Fermi level for the C_3/BN_{13} nanotube with applied electric fields along the x direction. Thin black solid, and red dotted line correspond to α and β spins. Energies are given in eV. Field strengths are given (in V/Å) on top of each panel.

spin polarization at the interfaces will be similar to that reported here for fields along the x-axis. Hence, the changes in the bandstructure and edge population are expected to give a surface ME coefficient comparable to that of GNR on silicon, though different in nature. Notice also that the surface ME constant for these half-metallic heterostructures would be two orders of magnitude larger than the universal constant predicted at the surface of bulk half-metals.[259]

It has been shown that the relative composition and sizes of C and BN domains determine the band gaps of C/BN heterostructures[88,90,91,211,241]. Very low concentrations of C give rise to semiconducting or insulating properties, while large concentrations suppress potential half-metallic properties. This, of course will change the strengths of the threshold fields, but the ME effect will remain, and the results presented here will hold. The systems studied here represent an alternative approach to tune the electronic properties allowing to dynamically move from one electronic behavior to another. Interestingly, He *et. al.* showed that half-metallicity could also be obtained when a few C zigzag chains (GNR) are attached to a BNNR.[211] Considering that the edges of BN monolayers are relatively smooth, this could also be an interesting path for the experimental realization of spintronic devices based in hybrid C/BN nanostructures.

CHAPTER 7

Summary

The importance of graphene in many scientific and technological fields was recognized by the award of the Nobel prize to A. Geim and K. Novoselov merely 6 years after its discovery. It was clear that to exploit all the potentiality of this novel material a devoted scientific research was much needed. On the one hand, the synthesis methods have to improve in order to have control over the quality, size (including the thickness), functionalization, doping and reactivity of graphene samples. The synthesised graphene sample can be used directly in the substrate where it was grown, deposited in other material to sustain it or isolated to form suspended graphene, hence avoiding any undesired substrate interaction. Due to its two-dimensional (2D) nature, graphene behaves like a flexible membrane, and the use of substrates were important for mechanical stabilization. On the other hand, a better knowledge of the properties of graphene was important to model and predict its behaviour. This can be done by experimental characterizations or theoretical approaches. By joining the expertise in synthesising suitable samples with the understanding of its properties, graphene-based devices were expected to excel over other materials in many applications.

After graphene was isolated and observed for the first time, an avalanche of new 2D materials arose, each one with different promising features. The compatibility of graphene with h-BN helps in the formation of hybrid systems that can lead to new properties. In this thesis, we present the study of stacked and co-planar heterostructures formed from graphene and h-BN. The main methods used here were density functional theory (DFT) and tight binding (TB), which were described in chapter 2. Both were used to calculate electronic structure, with the

difference that each one acts at different levels of accuracy, being DFT more accurate, but also more computationally demanding. While each method was more suitable for different systems, depending on the number of atoms, both were compatible and complementary. In this work, simple TB models were proposed based in our observations of DFT calculations for hybrid C/BN systems. Our parametrized TB Hamiltonians were fitted to DFT data to properly describe large scale systems that can reach millions of atoms.

Chapter 3 dealt with the study of moiré patterns formed by graphene on top of h-BN. DFT calculations were performed for different superlattices with different sizes. The density of states (DOS) was obtained for each system using a large number of k-points to sample the Brillouin zone. The dense grid was needed to clearly observe the dips appearing in the DOS as an effect of the h-BN substrate reported in previous STS experiments. The position in energy of these dips was found to be in agreement with perturbative predictions. A discussion was presented about different features in the band structure, such as the opening of gaps at non-zero energy that cause the appearance of the dips. The analysis of lattice distortions was then presented. It was found that the largest moirés have stronger off-plane and in-plane modulations. Is remarkable the fact that even with the large off-plane modulation found for one of the largest systems, no gap was opened at the Fermi level. Systems formed of by graphene sandwiched between two monolayers of h-BN were also considered in the thesis, in order to study the effect of graphene encapsulation. It was found that the dips in the DOS can be enhanced, and the in-plane distortions increased, while the off-plane displacements were decreased. This work allowed us to enlighten many effects that the superlattice moiré potential induce in graphene. The behaviour of largest systems can be then inferred by extrapolating of the characteristics of the systems studied here.

We then moved to the study of transport properties of the stacked graphene/h-BN heterostructures using the information of our previous DFT calculations. In chapter 4, the conductivity was calculated using the Kubo formalism of electronic transport within the TB description. The effect of the h-BN substrate was modelled with the simple expression proposed by Sachs *et al.*[139] where an additional mass term was included in the Hamiltonian to represent a local breaking of the sublattice symmetry. From the DFT calculations done in chapter 3, the local atomic energies were obtained to estimate the strength of the potential. This strength was used as the amplitude of the modulation of the substrate potential. Additional to the superlattice potential, disorder was added to graphene by randomly changing the on-site energies of C atoms. Two types of disorder were considered: short range Anderson disorder, and long range Gaussian potential. We observed that the mean free path and the resistivity were obtained for both types of disorder. The mean free path tends to decrease compared to the case where no substrate potential was considered. The signature of the moiré potential was a peak in the mean free path at the same energy as the dip in

the DOS. The same happens in the resistivity in good agreement with experiments.[62,63] As the strength of the disorder was increased, the characteristic features of the moiré potential were blurred to the point where they were completely dimmed. At this strong disorder, quantum interferences become important and localization effects can be observed. Also, the effect of a gap opening at the main Dirac point was analysed. While the resistivity at zero energy increased substantially, the secondary peaks were not affected. Finally, the interesting effect of a magnetic field acting in the moiré superlattice was treated. Apart from the well known Landau levels present in pristine graphene, other sets of Landau levels can be observed. While the main Landau levels have a quadratic behaviour, the Landau levels coming from the superlattice have a linear dependence with the magnetic field. As a future work, several improvements to the model can be done to describe in a more faithful way the stacked graphene/h-BN systems. This could include the electron-hole asymmetry of the dips present in the experiments, and the consideration of lattice strain that was considered to open a gap in graphene.[134]

In chapter 5 the electronic properties of in-plane hybrids were studied. After a DFT analysis of different systems with zigzag and armchair interfaces a model was proposed to describe these heterostructures within TB. The model was mainly based in the properties of polarization of h-BN. The polarization discontinuity that appears when h-BN was cut along the zigzag direction gives place to a induced electric field that acts in the graphene region. A simple electrostatic model of point charges at the interface was considered, which represent the physical bound charge accumulated at the edge of h-BN. The parameters of the TB model were fitted to zigzag systems, but were proven to work with armchair and chiral interfaces. The inclusion of the spin degree of freedom was also considered. The spin was very important in zigzag edged systems for two reasons: first, a half-metallic state can be induced for certain compositions, and second, magnetic ordering can appear at the interface. These two characteristics make graphene/h-BN heterostructures promising for spintronics applications. The TB model of hybrid systems was also useful to study theoretically systems like the ones obtained experimentally with large domains of each component. Electronic and transport properties can be obtained for realistic systems using very large simulation cells and considering interfacial effects.

Besides being able to change the gap of graphene in hybrid systems by considering different compositions and edge terminations, it was possible to dynamically tune its electronic properties taking advantage of the electromechanical response of h-BN. This was the topic of study in chapter 6. The piezoelectric constant of h-BN was calculated within DFT using the Berry-phase theory of polarization. In C/BN superlattices with zigzag interfaces, the piezoelectric tuning of the polarization induced bond charge, and was studied by applying tensile strain perpendicular to the interface. The behaviour of these systems was well described by

the piezoelectric response of pristine *h*-BN. Interestingly, graphene/BC_2N heterostructures, also studied, have a larger piezoelectric response than the hybrids with *h*-BN. This becomes useful for applications with experimentally synthesised systems of graphene/BC_2N.[106] The flexoelectric effect was also discussed, but now by application of compressive strains parallel to the zigzag interface. Tuning of the gap for one of the spins was found, along with curvature induced charge redistribution in the BN part of the hybrid system. Finally, the magnetoelectric response in hybrid nanotubes was probed to have an important effect. It was expected that the same effect remains in co-planar hybrids. The electric field-dependent spin redistribution of these systems could be useful for spintronics applications.

APPENDIX A

Wannier Functions

The electronic ground state in periodic solids is usually described by Bloch states $_{n\mathbf{k}}$, n and $\mathbf{k}$ being quantum numbers denoting the band index, and the crystal momentum, respectively. These Bloch states can be represented as

$$_{n\mathbf{k}}(\mathbf{r}) = u_{n\mathbf{k}}(\mathbf{r})e^{i\mathbf{k}\cdot\mathbf{r}} \tag{A.1}$$

where $u_{n\mathbf{k}}$ has the periodicity of the crystal. Wannier functions (WFs) are a representation in real-space of a set of Bloch eigenstates $_{n\mathbf{k}}(\mathbf{r})$, related by a Fourier transformation [260,261]

$$w_n(\mathbf{r}-\mathbf{R}_I) = \frac{\Omega_{\text{cell}}}{(2\beta)^3} \int_{\text{BZ}} {}_{n\mathbf{k}}(\mathbf{r})e^{-i\mathbf{k}\cdot\mathbf{R}_I}d^3\mathbf{k} \tag{A.2}$$

where $\mathbf{R}_I$ are lattice vectors and Ω_{cell} is the volume of the unit cell. These functions form an orthonormal set and can be used as a minimal basis for many theoretical studies. A more general form of this expression includes a unitary matrix transformation that mixes the bands at wave-vector $\mathbf{k}$

$$w_n(\mathbf{r}-\mathbf{R}) = \frac{\Omega_{\text{cell}}}{(2\beta)^3} \int_{\text{BZ}} \sum_{m=1}^{N} U_{mn}(\mathbf{k}) \; {}_{m\mathbf{k}}(\mathbf{r})e^{-i\mathbf{k}\cdot\mathbf{R}}d^3\mathbf{k} \tag{A.3}$$

with $U_{mn}(\mathbf{k})$ the unitary matrix of dimension N that defines the gauge transformation. The specific shape and range of the WFs depend on the choice of the unitary matrix. This, in addition to the arbitrariness of the phase factor, make WFs non-unique. From all the

possible ways of obtaining the WFs, the most common method is the one by Marzari and Vanderbilt [262] for finding Maximally Localised WFs (MLWF) by minimising the sum of the quadratic spreads of the WFs about their centres defined by

$$\Omega = \sum_{n}^{N} \left[\langle r^2 \rangle_n - |\mathbf{r}_n|^2 \right] \tag{A.4}$$

The quantities $\langle r^2 \rangle$ and $\mathbf{r}_n$ are computed through the Berry-phase theory of polarization, using a discretized k-space mesh. [261] The expressions for the expected values are: [262]

$$\mathbf{r}_n = -\frac{1}{N} \sum_{\mathbf{k}\,\mathbf{b}} w_b \mathbf{b}\, \mathrm{Im} \ln M_{nn}(\mathbf{k}, \mathbf{b}) \tag{A.5}$$

and

$$\langle r^2 \rangle_n = \frac{1}{N} \sum_{\mathbf{k}\,\mathbf{b}} w_b \left(1 - |M_{nn}(\mathbf{k}, \mathbf{b})|^2 + [\mathrm{Im} \ln M_{nn}(\mathbf{k}, \mathbf{b})]^2 \right) \tag{A.6}$$

where $M_{mn}(\mathbf{k}, \mathbf{b}) = \langle u_{m\mathbf{k}} | u_{n\,\mathbf{k}+\mathbf{b}} \rangle$ is the overlap matrix between Bloch orbitals, $\mathbf{b}$ are vectors connecting a mesh point to its near neighbours and w_b are weight factors associated with each shell of neighbours $b = |\mathbf{b}|$. Furthermore, the spread can be decomposed into two parts

$$\Omega = \Omega_{\mathrm{I}} + \tilde{\Omega} \tag{A.7}$$

being Ω_{I} gauge-invariant and $\tilde{\Omega}$ gauge-dependent. The minimisation of the spread can be done with steepest-descents or conjugate-gradient algorithms. For this, a reference set of Bloch orbitals are needed as starting point. Using trial functions $g_n(\mathbf{r})$ as initial guess for the Wannier functions, these are projected onto the set of Bloch bands and orthonormalized, being necessary to provide the coefficients of the projection

$$A_{mn}(\mathbf{k}) = \langle \psi_{m\mathbf{k}} | g_n \rangle \tag{A.8}$$

The trial functions considered in WANNIER90 [235] are hydrogenic orbitals with the radial part, $R_n(r)$, being equal to the Schrodinger solution of the hydrogen atom, and the angular dependence taken into account as the real spherical harmonics, $\Theta_{lm_r}(\theta, \lambda)$, so $g_n(\mathbf{r}) = R_n(r)\Theta_{lm_r}(\theta, \lambda)$. With this construction of the initial guess linear combinations of atomic orbitals can be used to represent hybrid orbitals.

In some cases, entangled energy bands should be considered, being necessary to use a disentanglement procedure [234] by defining an energy window (the *outer window*) such that for each k-point there are $N^{\mathbf{k}}_{\mathrm{win}} \geq N$ states within the window. With these $N^{\mathbf{k}}_{\mathrm{win}}$ states, a set of

N Bloch states is obtained by performing a unitary transformation

$$u^*_{n\mathbf{k}} = \sum_{m}^{N^{\mathbf{k}}_{\text{win}}} U^{\text{dis}}_{mn}(\mathbf{k})\, u_{m\mathbf{k}} \tag{A.9}$$

and minimising Ω_{I} with respect to $U^{\text{dis}}(\mathbf{k})$. With this transformation, the energy bands obtained may not correspond to any of the original energy bands. For this reason, a second energy window (the *inner* or *frozen window*) is introduced within which the properties of the system are preserved exactly.

APPENDIX B

Electric polarization

The modern theory of polarization [119] defines the electric polarization of an insulator as a bulk quantity with ionic and electronic contributions, $\mathbf{P}_{\text{bulk}} = \mathbf{P}_{\text{ion}} + \mathbf{P}_e$. The ionic part, $\mathbf{P}_{\text{ion}}$, is simply

$$\mathbf{P}_{\text{ion}} = \frac{e}{\Omega_{\text{cell}}} \sum_{\alpha=1}^{N} Z_\alpha \mathbf{R}_\alpha \tag{B.1}$$

where e is the electron charge, Ω_{cell} is the volume of the cell, N the number of atoms in the cell, Z_α the charge of the ionic core α, and $\mathbf{R}_\alpha$ its position. The electronic part can be expressed in terms of Wannier functions [262] as:

$$\mathbf{P}_e = -\frac{2e}{\Omega_{\text{cell}}} \sum_{j=1}^{N_{\text{el}}/2} \mathbf{r}_j \tag{B.2}$$

where N_{el} is the number of electrons in the cell, and $\mathbf{r}_j$ are the Wannier centres (for more on Wannier functions see Appendix A).

The interface theorem, formulated by Vanderbilt and King-Smith, [119,213] establish the polarization bound charge γ, in absence of lattice strains, that appears at the interface of two dielectric materials. This interfacial charge is given by the difference in bulk polarization between both materials

$$(\mathbf{P}_1 - \mathbf{P}_2) \cdot \mathbf{n} = \gamma \tag{B.3}$$

where $\mathbf{n}$ is a vector normal to the interface.

APPENDIX C

Atomic population analysis

In DFT calculations the electronic density of any system is always readily available, but a problem may rise when trying to partition the electronic density among the different atoms in the system. To assign a charge to each atom is an useful tool to determine how the charge is redistributing and the characteristics of chemical bonds between atoms. A well known method to obtain such atomic charges is the one proposed by Mulliken.[167] This method to obtain the electronic population of atoms is straightforward to implement when using linear combinations of atomic orbitals (LCAO) as basis. Having a system represented in terms of basis functions $\lambda_\mu(\mathbf{r})$ centred on atoms $\mathbf{A}$, the wave function is expanded as

$$_i(\mathbf{r}) = \sum_{\mathbf{A}\ \mu\ \mathbf{A}} c_{\mu i}\lambda_\mu(\mathbf{r}) \tag{C.1}$$

The total number of electrons in the system, N, is then given by

$$N = \sum_{\mathbf{A}\,\mathbf{B}\,\mu\ \mathbf{A}}^{\ \ \ \ \ \ \nu\ \mathbf{B}} \mathbf{D}_{\mu\,\nu} S_{\mu\,\nu} \tag{C.2}$$

where $S_{\mu\,\nu}$ is the overlap matrix, defined as in Equation 2.22. $\mathbf{D}$ is the density matrix

$$\mathbf{D}_{\mu\,\nu} = \sum_{i}^{\mathrm{occ}} f_i c_{\mu i} c_{\nu i} \tag{C.3}$$

where f_i is the orbital occupation and the sum is over all occupied orbitals.

The Mulliken population associated to the orbital λ_μ is

$$Q_\mu = \mathbf{D}_{\mu\,\mu} S_{\mu\,\mu} + \frac{1}{2} \sum_{\nu=\mu} (\mathbf{D}_{\mu\,\nu} S_{\mu\,\nu} + \mathbf{D}_{\nu\,\mu} S_{\nu\,\mu}) \tag{C.4}$$

and the atomic population of atom $\mathbf{A}$ is obtained by summing up all the Mulliken charges of the orbitals centred on that atom

$$Q_{\mathbf{A}}^{\text{Mulliken}} = Z_{\mathbf{A}} - \sum_{\mu \in \mathbf{A}} Q_\mu \tag{C.5}$$

where $Z_{\mathbf{A}}$ is the atomic charge.

The Hirshfeld approach[237] is based in the definition of a *promolecule* charge obtained as the sum of the ground state atomic densities disposed as in the total system

$$\alpha_{\text{promolecule}}(\mathbf{r}) = \sum_{\mathbf{A}} \alpha_{\mathbf{A}}(\mathbf{r}) \tag{C.6}$$

At each point, a deformation density can be associated to each atom from the total charge density α_{total}:

$$\alpha_{\mathbf{A}}^{\text{molecule}}(\mathbf{r}) = \frac{\alpha_{\mathbf{A}}(\mathbf{r})}{\alpha_{\text{promolecule}}(\mathbf{r})} \alpha_{\text{total}}(\mathbf{r}) \tag{C.7}$$

Finally, the Hirshfeld atomic charge is given by integrating the deformation density and subtracting it from the nuclear charge

$$Q_{\mathbf{A}}^{\text{Hirshfeld}} = Z_{\mathbf{A}} - \int \frac{\alpha_{\mathbf{A}}(\mathbf{r})}{\alpha_{\text{promolecule}}(\mathbf{r})} \alpha_{\text{total}}(\mathbf{r}) d\mathbf{r} \tag{C.8}$$

Bibliography

[1] Kroto, H. W., Heath, J. R., O Brien, S. C., Curl, R. F., and Smalley, R. E. C_{60}: Buckminsterfullerene. *Nature* **318**, 162 (1985).

[2] Hohenberg, P. and Kohn, W. Inhomogeneous Electron Gas. *Phys. Rev.* **136**, B864 B871, Nov (1964).

[3] Kohn, W. and Sham, L. J. Self-Consistent Equations Including Exchange and Correlation Effects. *Phys. Rev.* **140**, A1133 A1138, Nov (1965).

[4] Andreoni, W. *The Physics of Fullerene-Based and Fullerene-Related Materials*. Springer Science & Business Media, (2000).

[5] Saito, R., Dresselhaus, G., and Dresselhaus, M. S. *Physical Properties of Carbon Nanotube*. Imperial College Press, (1998).

[6] Novoselov, K. S., Geim, A. K., Morozov, S. V., Jiang, D., Zhang, Y., Dubonos, S. V., Grigorieva, I. V., and Firsov, A. A. Electric Field Effect in Atomically Thin Carbon Films. *Science* **306**(5696), 666 669 (2004).

[7] Tsoukleri, G., Parthenios, J., Papagelis, K., Jalil, R., Ferrari, A. C., Geim, A. K., Novoselov, K. S., and Galiotis, C. Subjecting a Graphene Monolayer to Tension and Compression. *Small* **5**(21), 2397 2402 (2009).

[8] Wallace, P. R. The Band Theory of Graphite. *Phys. Rev.* **71**, 622 634, May (1947).

[9] Novoselov, K. S., Geim, A. K., Morozov, S. V., Jiang, D., Katsnelson, M. I., Grigorieva, I. V., Dubonos, S. V., and Firsov, A. A. Two-dimensional gas of massless Dirac fermions in graphene. *Nature* **438**(7065), 197 200, November (2005).

[10] Castro Neto, A. H., Guinea, F., Peres, N. M. R., Novoselov, K. S., and Geim, A. K. The electronic properties of graphene. *Rev. Mod. Phys.* **81**, 109, Jan (2009).

[11] Hwang, E. H. and Das Sarma, S. Acoustic phonon scattering limited carrier mobility in two-dimensional extrinsic graphene. *Phys. Rev. B* **77**, 115449, Mar (2008).

[12] Bolotin, K. I., Sikes, K. J., Hone, J., Stormer, H. L., and Kim, P. Temperature-Dependent Transport in Suspended Graphene. *Phys. Rev. Lett.* **101**, 096802, Aug (2008).

[13] Du, X., Skachko, I., Barker, A., and Andrei, E. Y. Approaching ballistic transport in suspended graphene. *Nat. Nanotechnol.* **3**, 491 495 (2008).

[14] Zhang, Y., Brar, V. W., Wang, F., Girit, C., Yayon, Y., Panlasigui, M., Zettl, A., and Crommie, M. F. Giant phonon-induced conductance in scanning tunnelling spectroscopy of gate-tunable graphene. *Nat. Phys.* **4**, 627 630 (2008).

[15] Wehling, T. O., Grigorenko, I., Lichtenstein, A. I., and Balatsky, A. V. Phonon-Mediated Tunneling into Graphene. *Phys. Rev. Lett.* **101**, 216803, Nov (2008).

[16] Katsnelson, M. and Geim, A. Electron scattering on microscopic corrugations in graphene. *Phil. Trans. R. Soc. A* **366**(1863), 195 204, January (2008).

[17] Fratini, S. and Guinea, F. Substrate-limited electron dynamics in graphene. *Phys. Rev. B* **77**, 195415, May (2008).

[18] Teague, M. L., Lai, A. P., Velasco, J., Hughes, C. R., Beyer, A. D., Bockrath, M. W., Lau, C. N., and Yeh, N.-C. Evidence for Strain-Induced Local Conductance Modulations in Single-Layer Graphene on SiO2. *Nano Letters* **9**(7), 2542 2546 (2009). PMID: 19534500.

[19] Das Sarma, S., Adam, S., Hwang, E. H., and Rossi, E. Electronic transport in two-dimensional graphene. *Rev. Mod. Phys.* **83**, 407 470, May (2011).

[20] Song, H. S., Li, S. L., Miyazaki, H., Sato, S., Hayashi, K., Yamada, A., Yokoyama, N., and Tsukagoshi, K. Origin of the relatively low transport mobility of graphene grown through chemical vapor deposition. *Sci. Rep.* **2**, 337 (2012).

[21] Berger, C., Song, Z., Li, X., Wu, X., Brown, N., Naud, C., Mayou, D., Li, T., Hass, J., Marchenkov, A. N., Conrad, E. H., First, P. N., and de Heer, W. A. Electronic Confinement and Coherence in Patterned Epitaxial Graphene. *Science* **312**(5777), 1191 1196 (2006).

[22] Brar, V. W., Zhang, Y., Yayon, Y., Ohta, T., McChesney, J. L., Bostwick, A., Rotenberg, E., Horn, K., and Crommie, M. F. Scanning tunneling spectroscopy of inhomogeneous electronic structure in monolayer and bilayer graphene on SiC. *Applied Physics Letters* **91**(12), (2007).

[23] N Diaye, A. T., Bleikamp, S., Feibelman, P. J., and Michely, T. Two-Dimensional Ir Cluster Lattice on a Graphene Moiré on Ir(111). *Phys. Rev. Lett.* **97**, 215501, Nov (2006).

[24] Marchini, S., Gunther, S., and Wintterlin, J. Scanning tunneling microscopy of graphene on Ru(0001). *Phys. Rev. B* **76**, 075429, Aug (2007).

[25] Lui, C. H., Liu, L., Mak, K. F., Flynn, G. W., and Heinz, T. F. Ultraflat graphene. *Nature* **462**, 339 341 (2009).

[26] Chen, J.-H., Jang, C., Xiao, S., Ishigami, M., and Fuhrer, M. S. Intrinsic and extrinsic performance limits of graphene devices on SiO_2. *Nat. Nanotechnol.* **3**(4) (2008).

[27] Sabio, J., Seoánez, C., Fratini, S., Guinea, F., Neto, A. H. C., and Sols, F. Electrostatic interactions between graphene layers and their environment. *Phys. Rev. B* **77**, 195409, May (2008).

[28] Tan, Y.-W., Zhang, Y., Bolotin, K., Zhao, Y., Adam, S., Hwang, E. H., Das Sarma, S., Stormer, H. L., and Kim, P. Measurement of Scattering Rate and Minimum Conductivity in Graphene. *Phys. Rev. Lett.* **99**, 246803, Dec (2007).

[29] Cho, S. and Fuhrer, M. S. Charge transport and inhomogeneity near the minimum conductivity point in graphene. *Phys. Rev. B* **77**, 081402, Feb (2008).

[30] Chen, J.-H., Jang, C., Adam, S., Fuhrer, M. S., Williams, E. D., and Ishigami, M. Charged-impurity scattering in graphene. *Nat. Phys.* **4**, 377 381 (2008).

[31] Deshpande, A., Bao, W., Miao, F., Lau, C. N., and LeRoy, B. J. Spatially resolved spectroscopy of monolayer graphene on SiO_2. *Phys. Rev. B* **79**, 205411, May (2009).

[32] Ishigami, M., Chen, J. H., Cullen, W. G., Fuhrer, M. S., and Williams, E. D. Atomic structure of graphene on SiO_2. *Nano Lett.* **7**(6), 1643 1648, June (2007).

[33] Martin, J., Akerman, N., Ulbricht, G., Lohmann, T., Smet, J. H., von Klitzing, K., and Yacoby, A. Observation of electron-hole puddles in graphene using a scanning single-electron transistor. *Nat Phys* **4**(2), 144 148 (2008).

[34] Zhang, Y., Brar, V. W., Girit, C., Zettl, A., Crommie, M. F., et al. Origin of spatial charge inhomogeneity in graphene. *Nat. Phys.* **5**, 722 726 (2009).

[35] Kim, E.-A. and Neto, A. H. C. Graphene as an electronic membrane. *Europhys. Lett.* **84**(5), 57007 (2008).

[36] Guinea, F., Katsnelson, M. I., and Vozmediano, M. A. H. Midgap states and charge inhomogeneities in corrugated graphene. *Phys. Rev. B* **77**, 075422, Feb (2008).

[37] Prada, E., San-Jose, P., León, G., Fogler, M. M., and Guinea, F. Singular elastic strains and magnetoconductance of suspended graphene. *Phys. Rev. B* **81**, 161402, Apr (2010).

[38] Adam, S., Hwang, E. H., Galitski, V. M., and Sarma, S. D. A self-consistent theory for graphene transport. *PNAS* **104**(47), 18392 18397, November (2007).

[39] Chen, F., Xia, J., Ferry, D. K., and Tao, N. Dielectric Screening Enhanced Performance in Graphene FET. *Nano Letters* **9**(7), 2571 2574 (2009). PMID: 19496554.

[40] Ponomarenko, L. A., Yang, R., Mohiuddin, T. M., Katsnelson, M. I., Novoselov, K. S., Morozov, S. V., Zhukov, A. A., Schedin, F., Hill, E. W., and Geim, A. K. Effect of a High-κ Environment on Charge Carrier Mobility in Graphene. *Phys. Rev. Lett.* **102**, 206603, May (2009).

[41] Konar, A., Fang, T., and Jena, D. Effect of high-κ gate dielectrics on charge transport in graphene-based field effect transistors. *Phys. Rev. B* **82**, 115452, Sep (2010).

[42] Li, X., Barry, E. A., Zavada, J. M., Buongiorno Nardelli, M., and Kim, K. W. Surface polar phonon dominated electron transport in graphene. *Applied Physics Letters* **97**(23), (2010).

[43] Farmer, D. B., Chiu, H.-Y., Lin, Y.-M., Jenkins, K. A., Xia, F., and Avouris, P. Utilization of a Buffered Dielectric to Achieve High Field-Effect Carrier Mobility in Graphene Transistors. *Nano Letters* **9**(12), 4474 4478 (2009). PMID: 19883119.

[44] Novoselov, K. S., Jiang, D., Schedin, F., Booth, T. J., Khotkevich, V. V., Morozov, S. V., and Geim, A. K. Two-dimensional atomic crystals. *Proc. Natl. Acad. Sci. U.S.A.* **102**, 10451 10453, July (2005).

[45] Watanabe, K., Taniguchi, T., and Kanda, H. Direct-bandgap properties and evidence for ultraviolet lasing of hexagonal boron nitride single crystal. *Nat Mater* **3**, 404 409 (2004).

[46] Kubota, Y., Watanabe, K., Tsuda, O., and Taniguchi, T. Deep Ultraviolet Light-Emitting Hexagonal Boron Nitride Synthesized at Atmospheric Pressure. *Science* **317**(5840), 932 934 (2007).

[47] Gao, R., Yin, L., Wang, C., Qi, Y., Lun, N., Zhang, L., Liu, Y.-X., Kang, L., and Wang, X. High-Yield Synthesis of Boron Nitride Nanosheets with Strong Ultraviolet Cathodoluminescence Emission. *The Journal of Physical Chemistry C* **113**(34), 15160 15165 (2009).

[48] Chen, Y., Zou, J., Campbell, S. J., and Le Caer, G. Boron nitride nanotubes: Pronounced resistance to oxidation. *Applied Physics Letters* **84**(13), 2430 2432 (2004).

[49] Golberg, D., Bando, Y., Tang, C. C., and Zhi, C. Y. Boron Nitride Nanotubes. *Advanced Materials* **19**(18), 2413 2432 (2007).

[50] Ouyang, T., Chen, Y., Xie, Y., Yang, K., Bao, Z., and Zhong, J. Thermal transport in hexagonal boron nitride nanoribbons. *Nanotechnology* **21**(24), 245701 (2010).

[51] Naumov, I., Bratkovsky, A. M., and Ranjan, V. Unusual Flexoelectric Effect in Two-Dimensional Noncentrosymmetric sp^2-Bonded Crystals. *Phys. Rev. Lett.* **102**, 217601, May (2009).

[52] Michel, K. H. and Verberck, B. Theory of elastic and piezoelectric effects in two-dimensional hexagonal boron nitride. *Phys. Rev. B* **80**, 224301, Dec (2009).

[53] Pedersen, T. G., Flindt, C., Pedersen, J., Mortensen, N. A., Jauho, A.-P., and Pedersen, K. Graphene antidot lattices: designed defects and spin qubits. *Phys. Rev. Lett.* **100**(13), 136804, April (2008).

[54] Balog, R., J ˚rgensen, B., Nilsson, L., Andersen, M., Rienks, E., Bianchi, M., Fanetti, M., Lfl gsgaard, E., Baraldi, A., Lizzit, S., Sljivancanin, Z., Besenbacher, F., Hammer, B., Pedersen, T. G., Hofmann, P., Hornekfl r, L., et al. Bandgap opening in graphene induced by patterned hydrogen adsorption. *Nat. Mater.* **9**(4), 315 319, April (2010).

[55] Naumov, I. I. and Bratkovsky, A. M. Gap opening in graphene by simple periodic inhomogeneous strain. *Phys. Rev. B* **84**(24), 245444, December (2011).

[56] Dean, C., Young, A., Meric, I., Lee, C., Wang, L., Sorgenfrei, S., Watanabe, K., Taniguchi, T., Kim, P., Shepard, K., et al. Boron nitride substrates for high-quality graphene electronics. *Nat. Nanotechnol.* **5**(10), 722 726 (2010).

[57] Decker, R., Wang, Y., Brar, V. W., Regan, W., Tsai, H.-Z., Wu, Q., Gannett, W., Zettl, A., and Crommie, M. F. Local electronic properties of graphene on a BN substrate via scanning tunneling microscopy. *Nano Lett.* **11**(6), 2291 2295 (2011).

[58] Xue, J., Sanchez-Yamagishi, J., Bulmash, D., Jacquod, P., Deshpande, A., Watanabe, K., Taniguchi, T., Jarillo-Herrero, P., and LeRoy, B. J. Scanning tunnelling microscopy and spectroscopy of ultra-flat graphene on hexagonal boron nitride. *Nat. Mater.* **10**(4), 282 5 (2011).

[59] Mayorov, A. S., Gorbachev, R. V., Morozov, S. V., Britnell, L., Jalil, R., Ponomarenko, L. A., Blake, P., Novoselov, K. S., Watanabe, K., Taniguchi, T., and Geim, A. K. Micrometer-Scale Ballistic Transport in Encapsulated Graphene at Room Temperature. *Nano Letters* **11**(6), 2396 2399 (2011).

[60] Gannett, W., Regan, W., Watanabe, K., Taniguchi, T., Crommie, M. F., and Zettl, A. Boron nitride substrates for high mobility chemical vapor deposited graphene. *Applied Physics Letters* **98**(24), (2011).

[61] Yankowitz, M., Xue, J., Cormode, D., Sanchez-Yamagishi, J., Watanabe, K., Taniguchi, T., Jarillo-Herrero, P., Jacquod, P., and LeRoy, B. Emergence of Superlattice Dirac Points in Graphene on Hexagonal Boron Nitride. *Nat. Phys.* **8**, 382 386 (2012).

[62] Hunt, B., Sanchez-Yamagishi, J. D., Young, A. F., Yankowitz, M., LeRoy, B. J., Watanabe, K., Taniguchi, T., Moon, P., Koshino, M., Jarillo-Herrero, P., and Ashoori, R. C. Massive Dirac fermions and Hofstadter butterfly in a van der Waals heterostructure. *Science* **340**, 1427, Jun (2013).

[63] Dean, C. R., Wang, L., Maher, P., Forsythe, C., Ghahari, F., Gao, Y., Katoch, J., Ishigami, M., Moon, P., Koshino, M., Taniguchi, T., Watanabe, K., Shepard, K. L., Hone, J., and Kim, P. Hofstadter s butterfly and the fractal quantum Hall effect in moiré superlattices. *Nature* **497**, 598, May (2013).

[64] Ponomarenko, L. A., Gorbachev, R. V., Yu, G. L., Elias, D. C., Jalil, R., Patel, A. A., Mishchenko, A., Mayorov, A. S., Woods, C. R., Wallbank, J. R., Mucha-Kruczynski, M., Piot, B. A., Potemski, M., Grigorieva, I. V., Novoselov, K. S., Guinea, F., Fal ko, V. I., and Geim, A. K. Cloning of Dirac fermions in graphene superlattices. *Nature* **497**, 594, May (2013).

[65] Guo, T., Jin, C., and Smalley, R. E. Doping bucky: formation and properties of boron-doped buckminsterfullerene. *The Journal of Physical Chemistry* **95**(13), 4948 4950 (1991).

[66] Pradeep, T., Vijayakrishnan, V., Santra, A. K., and Rao, C. N. R. Interaction of nitrogen with fullerenes: nitrogen derivatives of C60 and C70. *The Journal of Physical Chemistry* **95**(26), 10564 10565 (1991).

[67] Stephan, O., Ajayan, P. M., Colliex, C., Redlich, P., Lambert, J. M., Bernier, P., and Lefin, P. Doping Graphitic and Carbon Nanotube Structures with Boron and Nitrogen. *Science* **266**(5191), 1683 1685 (1994).

[68] Redlich, P., Loeffler, J., Ajayan, P., Bill, J., Aldinger, F., and Ruhle, M. B-C-N nanotubes and boron doping of carbon nanotubes. *Chem. Phys. Lett.* **260**(3-4), 465 470 (1996).

[69] Terrones, M., Ajayan, P., Banhart, F., Blase, X., Carroll, D., Charlier, J., Czerw, R., Foley, B., Grobert, N., Kamalakaran, R., Kohler-Redlich, P., Ruhle, M., Seeger, T., and Terrones, H. N-doping and coalescence of carbon nanotubes: synthesis and electronic properties. *Appl. Phys. A* **74**(3), 355 361 (2002).

[70] Glerup, M., Steinmetz, J., Samaille, D., Stéphan, O., Enouz, S., Loiseau, A., Roth, S., and Bernier, P. Synthesis of N-doped SWNT using the arc-discharge procedure . *Chemical Physics Letters* **387**(1 3), 193 197 (2004).

[71] Ortiz-Medina, J., García-Betancourt, M. L., Jia, X., Martínez-Gordillo, R., Pelagio-Flores, M. A., Swanson, D., Elías, A. L., Gutiérrez, H. R., Gracia-Espino, E., Meunier, V., Owens, J., Sumpter, B. G., Cruz-Silva, E., Rodríguez-Macías, F. J., López-Urías, F., Munoz Sandoval, E., Dresselhaus, M. S., Terrones, H., and Terrones, M. Nitrogen-Doped Graphitic Nanoribbons: Synthesis, Characterization, and Transport. *Adv. Funct. Mater.* **23**(30), 3755 3762 (2013).

[72] Wei, D., Liu, Y., Wang, Y., Zhang, H., Huang, L., and Yu, G. Synthesis of N-Doped Graphene by Chemical Vapor Deposition and Its Electrical Properties. *Nano Letters* **9**(5), 1752 1758 (2009). PMID: 19326921.

[73] Kawaguchi, M. B/C/N Materials Based on the Graphite Network. *Adv. Mater.* **9**(8), 615 625 (1997).

[74] Kaner, R., Kouvetakis, J., Warble, C., Sattler, M., and Bartlett, N. Boron-carbon-nitrogen materials of graphite-like structure . *Mat. Res. Bull.* **22**(3), 399 404 (1987).

[75] Kouvetakis, J., Sasaki, T., Shen, C., Hagiwara, R., Lerner, M., Krishnan, K., and Bartlett, N. Novel aspects of graphite intercalation by fluorine and fluorides and new B/C, C/N and B/C/N materials based on the graphite network. *Synthetic Metals* **34**(1 3), 1 7 (1990).

[76] Popov, C., Saito, K., Yamamoto, K., Ouchi, A., Nakamura, T., Ohana, Y., and Koga, Y. Synthesis of nitrogen-rich B C N materials from melamine and boron trichloride. *J. Mater. Sci.* **33**(5), 1281 1286 (1998).

[77] Miyamoto, Y., Rubio, A., Cohen, M. L., and Louie, S. G. Chiral tubules of hexagonal BC_2N. *Phys. Rev. B* **50**, 4976 4979, Aug (1994).

[78] Weng-Sieh, Z., Cherrey, K., Chopra, N. G., Blase, X., Miyamoto, Y., Rubio, A., Cohen, M. L., Louie, S. G., Zettl, A., and Gronsky, R. Synthesis of $B_xC_yN_z$ nanotubules. *Phys. Rev. B* **51**, 11229 11232, Apr (1995).

[79] Suenaga, K., Colliex, C., Demoncy, N., Loiseau, A., Pascard, H., and Willaime, F. Synthesis of Nanoparticles and Nanotubes with Well-Separated Layers of Boron Nitride and Carbon. *Science* **278**(5338), 653 655 (1997).

[80] Zhang, Y., Gu, H., Suenaga, K., and Iijima, S. Heterogeneous growth of B-C-N nanotubes by laser ablation. *Chemical Physics Letters* **279**(5 6), 264 269 (1997).

[81] Suenaga, K., Willaime, F., Loiseau, A., and Colliex, C. Organisation of carbon and boron nitride layers in mixed nanoparticles and nanotubes synthesised by arc discharge. *Appl. Phys. A* **68**(3), 301 308 (1999).

[82] Kohler-Redlich, P., Terrones, M., Manteca-Diego, C., Hsu, W., Terrones, H., Ruhle, M., Kroto, H., and Walton, D. Stable BC_2N nanostructures: low-temperature production of segregated C/BN layered materials . *Chem. Phys. Lett.* **310**(5 6), 459 465 (1999).

[83] Golberg, D., Dorozhkin, P. S., Bando, Y., Dong, Z.-C., Grobert, N., Reyes-Reyes, M., Terrones, H., and Terrones, M. Cables of BN-insulated B C N nanotubes. *Appl. Phys. Lett.* **82**(8), 1275 1277 (2003).

[84] Enouz, S., Stéphan, O., Cochon, J.-L., Colliex, C., and Loiseau, A. C-BN Patterned Single-Walled Nanotubes Synthesized by Laser Vaporization. *Nano Lett.* **7**(7), 1856 1862 (2007). PMID: 17585829.

[85] Nozaki, H. and Itoh, S. Structural stability of BC_2N. *Journal of Physics and Chemistry of Solids* **57**(1), 41 49 (1996).

[86] Choi, J., Kim, Y.-H., Chang, K. J., and Tománek, D. Itinerant ferromagnetism in heterostructured C/BN nanotubes. *Phys. Rev. B* **67**, 125421, Mar (2003).

[87] Du, A., Chen, Y., Zhu, Z., Lu, G., and Smith, S. C. C-BN Single-Walled Nanotubes from Hybrid Connection of BN/C Nanoribbons: Prediction by ab initio Density Functional Calculations. *Journal of the American Chemical Society* **131**(5), 1682 1683 (2009). PMID: 19152268.

[88] Zhang, Z.-Y., Zhang, Z., and Guo, W. Stability and Electronic Properties of a Novel C-BN Heteronanotube from First-Principles Calculations. *J. Phys. Chem. C* **113**(30), 13108 13114 (2009).

[89] Huang, B., Si, C., Lee, H., Zhao, L., Wu, J., Gu, B.-L., and Duan, W. Intrinsic half-metallic BN C nanotubes. *Appl. Phys. Lett.* **97**(4), (2010).

[90] Ding, Y., Wang, Y., and Ni, J. Electronic properties of graphene nanoribbons embedded in boron nitride sheets. *Appl. Phys. Lett.* **95**(12), 123105 (2009).

[91] Pruneda, J. M. Origin of half-semimetallicity induced at interfaces of C-BN heterostructures. *Phys. Rev. B* **81**(16), 161409, February (2010).

[92] Xu, B., Lu, Y. H., Feng, Y. P., and Lin, J. Y. Density functional theory study of BN-doped graphene superlattice: Role of geometrical shape and size. *Journal of Applied Physics* **108**(7), 073711 (2010).

[93] Manna, A. K. and Pati, S. K. Tunable Electronic and Magnetic Properties in BxNyCz Nanohybrids: Effect of Domain Segregation. *The Journal of Physical Chemistry C* **115**(21), 10842 10850 (2011).

[94] Li, J. and Shenoy, V. B. Graphene quantum dots embedded in hexagonal boron nitride sheets. *Applied Physics Letters* **98**(1), (2011).

[95] Bernardi, M., Palummo, M., and Grossman, J. C. Optoelectronic Properties in Monolayers of Hybridized Graphene and Hexagonal Boron Nitride. *Phys. Rev. Lett.* **108**, 226805, Jun (2012).

[96] Azevedo, S. Energetic stability of B C N monolayer. *Physics Letters A* **351**(1 2), 109 112 (2006).

[97] Lam, K.-T., Lu, Y., Feng, Y. P., and Liang, G. Stability and electronic structure of two dimensional $C_x(BN)_y$ compound. *Applied Physics Letters* **98**(2), (2011).

[98] Ci, L., Song, L., Jin, C., Jariwala, D., Wu, D., Li, Y., Srivastava, A., Wang, Z. F., Storr, K., Balicas, L., Liu, F., and Ajayan, P. M. Atomic layers of hybridized boron nitride and graphene domains. *Nat. Mater.* **9**(5), 430 435, May (2010).

[99] Levendorf, M. P., Kim, C.-J., Brown, L., Huang, P. Y., Havener, R. W., Muller, D. A., and Park, J. Graphene and boron nitride lateral heterostructures for atomically thin circuitry. *Nature* **488**(7413), 627 632, August (2012).

[100] Sutter, P., Cortes, R., Lahiri, J., and Sutter, E. Interface Formation in Monolayer Graphene-Boron Nitride Heterostructures. *Nano Letters* **12**(9), 4869 4874 (2012).

[101] Kim, S. M., Hsu, A., Araujo, P. T., Lee, Y.-H., Palacios, T., Dresselhaus, M., Idrobo, J.-C., Kim, K. K., and Kong, J. Synthesis of Patched or Stacked Graphene and hBN Flakes: A Route to Hybrid Structure Discovery. *Nano Letters* **13**(3), 933 941 (2013).

[102] Liu, Z., Ma, L., Shi, G., Zhou, W., Gong, Y., Lei, S., Yang, X., Zhang, J., Yu, J., Hackenberg, K. P., Babakhani, A., Idrobo, J.-C., Vajtai, R., Lou, J., and Ajayan, P. M. In-plane heterostructures of graphene and hexagonal boron nitride with controlled domain sizes. *Nat. Nanotechnol.* **8**(2), 119 124, January (2013).

[103] Gao, Y., Zhang, Y., Chen, P., Li, Y., Liu, M., Gao, T., Ma, D., Chen, Y., Cheng, Z., Qiu, X., Duan, W., and Liu, Z. Toward Single-Layer Uniform Hexagonal Boron Nitride Graphene Patchworks with Zigzag Linking Edges. *Nano Letters* **13**(7), 3439 3443 (2013).

[104] Han, G. H., Rodríguez-Manzo, J. A., Lee, C.-W., Kybert, N. J., Lerner, M. B., Qi, Z. J., Dattoli, E. N., Rappe, A. M., Drndic, M., and Johnson, A. T. C. Continuous Growth of Hexagonal Graphene and Boron Nitride In-Plane Heterostructures by Atmospheric Pressure Chemical Vapor Deposition. *ACS Nano* **7**(11), 10129 10138 (2013).

[105] Liu, L., Park, J., Siegel, D. A., McCarty, K. F., Clark, K. W., Deng, W., Basile, L., Idrobo, J. C., Li, A.-P., and Gu, G. Heteroepitaxial Growth of Two-Dimensional Hexagonal Boron Nitride Templated by Graphene Edges. *Science* **343**(6167), 163 167 (2014).

[106] Lu, J., Zhang, K., Feng Liu, X., Zhang, H., Chien Sum, T., Castro Neto, A. H., and Loh, K. P. Order disorder transition in a two-dimensional boron carbon nitride alloy. *Nat Commun* **4**, 2681, October (2013).

[107] Ettenberg, M. and Olsen, G. H. The recombination properties of lattice-mismatched $In_xGa_{1-x}P$/GaAs heterojunctions. *Journal of Applied Physics* **48**(10), 4275 4280 (1977).

[108] Coon, D. D. and Liu, H. C. Lattice mismatch and band offsets in strained layers. *Journal of Applied Physics* **60**(8), 2893 2896 (1986).

[109] Anderson, R. Germanium-Gallium Arsenide Heterojunctions. *IBM J. Res. Dev.* **4**, 283 (1960).

[110] Franciosi, A. and de Walle, C. G. V. Heterojunction band offset engineering . *Surface Science Reports* **25**(1 4), 1 140 (1996).

[111] Peressi, M., Binggeli, N., and Baldereschi, A. Band engineering at interfaces: theory and numerical experiments. *Journal of Physics D: Applied Physics* **31**(11), 1273 (1998).

[112] Colombo, L., Resta, R., and Baroni, S. Valence-band offsets at strained Si/Ge interfaces. *Phys. Rev. B* **44**, 5572 5579, Sep (1991).

[113] Baldereschi, A., Baroni, S., and Resta, R. Band Offsets in Lattice-Matched Heterojunctions: A Model and First-Principles Calculations for GaAs/AlAs. *Phys. Rev. Lett.* **61**, 734 737, Aug (1988).

[114] Sze, S. M. and Ng, K. K. *Physics of Semiconductor Devices*. Wiley-Interscience, 3rd edition, , September (1981).

[115] Ohtomo, A., Muller, D. A., Grazul, J. L., and Hwang, H. Y. Artificial charge-modulationin atomic-scale perovskite titanate superlattices. *Nature* **419**(6905), 378 380, September (2002).

[116] Ohtomo, A. and Hwang, H. Y. A high-mobility electron gas at the LaAlO3/SrTiO3 heterointerface. *Nature* **427**(6973), 423 426, January (2004).

[117] Reyren, N., Thiel, S., Caviglia, A. D., Kourkoutis, L. F., Hammerl, G., Richter, C., Schneider, C. W., Kopp, T., Ruetschi, A.-S., Jaccard, D., Gabay, M., Muller, D. A., Triscone, J.-M., and Mannhart, J. Superconducting Interfaces between Insulating Oxides. *Science* **317**(5842), 1196 1199, August (2007).

[118] Brinkman, A., Huijben, M., van Zalk, M., Huijben, J., Zeitler, U., Maan, J. C., van der Wiel, W. G., Rijnders, G., Blank, D. H. A., and Hilgenkamp, H. Magnetic effects at the interface between non-magnetic oxides. *Nat. Mater.* **6**(7), 493 496, July (2007).

[119] Vanderbilt, D. and King-Smith, R. D. Electric polarization as a bulk quantity and its relation to surface charge. *Phys. Rev. B* **48**, 4442 4455, Aug (1993).

[120] Stengel, M. Electrostatic stability of insulating surfaces: Theory and applications. *Phys. Rev. B* **84**, 205432, Nov (2011).

[121] Born, M. and Oppenheimer, R. Zur Quantentheorie der Molekeln. *Annalen der Physik* **389**(20), 457 484 (1927).

[122] Soler, J. M., Artacho, E., Gale, J. D., García, A., Junquera, J., Ordejón, P., and Sánchez-Portal, D. The SIESTA method for ab initio order-N materials simulation. *J. Phys.: Condens. Matter* **14**(11), 2745 (2002).

[123] Junquera, J., Paz, O., Sánchez-Portal, D., and Artacho, E. Numerical atomic orbitals for linear-scaling calculations. *Phys. Rev. B* **64**, 235111, Nov (2001).

[124] Slater, J. C. and Koster, G. F. Simplified LCAO Method for the Periodic Potential Problem. *Phys. Rev.* **94**, 1498 1524, Jun (1954).

[125] Foa Torres, L. E. F., Roche, S., and Charlier, J. C. *Introduction to Graphene-Based Nanomaterials: From Electronic Structure to Quantum Transport.* Cambridge University Press, Cambridge, UK, (2014).

[126] Roche, S. and Mayou, D. Conductivity of Quasiperiodic Systems: A Numerical Study. *Phys. Rev. Lett.* **79**, 2518 2521, Sep (1997).

[127] Katsnelson, M. I., Novoselov, K. S., and Geim, A. K. Chiral tunnelling and the Klein paradox in graphene. *Nat. Phys.* **2**, 620 625 (2006).

[128] Katsnelson, M. I. Zitterbewegung, chirality, and minimal conductivity in graphene. *Eur. Phys. J. B* **51**, 157 160 (2006).

[129] Giovannetti, G., Khomyakov, P. A., Brocks, G., Kelly, P. J., and van den Brink, J. Substrate-induced band gap in graphene on hexagonal boron nitride: Ab initio density functional calculations. *Phys. Rev. B* **76**, 073103, Aug (2007).

[130] Slawińska, J., Zasada, I., and Klusek, Z. Energy gap tuning in graphene on hexagonal boron nitride bilayer system. *Phys. Rev. B* **81**, 155433, February (2010).

[131] Yan, H., Chu, Z.-D., Yan, W., Liu, M., Meng, L., Yang, M., Fan, Y., Wang, J., Dou, R.-F., Zhang, Y., Liu, Z., Nie, J.-C., and He, L. Superlattice Dirac points and space-dependent Fermi velocity in a corrugated graphene monolayer. *Phys. Rev. B* **87**, 075405, Feb (2013).

[132] Yu, G. L., Gorbachev, R. V., Tu, J. S., Kretinin, A. V., Cao, Y., Jalil, R., Withers, F., Ponomarenko, L. A., Piot, B. A., Potemski, M., Elias, D. C., Chen, X., Watanabe, K., Taniguchi, T., Grigorieva, I. V., Novoselov, K. S., Fal/ ko, V. I., Geim, A. K., Mishchenko, A., et al. Hierarchy of Hofstadter states and replica quantum Hall ferromagnetism in graphene superlattices. *Nat. Phys.* **10**, 525 (2014).

[133] Woods, C. R., Britnell, L., Eckmann, A., Yu, G. L., Gorbachev, R. V., Kretinin, A., Park, J., Ponomarenko, L. A., Katsnelson, M. I., Gornostyrev, Y. N., Watanabe, K., Taniguchi, T., Casiraghi, C., Geim, A. K., and Novoselov, K. S. Commensurate-incommensurate transition for graphene on hexagonal boron nitride. *Nat. Phys.* **10**, 451 (2014).

[134] San-Jose, P., Gutiérrez, A., Sturla, M., and Guinea, F. Spontaneous Strains and Gap in Graphene on Boron Nitride. arXiv:1404.7777v2 [cond-mat.mes-hall] (2014).

[135] Jung, J., DaSilva, A., MacDonald, A. H., and Adam, S. Origin of band gaps in graphene on hexagonal boron nitride. arXiv:1403.0496v2 [cond-mat.mes-hall] (2014).

[136] Bokdam, M., Amlaki, T., Brocks, G., and Kelly, P. J. Band gaps in incommensurable graphene on hexagonal boron nitride. *Phys. Rev. B* **89**, 201404, May (2014).

[137] Park, C.-H., Yang, L., Son, Y.-W., Cohen, M. L., and Louie, S. G. Anisotropic behaviours of massless Dirac fermions in graphene under periodic potentials. *Nat. Phys.* **4**, 213 217 (2008).

[138] Park, C.-H., Yang, L., Son, Y.-W., Cohen, M. L., and Louie, S. G. New Generation of Massless Dirac Fermions in Graphene under External Periodic Potentials. *Phys. Rev. Lett.* **101**, 126804, Sep (2008).

[139] Sachs, B., Wehling, T. O., Katsnelson, M. I., and Lichtenstein, A. I. Adhesion and electronic structure of graphene on hexagonal boron nitride substrates. *Phys. Rev. B* **84**, 195414 (2011).

[140] Jung, J., Raoux, A., Qiao, Z., and MacDonald, A. H. Ab initio theory of moiré superlattice bands in layered two-dimensional materials. *Phys. Rev. B* **89**, 205414, May (2014).

[141] Pletikosić, I., Kralj, M., Pervan, P., Brako, R., Coraux, J., N Diaye, A. T., Busse, C., and Michely, T. Dirac Cones and Minigaps for Graphene on Ir(111). *Phys. Rev. Lett.* **102**, 056808, Feb (2009).

[142] Tonnoir, C., Kimouche, A., Coraux, J., Magaud, L., Delsol, B., Gilles, B., and Chapelier, C. Induced Superconductivity in Graphene Grown on Rhenium. *Phys. Rev. Lett.* **111**, 246805, Dec (2013).

[143] Coy Diaz, H., Addou, R., and Batzill, M. Interface properties of CVD grown graphene transferred onto MoS2(0001). *Nanoscale* **6**, 1071 1078 (2014).

[144] Hermann, K. Periodic overlayers and moiré patterns: theoretical studies of geometric properties. *Journal of Physics: Condensed Matter* **24**(31), 314210 (2012).

[145] Mishima, O. and Era, K. *Electric Refractory Materials*, 495 556. Marcel Dekker, New York (2000).

[146] Bai, C. and Zhang, X. Klein paradox and resonant tunneling in a graphene superlattice. *Phys. Rev. B* **76**, 075430, Aug (2007).

[147] Barbier, M., Peeters, F. M., Vasilopoulos, P., and Pereira, J. M. Dirac and Klein-Gordon particles in one-dimensional periodic potentials. *Phys. Rev. B* **77**, 115446, Mar (2008).

[148] Ho, J. H., Chiu, Y. H., Tsai, S. J., and Lin, M. F. Semimetallic graphene in a modulated electric potential. *Phys. Rev. B* **79**, 115427, Mar (2009).

[149] Brey, L. and Fertig, H. A. Emerging Zero Modes for Graphene in a Periodic Potential. *Phys. Rev. Lett.* **103**, 046809, Jul (2009).

[150] Tiwari, R. P. and Stroud, D. Tunable band gap in graphene with a noncentrosymmetric superlattice potential. *Phys. Rev. B* **79**, 205435, May (2009).

[151] Barbier, M., Vasilopoulos, P., and Peeters, F. M. Extra Dirac points in the energy spectrum for superlattices on single-layer graphene. *Phys. Rev. B* **81**, 075438, Feb (2010).

[152] Guinea, F. and Low, T. Band structure and gaps of triangular graphene superlattices. *Philos. Trans. A: Math. Phys. Eng. Sci.* **368**(1932), 5391 5402 (2010).

[153] Park, C.-H., Tan, L. Z., and Louie, S. G. Theory of the electronic and transport properties of graphene under a periodic electric or magnetic field . *Physica E: Low-dimensional Systems and Nanostructures* **43**(3), 651 656 (2011). ce:title NanoPHYS 09 /ce:title xocs:full-name Proceedings of the International Symposium on Nanoscience and Quantum Physics /xocs:full-name .

[154] Dell Anna, L. and De Martino, A. Magnetic superlattice and finite-energy Dirac points in graphene. *Phys. Rev. B* **83**, 155449, Apr (2011).

[155] Kindermann, M., Uchoa, B., and Miller, D. L. Zero-energy modes and gate-tunable gap in graphene on hexagonal boron nitride. *Phys. Rev. B* **86**, 115415, Sep (2012).

[156] Ortix, C., Yang, L., and van den Brink, J. Graphene on incommensurate substrates: Trigonal warping and emerging Dirac cone replicas with halved group velocity. *Phys. Rev. B* **86**, 081405, Aug (2012).

[157] Wallbank, J. R., Patel, A. A., Mucha-Kruczyński, M., Geim, A. K., and Fal ko, V. I. Generic miniband structure of graphene on a hexagonal substrate. *Phys. Rev. B* **87**, 245408, Jun (2013).

[158] Hofstadter, D. Energy levels and wave functions of Bloch electrons in rational and irrational magnetic fields. *Phys. Rev. B* **14**, 2239 (1976).

[159] Troullier, N. and Martins, J. L. Efficient pseudopotentials for plane-wave calculations. *Phys. Rev. B* **43**(3), 1993 2006, January (1991).

[160] Román-Pérez, G. and Soler, J. M. Efficient implementation of a van der Waals density functional: application to double-wall carbon nanotubes. *Phys. Rev. Lett.* **103**(9), 096102, August (2009).

[161] Monkhorst, H. J. and Pack, J. D. Special points for Brillouin-zone integrations. *Phys. Rev. B* **13**, 5188 5192, Jun (1976).

[162] Elias, D. C., Gorbachev, R. V., Mayorov, A. S., Morozov, S. V., Zhukov, A. A., Blake, P., Ponomarenko, L. A., Grigorieva, I. V., Novoselov, K. S., Guinea, F., and Geim, A. K. Dirac cones reshaped by interaction effects in suspended graphene. *Nat. Phys.* **7**, 701 (2011).

[163] Deacon, R. S., Chuang, K.-C., Nicholas, R. J., Novoselov, K. S., and Geim, A. K. Cyclotron resonance study of the electron and hole velocity in graphene monolayers. *Phys. Rev. B* **76**, 081406, Aug (2007).

[164] de Juan, F., Cortijo, A., and Vozmediano, M. A. H. Charge inhomogeneities due to smooth ripples in graphene sheets. *Phys. Rev. B* **76**, 165409, Oct (2007).

[165] de Juan, F., Sturla, M., and Vozmediano, M. A. H. Space Dependent Fermi Velocity in Strained Graphene. *Phys. Rev. Lett.* **108**, 227205, May (2012).

[166] Zou, Q., Belle, B. D., Zhang, L. Z., Xiao, W. D., Yang, K., Liu, L. W., Wang, G. Q., Fei, X. M., Huang, Y., Ma, R. S., Lu, Y., Tan, P. H., Guo, H. M., Du, S. X., and Gao, H.-J. Modulation of Fermi velocities of Dirac electrons in single layer graphene by moiré superlattice. *Applied Physics Letters* **103**(11), (2013).

[167] Mulliken, R. S. Electronic Population Analysis on LCAO MO Molecular Wave Functions. I. *The Journal of Chemical Physics* **23**(10), 1833 1840 (1955).

[168] Pruneda, J., Sánchez-Portal, D., Arnau, A., Juaristi, J., and Artacho, E. Heating electrons with ion irradiation: A first-principles approach . *Nuclear Instruments and Methods in Physics Research Section B: Beam Interactions with Materials and Atoms* **267**(4), 590 593 (2009). Proceedings of the 17th International Workshop on Inelastic Ion-Surface Collisions.

[169] Lin, L., García, A., Huhs, G., and Yang, C. SIESTA-PEXSI: massively parallel method for efficient and accurate ab initio materials simulation without matrix diagonalization. *Journal of Physics: Condensed Matter* **26**(30), 305503 (2014).

[170] Evers, F. and Mirlin, A. D. Anderson transitions. *Rev. Mod. Phys.* **80**, 1355 1417, Oct (2008).

[171] Abrahams, E., Anderson, P. W., Licciardello, D. C., and Ramakrishnan, T. V. Scaling Theory of Localization: Absence of Quantum Diffusion in Two Dimensions. *Phys. Rev. Lett.* **42**, 673 676, Mar (1979).

[172] Yang, W., Chen, G., Shi, Z., Liu, C.-C., Zhang, L., Xie, G., Cheng, M., Wang, D., Yang, R., Shi, D., Watanabe, K., Taniguchi, T., Yao, Y., Zhang, Y., and Zhang, G. Epitaxial growth of single-domain graphene on hexagonal boron nitride. *Nat. Mater.* **12**, 792 (2013).

[173] Anderson, P. W. Absence of Diffusion in Certain Random Lattices. *Phys. Rev.* **109**, 1492 1505, Mar (1958).

[174] Lherbier, A., Biel, B., Niquet, Y.-M., and Roche, S. Transport Length Scales in Disordered Graphene-Based Materials: Strong Localization Regimes and Dimensionality Effects. *Phys. Rev. Lett.* **100**, 036803, Jan (2008).

[175] Roche, S., Leconte, N., Ortmann, F., Lherbier, A., Soriano, D., and Charlier, J.-C. Quantum transport in disordered graphene: A theoretical perspective . *Solid State Communications* **152**(15), 1404 1410 (2012). Exploring Graphene, Recent Research Advances.

[176] Radchenko, T. M., Shylau, A. A., and Zozoulenko, I. V. Influence of correlated impurities on conductivity of graphene sheets: Time-dependent real-space Kubo approach. *Phys. Rev. B* **86**, 035418, Jul (2012).

[177] Anderson, P. W. Localized Magnetic States in Metals. *Phys. Rev.* **124**, 41 (1961).

[178] Nomura, K. and MacDonald, A. H. Quantum Transport of Massless Dirac Fermions. *Phys. Rev. Lett.* **98**, 076602, Feb (2007).

[179] Rycerz, A., Tworzydlo, J., and Beenakker, C. W. J. Anomalously large conductance fluctuations in weakly disordered graphene. *EPL (Europhysics Letters)* **79**(5), 57003 (2007).

[180] Wakabayashi, K., Takane, Y., and Sigrist, M. Perfectly Conducting Channel and Universality Crossover in Disordered Graphene Nanoribbons. *Phys. Rev. Lett.* **99**, 036601, Jul (2007).

[181] Zhang, Y.-Y., Hu, J., Bernevig, B. A., Wang, X. R., Xie, X. C., and Liu, W. M. Localization and the Kosterlitz-Thouless Transition in Disordered Graphene. *Phys. Rev. Lett.* **102**, 106401, Mar (2009).

[182] Lee, P. A. and Ramakrishnan, T. V. Disordered electronic systems. *Rev. Mod. Phys.* **57**, 287 337, Apr (1985).

[183] Moser, J., Tao, H., Roche, S., Alzina, F., Sotomayor Torres, C. M., and Bachtold, A. Magnetotransport in disordered graphene exposed to ozone: From weak to strong localization. *Phys. Rev. B* **81**, 205445, May (2010).

[184] Ortmann, F., Cresti, A., Montambaux, G., and Roche, S. Magnetoresistance in disordered graphene: The role of pseudospin and dimensionality effects unraveled. *EPL (Europhysics Letters)* **94**(4), 47006 (2011).

[185] Geim, A. K. and Novoselov, K. S. The rise of graphene. *Nat Mater* **6**, 183 191 (2007).

[186] Hamada, N., Sawada, S.-i., and Oshiyama, A. New one-dimensional conductors: Graphitic microtubules. *Phys. Rev. Lett.* **68**, 1579 1581, Mar (1992).

[187] Son, Y.-W., Cohen, M. L., and Louie, S. G. Energy Gaps in Graphene Nanoribbons. *Phys. Rev. Lett.* **97**, 216803, Nov (2006).

[188] Han, M. Y., Ozyilmaz, B., Zhang, Y., and Kim, P. Energy Band-Gap Engineering of Graphene Nanoribbons. *Phys. Rev. Lett.* **98**, 206805, May (2007).

[189] Eroms, J. and Weiss, D. Weak localization and transport gap in graphene antidot lattices. *New Journal of Physics* **11**(9), 095021 (2009).

[190] Bai, J., Zhong, X., Jiang, S., Huang, Y., and Duan, X. Graphene nanomesh. *Nat. Nanotechnol.* **5**, 190 (2010).

[191] Kim, M., Safron, N. S., Han, E., Arnold, M. S., and Gopalan, P. Fabrication and Characterization of Large-Area, Semiconducting Nanoperforated Graphene Materials. *Nano Letters* **10**(4), 1125 1131 (2010). PMID: 20192229.

[192] Zhao, R., Wang, J., Yang, M., Liu, Z., and Liu, Z. BN-Embedded Graphene with a Ubiquitous Gap Opening. *The Journal of Physical Chemistry C* **116**(39), 21098 21103 (2012).

[193] Li, X., Wang, X., Zhang, L., Lee, S., and Dai, H. Chemically Derived, Ultrasmooth Graphene Nanoribbon Semiconductors. *Science* **319**(5867), 1229 1232 (2008).

[194] Jiao, L., Zhang, L., Wang, X., Diankov, G., and Dai, H. Narrow graphene nanoribbons from carbon nanotubes. *Nature* **458**, 877 880 (2009).

[195] Fujita, M., Wakabayashi, K., Nakada, K., and Kusakabe, K. Peculiar Localized State at Zigzag Graphite Edge. *Journal of the Physical Society of Japan* **65**(7), 1920 1923 (1996).

[196] Lee, H., Son, Y.-W., Park, N., Han, S., and Yu, J. Magnetic ordering at the edges of graphitic fragments: Magnetic tail interactions between the edge-localized states. *Phys. Rev. B* **72**, 174431, Nov (2005).

[197] Son, Y.-W., Cohen, M. L., and Louie, S. G. Half-metallic graphene nanoribbons. *Nature* **444**, 347 349 (2006).

[198] Wolf, S. A., Awschalom, D. D., Buhrman, R. A., Daughton, J. M., von Molnár, S., Roukes, M. L., Chtchelkanova, A. Y., and Treger, D. M. Spintronics: A Spin-Based Electronics Vision for the Future. *Science* **294**(5546), 1488 1495 (2001).

[199] Terrones, M., Charlier, J.-C., Gloter, A., Cruz-Silva, E., Terrés, E., Li, Y. B., Vinu, A., Zanolli, Z., Dominguez, J. M., Terrones, H., Bando, Y., and Golberg, D. Experimental and Theoretical Studies Suggesting the Possibility of Metallic Boron Nitride Edges in Porous Nanourchins. *Nano Letters* **8**(4), 1026 1032 (2008). PMID: 18333621.

[200] Barone, V. and Peralta, J. E. Magnetic Boron Nitride Nanoribbons with Tunable Electronic Properties. *Nano Letters* **8**(8), 2210 2214 (2008). PMID: 18624385.

[201] Topsakal, M., Akturk, E., and Ciraci, S. First-principles study of two- and one-dimensional honeycomb structures of boron nitride. *Phys. Rev. B* **79**, 115442, Mar (2009).

[202] Lai, L., Lu, J., Wang, L., Luo, G., Zhou, J., Qin, R., Gao, Z., and Mei, W. N. Magnetic Properties of Fully Bare and Half-Bare Boron Nitride Nanoribbons. *The Journal of Physical Chemistry C* **113**(6), 2273 2276 (2009).

[203] Park, C.-H. and Louie, S. G. Energy Gaps and Stark Effect in Boron Nitride Nanoribbons. *Nano Letters* **8**(8), 2200 2203 (2008). PMID: 18593205.

[204] Zhang, Z. and Guo, W. Energy-gap modulation of BN ribbons by transverse electric fields: First-principles calculations. *Phys. Rev. B* **77**, 075403, Feb (2008).

[205] Zheng, F., Sasaki, K.-i., Saito, R., Duan, W., and Gu, B.-L. Edge States of Zigzag Boron Nitride Nanoribbons. *Journal of the Physical Society of Japan* **78**(7), 074713 (2009).

[206] Miyamoto, Y., Louie, S. G., and Cohen, M. L. Chiral Conductivities of Nanotubes. *Phys. Rev. Lett.* **76**, 2121 2124, Mar (1996).

[207] Gal pern, E. G., Pinyaskin, V. V., Stankevich, I. V., and Chernozatonskii, L. A. Heteroatomic Nanotubes with Quasi-One-Dimensional Superlattice Structure. *The Journal of Physical Chemistry B* **101**(5), 705 709 (1997).

[208] Blase, X. Properties of composite $B_xC_yN_z$ nanotubes and related heterojunctions. *Computational Materials Science* **17**(2 4), 107 114 (2000).

[209] Yu, Z., Hu, M. L., Zhang, C. X., He, C. Y., Sun, L. Z., and Zhong, J. Transport Properties of Hybrid Zigzag Graphene and Boron Nitride Nanoribbons. *The Journal of Physical Chemistry C* **115**(21), 10836 10841 (2011).

[210] Seol, G. and Guo, J. Bandgap opening in boron nitride confined armchair graphene nanoribbon. *Applied Physics Letters* **98**(14), (2011).

[211] He, J., Chen, K.-Q., Fan, Z.-Q., Tang, L.-M., and Hu, W. P. Transition from insulator to metal induced by hybridized connection of graphene and boron nitride nanoribbons. *Applied Physics Letters* **97**(19), (2010).

[212] Xiao, H., He, C., Zhang, C., Sun, L., Peng, X., Zhang, K., and Zhong, J. Size effect of half-metallic properties of BN/C hybrid nanoribbons . *Physica B* **407**(24), 4770 4772 (2012).

[213] Stengel, M. and Vanderbilt, D. Berry-phase theory of polar discontinuities at oxide-oxide interfaces. *Phys. Rev. B* **80**, 241103, Dec (2009).

[214] Bristowe, N. C., Stengel, M., Littlewood, P. B., Artacho, E., and Pruneda, J. M. One-dimensional half-metallic interfaces of two-dimensional honeycomb insulators. *Phys. Rev. B* **88**, 161411, Oct (2013).

[215] Reich, S., Maultzsch, J., Thomsen, C., and Ordejón, P. Tight-binding description of graphene. *Phys. Rev. B* **66**, 035412, Jul (2002).

[216] Boykin, T. B., Luisier, M., Klimeck, G., Jiang, X., Kharche, N., Zhou, Y., and Nayak, S. K. Accurate six-band nearest-neighbor tight-binding model for the pi-bands of bulk graphene and graphene nanoribbons. *Journal of Applied Physics* **109**(10), 104304 (2011).

[217] Semenoff, G. W. Condensed-Matter Simulation of a Three-Dimensional Anomaly. *Phys. Rev. Lett.* **53**, 2449 2452, Dec (1984).

[218] Partoens, B. and Peeters, F. M. From graphene to graphite: Electronic structure around the K point. *Phys. Rev. B* **74**, 075404, Aug (2006).

[219] Nilsson, J., Castro Neto, A. H., Guinea, F., and Peres, N. M. R. Electronic properties of bilayer and multilayer graphene. *Phys. Rev. B* **78**, 045405, Jul (2008).

[220] Jung, J. and MacDonald, A. H. Accurate tight-binding models for the β bands of bilayer graphene. *Phys. Rev. B* **89**, 035405, Jan (2014).

[221] Ribeiro, R. M. and Peres, N. M. R. Stability of boron nitride bilayers: Ground-state energies, interlayer distances, and tight-binding description. *Phys. Rev. B* **83**, 235312, Jun (2011).

[222] Martinez-Gordillo, R., Roche, S., Ortmann, F., and Pruneda, M. Transport fingerprints at graphene superlattice Dirac points induced by a boron nitride substrate. *Phys. Rev. B* **89**, 161401, Apr (2014).

[223] Yamashiro, A., Shimoi, Y., Harigaya, K., and Wakabayashi, K. Spin- and charge-polarized states in nanographene ribbons with zigzag edges. *Phys. Rev. B* **68**, 193410, Nov (2003).

[224] Sasaki, K.-i. and Saito, R. Magnetism as a Mass Term of the Edge States in Graphene. *Journal of the Physical Society of Japan* **77**(5), 054703 (2008).

[225] Dutta, S., Lakshmi, S., and Pati, S. K. Electron-electron interactions on the edge states of graphene: A many-body configuration interaction study. *Phys. Rev. B* **77**, 073412, Feb (2008).

[226] Hubbard, J. Electron Correlations in Narrow Energy Bands. *Proc. R. Soc. Lond. A* **276**(1365), 238 257 (1963).

[227] Nakada, K., Fujita, M., Dresselhaus, G., and Dresselhaus, M. S. Edge state in graphene ribbons: Nanometer size effect and edge shape dependence. *Phys. Rev. B* **54**, 17954 17961, Dec (1996).

[228] Wakabayashi, K., Fujita, M., Ajiki, H., and Sigrist, M. Electronic and magnetic properties of nanographite ribbons. *Phys. Rev. B* **59**, 8271 8282, Mar (1999).

[229] Ezawa, M. Peculiar width dependence of the electronic properties of carbon nanoribbons. *Phys. Rev. B* **73**, 045432, Jan (2006).

[230] Gunlycke, D. and White, C. T. Tight-binding energy dispersions of armchair-edge graphene nanostrips. *Phys. Rev. B* **77**, 115116, Mar (2008).

[231] Graf, M. and Vogl, P. Electromagnetic fields and dielectric response in empirical tight-binding theory. *Phys. Rev. B* **51**, 4940 4949, Feb (1995).

[232] Perdew, J. P., Burke, K., and Ernzerhof, M. Generalized Gradient Approximation Made Simple. *Phys. Rev. Lett.* **77**(18), 3865 3868, October (1996).

[233] Korytár, R., Pruneda, M., Junquera, J., Ordejón, P., and Lorente, N. Band selection and disentanglement using maximally-localized Wannier functions: the cases of Co impurities in bulk copper and the Cu (111) surface. *J. Phys.: Condens. Matter* **22**(38), 385601, September (2010).

[234] Souza, I., Marzari, N., and Vanderbilt, D. Maximally-localized Wannier functions for entangled energy bands. *Phys. Rev. B* **65**, 035109, August (2001).

[235] Mostofi, A. A., Yates, J. R., Lee, Y.-S., Souza, I., Vanderbilt, D., and Marzari, N. Wannier90: A tool for obtaining maximally-localised Wannier functions. *Comp. Phys. Comm.* **178**(9), 685 699 (2008).

[236] Giannozzi, P., Baroni, S., Bonini, N., Calandra, M., Car, R., Cavazzoni, C., Ceresoli, D., Chiarotti, G. L., Cococcioni, M., Dabo, I., Corso, A. D., de Gironcoli, S., Fabris, S., Fratesi, G., Gebauer, R., Gerstmann, U., Gougoussis, C., Kokalj, A., Lazzeri, M., Martin-Samos, L., Marzari, N., Mauri, F., Mazzarello, R., Paolini, S., Pasquarello, A., Paulatto, L., Sbraccia, C., Scandolo, S., Sclauzero, G., Seitsonen, A. P., Smogunov, A., Umari, P., and Wentzcovitch, R. M. QUANTUM ESPRESSO: a modular and open-source software project for quantum simulations of materials. *J. Phys.: Cond. Matt.* **21**(39), 395502, September (2009).

[237] Fonseca Guerra, C., Handgraaf, J.-W., Baerends, E. J., and Bickelhaupt, F. M. Voronoi deformation density (VDD) charges: Assessment of the Mulliken, Bader, Hirshfeld, Weinhold, and VDD methods for charge analysis. *Journal of Computational Chemistry* **25**(2), 189 210 (2004).

[238] Wangsness, R. K. *Electromagnetic Fields*. John Wiley & Sons, Inc., (1979).

[239] Press, W. H., Flannery, B. P., Teukolsky, S. A., and Vetterling, W. T. *Numerical Recipes in Fortran: The Art of Scientific Computing*. Cambridge University Press, 2nd edition, (1992).

[240] Ivanovskaya, V. V., Zobelli, A., Stéphan, O., Briddon, P. R., and Colliex, C. BN Domains Included into Carbon Nanotubes: Role of Interface. *The Journal of Physical Chemistry C* **113**(38), 16603 16609 (2009).

[241] An, W. and Turner, C. H. Linking Carbon and Boron-Nitride Nanotubes: Heterojunction Energetics and Band Gap Tuning. *The Journal of Physical Chemistry Letters* **1**(15), 2269 2273 (2010).

[242] Pruneda, J. M. Native defects in hybrid C/BN nanostructures by density functional theory calculations. *Phys. Rev. B* **85**, 045422, Jan (2012).

[243] Tombros, N., Jozsa, C., Popinciuc, M., Jonkman, H. T., and van Wees, B. J. Electronic spin transport and spin precession in single graphene layers at room temperature. *Nature* **448**, 571 (2007).

[244] Hueso, L. E., Pruneda, J. M., Ferrari, V., Burnell, G., Valdes-Herrera, J. P., Simons, B. D., Littlewood, P. B., Artacho, E., Fert, A., and Mathur, N. D. Transformation of spin information into large electrical signals using carbon nanotubes. *Nature* **445**, 410 (2007).

[245] Kim, W. Y. and Kim, K. S. Prediction of very large values of magnetoresistance in a graphene nanoribbon device. *Nat. Nanotechnol.* **3**, 408 (2008).

[246] Bai, J., Cheng, R., Xiu, F., Liao, L., Wang, M., Shailos, A., Wang, K. L., Huang, Y., and Duan, X. Very large magnetoresistance in graphene nanoribbons. *Nat. Nanotechnol.* **5**, 655 (2010).

[247] Popinciuc, M., Józsa, C., Zomer, P. J., Tombros, N., Veligura, A., Jonkman, H. T., and van Wees, B. J. Electronic spin transport in graphene field-effect transistors. *Phys. Rev. B* **80**, 214427, Dec (2009).

[248] Zhang, Z., Chen, C., and Guo, W. Magnetoelectric Effect in Graphene Nanoribbons on Substrates via Electric Bias Control of Exchange Splitting. *Phys. Rev. Lett.* **103**, 187204, Oct (2009).

[249] Jung, J. and MacDonald, A. H. Magnetoelectric coupling in zigzag graphene nanoribbons. *Phys. Rev. B* **81**, 195408, May (2010).

[250] Qi, J., Qian, X., Qi, L., Feng, J., Shi, D., and Li, J. Strain-Engineering of Band Gaps in Piezoelectric Boron Nitride Nanoribbons. *Nano Letters* **12**(3), 1224 1228 (2012).

[251] Duerloo, K.-A. N., Ong, M. T., and Reed, E. J. Intrinsic Piezoelectricity in Two-Dimensional Materials. *The Journal of Physical Chemistry Letters* **3**(19), 2871 2876 (2012).

[252] King-Smith, R. D. and Vanderbilt, D. Theory of polarization of crystalline solids. *Phys. Rev. B* **47**, 1651 1654, Jan (1993).

[253] López-Suárez, M., Pruneda, M., Abadal, G., and Rurali, R. Piezoelectric monolayers as nonlinear energy harvesters. *Nanotechnology* **25**(17), 175401 (2014).

[254] Liu, A. Y., Wentzcovitch, R. M., and Cohen, M. L. Atomic arrangement and electronic structure of BC_2N. *Phys. Rev. B* **39**, 1760 1765, Jan (1989).

[255] Sai, N. and Mele, E. J. Microscopic theory for nanotube piezoelectricity. *Phys. Rev. B* **68**, 241405, Dec (2003).

[256] Nakhmanson, S. M., Calzolari, A., Meunier, V., Bernholc, J., and Buongiorno Nardelli, M. Spontaneous polarization and piezoelectricity in boron nitride nanotubes. *Phys. Rev. B* **67**, 235406, Jun (2003).

[257] Souza, I., Íniguez, J., and Vanderbilt, D. First-Principles Approach to Insulators in Finite Electric Fields. *Phys. Rev. Lett.* **89**, 117602, Aug (2002).

[258] Khoo, K. H., Mazzoni, M. S. C., and Louie, S. G. Tuning the electronic properties of boron nitride nanotubes with transverse electric fields: A giant dc Stark effect. *Phys. Rev. B* **69**, 201401, May (2004).

[259] Duan, C.-G., Nan, C.-W., Jaswal, S. S., and Tsymbal, E. Y. Universality of the surface magnetoelectric effect in half-metals. *Phys. Rev. B* **79**, 140403, Apr (2009).

[260] Martin, R. M. *Electronic Structure: Basic Theory and Practical Methods*. Cambridge Univ. Press, Cambridge, (2004).

[261] Marzari, N., Mostofi, A. A., Yates, J. R., Souza, I., and Vanderbilt, D. Maximally localized Wannier functions: Theory and applications. *Rev. Mod. Phys.* **84**, 1419 1475, Oct (2012).

[262] Marzari, N. and Vanderbilt, D. Maximally localized generalized Wannier functions for composite energy bands. *Phys. Rev. B* **56**, 12847 12865, Nov (1997).